Universidade de Brasília

Simulating a granular bed of repelling magnetic particles

Towards a granular damper

Caio Tomás de Paula

Advisor: Dr. Yuri Dumaresq Sobral

Department of Mathematics
Universidade de Brasília

Dissertation submitted in partial fulfilment of the requirements for the degree of
Master in Mathematics

Instituto de Ciências Exatas

Brasília, August 25, 2025

Simulating a granular bed of repelling magnetic particles: Towards a granular damper

by

Caio Tomás de Paula

Dissertation presented to the Department of Mathematics at the University of Brasília, as part of the requirements for obtaining the degree of

Master in Mathematics

Brasília, May 9, 2025

Examining Committee:

Yuri Dumaresq Sobral

Prof. Dr. Yuri Dumaresq Sobral – MAT/UnB
(Advisor)

Prof. Dr. Jérôme Depeyrot – IF/UnB
(Member)

Ascânio Dias Araújo

Prof. Dr. Ascânio Dias Araújo – UFC
(Member)

Prof. Dr. Felipe Pacheco Vázquez – IF/BUAP (México)
(Member)

Ficha catalográfica elaborada automaticamente,
com os dados fornecidos pelo(a) autor(a)

TD278s

Tomás de Paula, Caio
Simulating a granular bed of repelling magnetic particles: Towards a granular damper / Caio Tomás de Paula; orientador Yuri Dumaresq Sobral. Brasília, 2025.
134 p.

Dissertação(Mestrado em Matemática) Universidade de Brasília, 2025.

1. magnetic dipoles. 2. granular materials. 3. Verlet lists. 4. numerical simulations. I. Dumaresq Sobral, Yuri, orient. II. Título.

“É melhor ter companhia do que estar sozinho, porque maior é a recompensa do trabalho de duas pessoas.”

— Eclesiastes, 4:9 (NVI)

Agradecimentos

Naturalmente, alguns agradecimentos se fazem necessários. Afinal, este documento não é fruto apenas de um trabalho meu e do Yuri, mas de todos os amigos e familiares que deram seu suporte, carinho e tempo para que ele se concretizasse.

Em primeiro lugar agradeço a Deus por me permitir fazer este mestrado e me capacitar para tal antes e durante o próprio mestrado.

Agradeço também aos meus pais, Sérgio e Cláudia, que sempre me apoiaram em tudo; à Ana Luísa, hoje minha esposa, pela paciência em por muitas vezes abrir mão de tempo juntos para que eu pudesse escrever esta dissertação; ao meu orientador, Yuri, por ser um exemplo de profissional, de professor, de orientador e, acima de tudo, de ser humano; à professora Luciana, que me orientou em uma das iniciações científicas que fiz durante minha passagem pelo PET, por me ensinar como ser alguém que lidera pelo exemplo; aos professores Lucas Seco, Guy Grebot e Sheila Campos, pelos projetos em que trabalhamos juntos, que foram fundamentais para que eu entendesse realmente o quê é ser um pesquisador; aos meus amigos do PET, que foram companheiros em diversos momentos e por quem guardo um grande carinho: Matheus, João Vítor, Lívia, Pedro Cusinato, Davi, Anita, Isadora, Railandi, Thais, Riquelme, Henrique e Herbert; aos meus amigos do MAT e colegas de mestrado, que ajudaram a tornar as aulas e os exames mais leves: Valdemir, Josy, Pedro Luís, Iuri, Callebe, Ângelo, Heloísa, Fabiane, Francisco e Wanessa; aos meus irmãos e irmãs acadêmicas, que várias vezes me ajudaram a desopilar a cabeça com nossas discussões no WhatsApp: Jorge, Caio (o Xará), Marina, Luís, Camila, Alan, Daniel, Dhiego e Saulo; aos meus professores do Ensino Médio, Paulo Luiz, Luiz Antônio e Carlos Sérgio, que me incentivaram a cursar Matemática quando eu nem considerava isso uma possibilidade.

Por último, mas não menos importante, agradeço a você, leitor, que se dispôs a ler este trabalho. Espero que ele lhe seja útil!

Resumo

Título: Simulação de um leito granular de partículas magnéticas repelentes: rumo a um amortecedor granular

Neste trabalho analisamos aspectos numéricos e da dinâmica de um sistema físico composto de ímãs de dimensões milimétricas confinados a uma célula de Hele-Shaw — essencialmente um material granular magnético. Estudamos e caracterizamos o comportamento deste material sob compressão de acordo com os diferentes parâmetros físicos através de simulações computacionais. Generalizamos a simulação para estudar um sistema bi-disperso, onde o material granular é composto por duas espécies de ímãs com tamanhos distintos — e também detalhamos como generalizar o algoritmo computacional para lidar com sistemas poli-dispersos. Apresentamos também uma otimização computacional do algoritmo de simulação usando listas de Verlet para reduzir o tempo de simulação e estudamos o comportamento do sistema quando o leito granular é sujeito a uma compressão advinda de uma massa em queda livre, caracterizando o movimento oscilatório-amortecido resultante.

Palavras-chave: dipolos magnéticos, materiais granulares, listas de Verlet

Abstract

In this work, we analyze numerical aspects and the dynamics of a physical system composed of millimeter-sized magnets confined within a Hele-Shaw cell—essentially a magnetic granular material. We study and characterize the behavior of this material under compression based on different physical parameters through computational simulations. We generalize the simulation to study a bi-disperse system, where the granular material is composed of two species of magnets with distinct sizes—and we also detail how to generalize the computational algorithm to handle poly-disperse systems. Additionally, we present a computational optimization of the simulation algorithm using Verlet lists to reduce simulation time and study the system's behavior when the granular bed is subjected to compression from a freely falling mass, characterizing the resulting damped oscillatory motion.

Keywords: magnetic dipoles, granular materials, Verlet lists

Contents

List of Figures

List of Tables

List of Algorithms

List of Metrics and Symbols

Verlet list related symbols

r_v	Verlet list neighbour radius
r_c	Verlet list cutoff radius
r_s	Verlet list skin radius ($r_v - r_c$)
$\widehat{d_p}$	Average particle displacement per simulation step
s_r	Average amount of simulation steps between Verlet lists reconstructions

Bi-disperse metrics and symbols

$\mathcal{R}$	Hexagon regularity metric in the Voronoi diagram
R	Mixing ratio of big and small particles
a	Aspect ratio of the system (ratio between small and big particle diameters)
$n_{5,6,7}$	Proportion of pentagons, hexagons and heptagons in the Voronoi diagram
Ψ_6	Global orientational order parameter
$\binom{n}{r}$	Combination of r elements from array of n elements

Computational/numeric symbols

O	Big O notation
h	Simulation time step

General metrics and symbols

ϕ	Packing fraction of the system (proportion of area occupied by particles)
$\hat{D}$	Mean inter-particle distance
δ_a^t	Minimum particle distance to the piston at time t and aspect ratio a
D	Particle diameter
ε	Particle width

m	Particle mass
μ	Particle magnetic moment
ρ	Particle density
Br	Particle residual magnetization
E	Wall separation in the Hele-Shaw cell
W	Hele-Shaw cell width
H	Hele-Shaw cell height
μ_0	Vacuum magnetic permeability
N_i	Total normal force on particle i
F^i_{pp}	Total force on particle i due to other particles
F^i_{pw}	Total force on particle i due to the walls
τ_{ij}	Torque on particle i due to particle j
g	Gravity acceleration
v	Piston velocity
μ_e	Static friction coefficient
μ_d	Dynamic friction coefficient

Carta aberta ao MAT/PPGMAT: o futuro exige mudanças

Nem tudo foram flores na minha trajetória dentro do PPGMAT. Peço licença ao leitor para deixar um breve comentário/desabafo acerca de alguns aspectos do programa de mestrado do PPGMAT (creio que parte dos comentários também se aplicam ao programa de doutorado, mas não tenho propriedade para comentar sobre ele diretamente).

Antes de tudo, gostaria de começar do começo: quais são os objetivos de um mestrado acadêmico? Ao meu ver, os principais são dois:

- introduzir o aluno à pesquisa/à realidade acadêmica;
- preparar o aluno para desenvolver pesquisa independentemente.

E quais **não** são os objetivos de um mestrado acadêmico? Acho que podemos concordar que o principal não objetivo é ser uma graduação 2.0, fazendo uma tonelada de matérias apenas para acúmulo de conhecimento.

Na seção seguinte, observo o que considero ser os pontos negativos princpais do programa e listo algumas sugestões e ideias de melhorias. No restante desta seção, gostaria de deixar um desabafo pessoal.

Sim, é assustador mudar a maneira como as coisas estão sendo feitas, principalmente quando a maioria já está confortável e acostumada ao *status quo*. Mas as mudanças são necessárias, na pós e também na graduação (bacharelado): ambas estão **morrendo**. A cada dia que passa, mais alunos desistem de perseguir um grau de bacharel/mestre/doutor, não só por causa da baixa remuneração mas também por causa de programas jurássicos que exigem que o aluno entregue a alma em prol do grau.

Pelas minhas experiências no Departamento, eu vejo que boa parte da resistência à mudança venha do famigerado "conceito CAPES 7", que atualmente o PPGMAT possui. De fato, o formato atual de avaliação da CAPES foi criado em 1998 e, na primeira avaliação neste formato, o PPGMAT recebeu nota 6 (biênio 1996–1997), que se manteve até a avaliação trienal de 2013. A partir desta avalição, o programa passou a ter nota 7, a máxima possível. Em particular, o curso de mestrado, que existe desde a década de 1970, se manteve com nota máxima no formato antigo de avaliação da CAPES desde sua primeira avaliação até a mudança no formato [2, Cap.2]. Além disso, não vejo como razoável o argumento de que o PPGMAT tenha conceito CAPES 7 para justificar manutenção da estrutura do programa. De fato, as notas 6 e 7 nem se aplicam para o mestrado, apenas para o doutorado [3]!

Fica claro que o PPGMAT tem uma longa história de excelência. Diferentemente de vários outros programas de pós-graduação, já começamos com um nível alto de excelência. Entretanto, um fato deixa evidente que o custo deste nível de excelência foi a falta de mudanças: desde 1988 é exigido que os alunos de mestrado façam exames de qualificação em Álgebra, Análise, Geometria e Matemática Aplicada. 35 **anos** (em 2023). Há 35 anos o sistema de avaliação do mestrado não muda!

E para refutar a máxima do "em time que está ganhando não se mexe", eu cito a notícia sobre o IMPA Tech [4], que traz a iniciativa do Instituto de Matemática Pura e Aplicada — IMPA (criado em 1952) de criar um curso de graduação voltado para tecnologia. Eu acho que podemos definir o IMPA, *alma mater* do nosso único medalhista Fields (até a data de escrita desta carta), como "um time que está ganhando".

Pessoalmente, eu quase desisti de continuar no mestrado do MAT. Atualmente estou empregado, trabalhando na área de TI (coisa que, inclusive, o curso não me preparou nem um pouco e eu estudei totalmente por fora — outro ponto de melhoria e atualização que o curso precisa). A entrada no mercado de trabalho abriu os meus olhos para como existe não uma distância entre mercado e academia, mas uma verdadeira fossa das Marianas. A quantidade de liberdade, autonomia e incentivo à independência que existe no mercado é infinitamente superior à do MAT atual (e, creio, à da academia de maneira geral — claro, existem exceções) além, claro, da remuneração ser simplesmente incomparável, principalmente em áreas de tecnologia, como desenvolvimento de software, engenharia de dados, ciência de dados, análise de dados, etc: posições de entrada (júnior) pagam mais do que a bolsa de mestrado (mesmo após o reajuste recente!) e posições geralmente obtidas após 2 anos de carreira (pleno) pagam o mesmo ou mais que a bolsa de doutorado (mesmo após reajuste recente!). Trocando em miúdos: graduar-se no MAT e perseguir uma carreira em tecnologia traz uma remuneração, após 6 anos (que seria o tempo médio de um mestrado e doutorado), pelo menos duas vezes maior que a bolsa de doutorado reajustada, sem mencionar o fator bem mais valioso, que é tempo de mercado e experiência!

O MAT e o PPGMAT têm uma quantidade extraordinária de mentes afiadas e preparadas para resolver problemas. A formação em Matemática, quando bem realizada, capacita o egresso a analisar situações e pensar em alternativas e saídas criativas; sobretudo, capacita o egresso a ser autônomo na busca por tais alternativas e na busca por conhecimento. Com uma formação em Matemática (e uma pós-graduação), você aprende a aprender. Você aprende:

- como e onde procurar por referências;
- a como assimilar rapidamente as ideias centrais de um trabalho/texto/argumento;
- a ser conciso nas suas explicações, sem perder os detalhes de vista;
- a apresentar ideias claramente (ou deveria, se tivéssemos mais seminários e menos provas, em especial na pós-graduação);
- a gerenciar o seu tempo.

Ainda assim, o sentimento constante (principalmente na pós-graduação) é de que somos vistos como inferiores: simples "aluninhos" que não têm noção de nada e precisam ser moldados no formato que o programa exige. Somos adultos capazes de tomar decisões por conta própria (como a de se mudar para Brasília, no caso de alunos de outras instituições). Precisamos de **orientação**, e não de cabrestos. Precisamos de **oportunidades**, e não de obstáculos.

Beira à insanidade ouvir de professores que "o propósito do mestrado é que você começe a se especializar na sua área" (sim, já ouvi isso) quando fazemos de tudo, exceto nos especializar. Sua área é Geometria? Legal, toma aqui uma prova de Álgebra de 4h; se reprovar duas vezes você tá fora! Se a prova aborda conteúdos correlatos com geometria? Não, não, a gente quer ter certeza de que você sabe calcular a forma canônica de Jordan de uma transformação linear na mão, porque vai quê no seu doutorado você precisa disso. Se acontecer, você não vai precisar gastar 10 minutos para achar um programa que calcule essa forma, basta gastar 10 minutos para calcular na mão e mais 10 minutos para conferir se sua conta tá certa! Ah, toma aqui também uma prova de Análise. De fato, Análise e Geometria têm várias conexões, mas a gente quer saber mesmo é se você decorou tim-tim por tim-tim do Teorema de Arzelà-Ascoli. Desta forma, caso você precise dele, basta recorrer à memória ao invés dos livros escritos por especialistas!

Tem algo muito errado com qualquer departamento que não reconheça isso. Tem algo muito errado com qualquer departamento cujos professores agem como se fossem superiores, diminuindo as lutas e sofrimentos de alunos enquanto estão lá no topo da sua torre de marfim chamada concurso público. E sim, é uma torre de marfim. Estando nela, é possível não dar aulas para os alunos matriculados em suas disciplinas e, no lugar, participar de eventos/premiações ou mesmo realizar inúmeras visitas a colaboradores. Estando nela, é possível entrar em sala de aula de camiseta, bermuda e chinelo, com as mãos sujas de graxa, e assistir os alunos darem a aula que você deveria dar, enquanto você faz comentários rudes, grosseiros e sem empatia. Estando nela, é extremamente fácil dizer que para obter uma posição em uma universidade é preciso estar disposto a abrir mão e se mudar (por alguns anos, talvez permanentemente) para o outro lado do país ou mesmo do oceano, mesmo sem nunca ter feito isso.

Eu estou exausto do mundo acadêmico. Exausto dessa briga de galo de egos entre professores e áreas. Exausto do status quo de publicação acadêmica, onde o que vale é quantidade e não qualidade. Exausto de ser olhado de cima para baixo. Exausto da preguiça e do medo em fazer mudanças estruturais no departamento.

Para os meus colegas — e aqui me refiro a alunos e não a professores, porque apesar de achar que os professores deveriam ser nossos colegas profissionais, não me referirei desta forma a quem não se refere a mim desta forma —, eu deixo uma provocação: parem de achar que vocês dependem de professor (a) e se valorizem. Os trabalhos que vocês desenvolvem, tanto no mestrado quanto no doutorado, são de vocês. Tomem consciência disso e se apropriem do que vocês desenvolvem e criam. Pouco é falado sobre, mas a grande verdade é que nessa relação "simbiótica" orientador (a)-orientado (a), os docentes dependem de nós tanto quanto nós dependemos deles, senão mais!

Gostaria de deixar claro que os comentários aqui escritos não se estendem a todo o corpo docente do MAT. Existem professores e professoras do mais alto profissionalismo no departamento. De forma a ser um exemplo de profissional para aqueles que não o são, irei me abster de citar nomes.

Na minha formatura de graduação, eu recebi o prêmio de aluno destaque. Hoje eu me pergunto, destaque em quê? Em ter um IRA alto? Em ter SS nas matérias "temidas" do bacharelado? Muito provavelmente. Afinal de contas, é assim que se avalia um aluno, não é mesmo? Pelo desempenho em provas. E adivinha? O mesmo se mantém na pós-graduação. E aí o interessante é que como futuros pesquisadores somos incentivados a colaborar e construir nosso *network* e todas essas coisas legais. E em nenhum momento sequer da nossa formação isso é incentivado.

Eu espero que esta carta provoque uma reflexão séria. Também tenho certeza de que muitos colegas alunos vão se identificar com vários trechos. Aos colegas que se identificarem: enquanto vocês tiverem força para lutar por mudanças, façam-no! A vontade de lutar por mudanças é sinal de que ainda existe amor e preocupação. A partir do momento em que essa vontade sumir, não tenha vergonha em desistir. O mundo acadêmico é por vezes muito orgulhoso e permeado de egos inflados para te dizer isto, mas eu digo: às vezes, a melhor decisão é abrir mão e ir embora.

Neste outro artigo [5], entitulado "How gradschool turned me into Darth Vader" — em tradução livre, "Como a pós-graduação me transformou no Darth Vader", a autora traça um paralelo muito divertido e, ao mesmo tempo, trágico, entre a forma atual como a academia ser organiza e a Ordem Jedi do universo de Star Wars. Um trecho particularmente interessante:

"Meanwhile I, and many students like me, entered graduate school hoping to join a community dedicated to the pursuit of knowledge, only to find that academia's primary function is simply the reproduction of itself. As institutions, the goal of the Jedi Order and the academy at their most base level is to survive. As padawans and students alike have found, this institutional purpose is often fundamentally at odds with the health and safety of its members. It also renders them inflexible when faced with the changes necessary for them to continue on. We are more than all the things academia tries to turn us into."

Se me permitem a tradução livre com grifo próprio,

"Enquanto isso eu e muitos alunos como eu entramos na pós-graduação esperando nos juntar a uma comunidade dedicada à busca de conhecimento, apenas para descobrirmos que a função primária da academia é simplesmente reproduzir a si mesma. Como instituições, o objetivo da Ordem Jedi e da academia, em seu nível mais básico, é sobreviver. Da mesma forma que padawans e estudantes descobriram, esse propósito institucional frequentemente se contrapõe à saúde e segurança de seus membros. Ele também os deixa inflexíveis quando se deparam com as mudanças necessárias para que sigam em frente. ***Nós somos mais do que todas as coisas nas quais a academia tenta nos transformar****."*

No fim das contas, a moeda de troca no mundo acadêmico é prestígio e influência. E essa moeda é uma mão de ferro invisível: se pronunciar contra o *status quo* muitas vezes é se tornar um pária. Para amarrar esta discussão geral sobre o mundo acadêmico e partir para uma discussão mais específica ao PPGMAT, deixo aqui um tweet [6], que contém um trecho de um livro de Max Perutz — biólogo molecular austríaco ganhador do prêmio Nobel de Química em 1962 — que discorre sobre a liberdade para criar e pensar nas universidade e institutos.

Hoje, no nosso programa de pós-graduação, as disciplinas preparatórias para os exames qualificatórios não isentam os alunos de fazer as provas, independente da menção obtida. Basicamente, os alunos pagam o preço do corpo docente do departamento ter profissionais preguiçosos, que dão aulas medíocres. O **próprio departamento não confia na qualidade das aulas que os seus integrantes ministram, e julgam necessário, depois de um semestre inteiro de aulas e avaliações, realizar uma bateria de provas para "qualificar o aluno"**. E mais: todos os exames que fiz eram extremamente parecidos com as provas das disciplinas. Qual a lógica? Melhor fazer disciplinas com uma prova final de toda a matéria, não?

A grande verdade é que é inútil tentar convencer diretamente apenas os professores e coordenadores de que a realidade da pós no MAT hoje é insustentável a longo prazo. Precisamos convencer os **alunos** de que:

1. não é normal passar o estresse que eles passam ganhando o que ganham de bolsa (quando ganham);
2. antes de sair da graduação e emendar um mestrado direto, é preciso ponderar:
    - você tem um projeto de vida? (se não tiver, vai procurar e volte quando tiver)
    - você tem noção de onde você tá entrando?
    - você tem noção do tipo de mentalidade que a academia tem?
    - o seu projeto de vida passa diretamente por isso?
    - você está entrando no mestrado por quê? Pelo status? Por que você gosta de estudar? Para ser um(a) pesquisador(a)? Não existe uma resposta certa para esta pergunta, mas existem respostas erradas.

E para os alunos de mestrado atuais, alguns lembretes/conselhos:

- o seu mestrado não é mais importante do que a sua saúde (mental/emocional/física);
- o seu mestrado não é mais importante do que a sua família;
- o seu mestrado não é mais importante do que os seus relacionamentos;
- o mestrado **é seu** e não do seu orientador;
- ninguém (absolutamente **ninguém**) vai saber ou ligar para quantos exames você reprovou ou quanto você estudou (para o bem e para o mal);
- você provavelmente tem na faixa de 22 a 25 anos; esquece esse mestrado por uma semana e vai viver!
- na mesma linha: sim, você precisa de férias; não, o recesso da pós que você fica estudando para exame não conta!
- tente se enxergar como funcionário, e não como aluno. Você pode não ter um vínculo empregatício firmado em contrato, mas o nível do que você estuda e a quantidade de trabalho que você tem são os mesmos ou maiores.
- na mesma linha: parem de aceitar tudo e questionem! Interrompam as aulas! Por que é assim e não assado? Vocês são a próxima leva de pesquisadores/professores! Incomodem o conformismo alheio!

Para os professores e pesquisadores do Departamento: tenham coragem! Coragem de olhar para o estado atual dos nossos programas de pós-graduação para além do "Capes nota 7". Coragem de levantar o que está bom e poderia ser melhorado; o que está ruim e deve ser corrigido; e o que está péssimo e deve ser repensado. Coragem de mudar!

O MAT foi responsável pela criação do primeiro curso de mestrado da UnB, pela formação do primeiro aluno de graduação da UnB e pela formação do primeiro doutor da UnB [2]. Este Departamento tem em sua origem a veia do pioneirismo. Mas nos acostumamos. Ficamos acostumados a fazer as coisas de uma certa forma. "É assim, sempre foi assim".

> "A vida é assim: esquenta e esfria, aperta e daí afrouxa, sossega e depois desinquieta. O que ela quer da gente é coragem."
>
> — Guimarães Rosa

Saber o que é correto e não o fazer é falta de coragem. E todos nós já sabemos, há algum tempo, que o correto é realizar mudanças nos nossos programas de pós-graduação.

Ao corpo docente do Departamento: vocês são pesquisadores e pesquisadoras do mais alto escalão. Pessoas que não apenas trabalham com Ciência mas que **são** cientistas. Pessoas que, por natureza, questionam as coisas à sua volta buscando entendê-las nas suas origens, nas suas causas, nos seus princípios fundamentais. Pessoas que não se dão por satisfeitas até que a explicação esteja completa. Pessoas que não aceitam qualquer resposta. Pessoas que não aceitam qualquer coisa. Pessoas que não deveriam aceitar a permanência de uma estrutura de programas de pós-graduação inalterada há decadas, principalmente quando esta permanência se baseia em argumentos frágeis.

Propostas de melhoria

O modelo de avaliação vigente no PPGMAT se baseia nos famigerados "exames": quatro provas de 4h de duração cada, uma para cada grande área do departamento (Álgebra, Ánalise, Geometria, Matemática Aplicada — esta última abrangendo uma escolha dentre as áreas de Probabilidade, Sistemas Dinâmicos, Computação e Mecânica). Este modelo tem sido aplicado há décadas, praticamente desde a criação do programa em meados de 1960. Embora a história e a tradição possam conferir um certo valor à metodologia, vários questionamentos já foram levantados com relação à adequação desta abordagem atualmente. Os motivos e razões que fundamentam tais críticas são inúmeros; alguns são pontuados abaixo. Não obstante, meu foco nesta seção não é discutir apenas os pontos negativos: gostaria de discutir ideias concretas de melhorias, que possam ser discutidas de forma séria tendo o melhor interesse do PPGMAT em mente.

Pontos negativos do método atual

- Excesso de estresse e pressão psicológica: o modelo de provas longas e isoladas coloca uma pressão psicológica excessiva sobre os alunos, o que pode prejudicar seu desempenho e seu bem-estar. Esse estresse crônico é contraproducente, causando ansiedades que afetam negativamente a aprendizagem.

- Foco restrito em habilidades testáveis e memorização: o formato de provas de 4h acaba privilegiando uma forma de avaliação extremamente restritiva, que testa principalmente habilidades de memorização e resolução de problemas sob pressão. Isso não reflete adequadamente a capacidade dos alunos de realizar pesquisas independentes, trabalhar em equipe ou comunicar suas ideias de forma clara, habilidades fundamentais para a dissertação e a vida acadêmica em geral. Na configuração atual, os nossos exames são mais uma perda de tempo e motivo de estresse para os alunos do que uma forma legítima e razoável de aferir a proficiência do mestrando nas 4 grandes áreas da Matemática. Considerando que boa parte dos alunos que realizam os exames cursam as disciplinas preparatórias antes, por que não utilizar a disciplina como instrumento de aferição de proficiência? Por que fazemos uma disciplina por um semestre inteiro, sendo avaliados, e ao final ainda é preciso prestar uma prova de 4h que, a depender da área, pode pedir coisas do tipo "enuncie o Teorema XYZ" ou "defina ABC" que, ao meu ver, não medem maturidade matemática mas apenas a capacidade de armazenamento de informação? Somos matemáticos ou bibliotecas ambulantes, que precisam cuspir enunciados de teoremas e definições sempre que requisitado? Sim, devemos ter pelo menos uma noção básica dos teoremas e definições principais da área, mas imagino que o fato de todo(a) docente ter sua bilioteca particular é prova suficiente de que este questionamento é puramente retórico.

- Desestímulo à reflexão crítica e criatividade: a metodologia de avaliação não incentiva a reflexão profunda e criativa. Em vez disso, ela promove uma abordagem reativa e técnica, onde os alunos se preparam apenas para reproduzir soluções predefinidas, em vez de explorar novas ideias ou questionar os paradigmas existentes.

- Falta de diversificação na avaliação: o modelo atual não contempla formas alternativas de avaliação, como projetos, apresentações, artigos ou mesmo avaliações contínuas, que poderiam ser mais eficazes em medir o desenvolvimento acadêmico de forma mais holística e flexível.

- Impacto negativo no tempo de formação: as provas de qualificação exigem uma preparação intensa e muitas vezes prolongada, o que retarda ou atropela o avanço dos alunos nas etapas seguintes do programa, como a elaboração da dissertação. Esse tempo poderia ser melhor investido no aprofundamento do conhecimento específico da área de pesquisa do aluno.

- Bolsas defasadas: a realidade hoje é que a bolsa de mestrado (mesmo com o reajuste feito em 2023) não é suficiente para o(a) aluno(a) sobreviver, que dirá viver. Portanto, não vejo como é coerente/razoável exigir tantas horas do aluno considerando que boa parte ainda precisa trabalhar por fora para fazer face às despesas.

Falhas no argumento de manutenção da nota 7 da CAPES

- Inadequação ao novo contexto acadêmico: o fato de o programa manter uma nota 7 na avaliação da CAPES não é um argumento suficiente para justificar a perpetuação de práticas que não atendem às necessidades e expectativas dos alunos e do cenário acadêmico atual, nacional e internacional. A nota alta é fruto de uma análise que pode estar desatualizada, especialmente se os critérios de avaliação da CAPES não consideram as metodologias de ensino e avaliação mais inovadoras. Uma evidência que apoia esta última sugestão é o fato de que esta a nota 7 se manteve durante pelo menos as duas últimas décadas mesmo sem alterações na estrutura do programa.

- Estabilidade à custa da inovação: a alegação de que mudanças no formato de avaliação possam comprometer a qualidade do programa carece de uma análise mais profunda. Na verdade, a resistência a mudanças pode resultar na estagnação do programa, impedindo a adaptação às novas exigências da pesquisa científica e do mercado de trabalho. A evolução do ensino superior exige flexibilidade e a capacidade de implementar metodologias mais eficazes.

- Capacidade de adaptação do programa: o argumento de que a nota CAPES deve ser preservada sem mudanças substanciais ignora a capacidade do programa de se adaptar sem comprometer a qualidade. A inovação nas metodologias de ensino e avaliação não implica em uma diminuição da qualidade acadêmica, mas sim em um aprimoramento do processo formativo dos alunos.

Plano de ação para melhorar o processo de avaliação

- Diversificação das formas de avaliação: introduzir avaliações alternativas, como projetos de pesquisa, seminários, artigos acadêmicos e apresentações. Estas formas podem ser mais representativas do progresso acadêmico dos alunos e menos estressantes do que as provas de 4h. Além disso, elas promovem habilidades importantes como a comunicação científica e o trabalho em equipe. Outras ideias: separar as áreas em pura e aplicada (os professores de cada área decidiriam a classificação das mesmas) e o aluno teria de fazer pelo menos um exame de uma área pura e um exame de uma área aplicada, à sua escolha; extinguir os exames e passar a ter matérias obrigatórias; permitir que as matérias preparatórias para os exames isentem os alunos que obtiveram menção a partir de MS de prestar os exames; permitir que alunos do bacharelado que cursaram as Análises e as Álgebras com bom aproveitamento — SS em Álgebra 3 e Análise 3, por exemplo — sejam isentos dos respectivos exames.

- Mudança na quantidade de créditos exigidos: hoje, além de prestar os exames e defender a dissertação, precisamos cursar 32 créditos de disciplinas. Este número é muito alto. Algo como 18 ou 24 seria bem mais razoável, permitindo uma maior dedicação do aluno a cada disciplina realizada.

- Avaliação contínua: implementar uma avaliação contínua, em que os alunos sejam acompanhados ao longo do tempo em suas atividades acadêmicas. Isso incluiria avaliações periódicas de seu progresso na pesquisa, em conjunto com o orientador, permitindo ajustes no plano de estudos e intervenções mais eficazes caso necessário. Isto também permitiria uma verificação mais eficaz de possíveis “abandonos”, tanto por parte do aluno quanto por parte do orientador.

- Reformulação da qualificação: reconsiderar o formato da prova de qualificação, transformando-a em um processo mais interativo e construtivo. Isso poderia envolver a apresentação de um projeto de pesquisa para uma banca composta por professores e alunos, onde o foco fosse a discussão da viabilidade da pesquisa e a qualidade do planejamento do aluno, em vez de simplesmente um exame técnico. Uma etapa intermediária que poderia ser adotada antes do fim dos exames seria adotar, no edital de seleção, uma menção de corte a disciplinas específicas consideradas "equivalentes" aos exames: e.g., alunos com menção MS ou superior em Variável Complexa ficariam isentos de prestar o exame de Análise.

- Consulta e participação ativa dos alunos: organizar consultas periódicas com os alunos sobre o modelo de avaliação e coletar feedback sobre a eficácia e o impacto das mudanças implementadas. Isso garantiria que a reforma se alinhasse às necessidades dos alunos e aos objetivos do programa. Tais consultas poderiam ser feitas de forma semestral ou anual, com seus resultados sendo discutidos e divulgados abertamente. Isto não significa que a CPG irá se comprometer a realizar mudanças a cada semestre/ano, mas que sempre estará aberta a sugestões de mudanças.

- Maior rotatividade nos professores representantes de área na CPG: cada uma das grandes áreas possui um representante na CPG. Hoje, não é claro se existe um tempo limite de permanência de um representante de área na CPG. Seria interessante considerar a possibilidade de estabelecer um tempo limite para a representação, de forma a promover uma maior rotatividade dos representantes e, com isso, fomentar uma maior oxigenação de ideias no âmbito da CPG. A princípio, penso que um tempo limite de 1 ou 2 anos seria interessante. A mesma ideia se aplica para o chefe da pós-graduação, possivelmente com um tempo limite maior (2 ou 3 anos, a princípio).

- Capacitação de docentes e alunos: oferecer treinamentos regulares para docentes sobre novas abordagens pedagógicas e metodologias de avaliação. Para os alunos, a criação de workshops sobre gerenciamento de estresse e técnicas de estudo também poderia ser benéfica.

Eu espero, de coração, que nossos programas evoluam e melhorem cada vez mais com o passar dos anos. O MAT é e sempre será a minha casa, e todas as minhas opiniões e posicionamentos partem de um lugar de preocupação e carinho. Desejo longa vida ao MAT e que esse futuro possa ser construído de forma colaborativa e conjunta, aberta a mudanças e correções de rota!

Chapter 1

Introduction

> "Does real mathematics consist of algorithms or abstractions, and, when they are both present, which is more important? The answer is that every mathematician must be both an effective calculator and an abstract thinker."
>
> — Paul Halmos

Magnetic materials have fascinated scholars since antiquity due to their unique properties of attraction and repulsion. However, the scientific understanding of these phenomena began to develop significantly only in the 19th century, with the formulation of the fundamental laws of electromagnetism [7]. The study of magnetic materials progressed with the discovery of magnetic hysteresis and the establishment of Maxwell's equations, which provided the theoretical foundation for understanding magnetic fields in different media. In the 20th century, the investigation of magnetic structures at the atomic level led to the understanding of magnetic domains [8] and the development of materials with tunable magnetic properties, driving advancements in industry and modern technology [9, 10, 11].

Among the major technological applications of magnetic materials are data storage devices, including magnetic tapes, hard drives, and, more recently, magnetoresistive memory (MRAM) [12, 13]. Additionally, these materials play a crucial role in electric motors, transformers, and various biomedical applications, such as magnetic resonance imaging and magnetic hyperthermia for cancer treatment. Current research on magnetic materials focuses on the development of novel compounds, such as molecular magnets and magnetocaloric materials, which exhibit adjustable properties depending on temperature and applied magnetic fields [14].

1.1 Motivation for the project

This dissertation investigates a magnetic granular system composed of cylindrical magnets with diameters on the order of millimeters. These magnets form a granular bed that is compressed under the influence of a magnetic piston. The motivation for this study originates from the broader interest in simulating particle-based systems and the need to understand the compression behavior of fragile materials, particularly their stick-slip behavior associated with fracture processes. In our previous work [15], we started to investigate this system looking at numerical simulations and experiments (see experimental schematic in Fig. 1.1). We validated the proposed modelling by comparing the resulting dynamics with the observed dynamics in the experiments, and analysed properties of the system that are difficult to assess in experiments, such as the mean inter-particle distance, $\hat{D}$, which consists of the average of all pairwise inter-particle distances; and the effects of different types of friction on the dynamics of the compression.

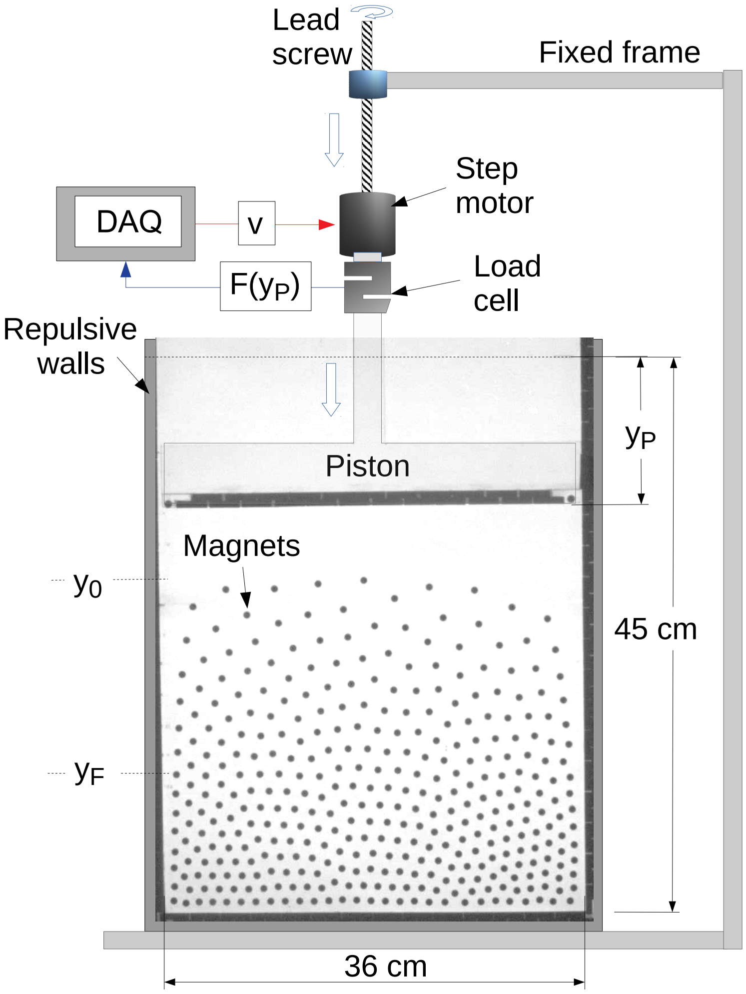

Figure 1.1 Experimental setup of the mono-disperse systems. Figure extracted from [16].

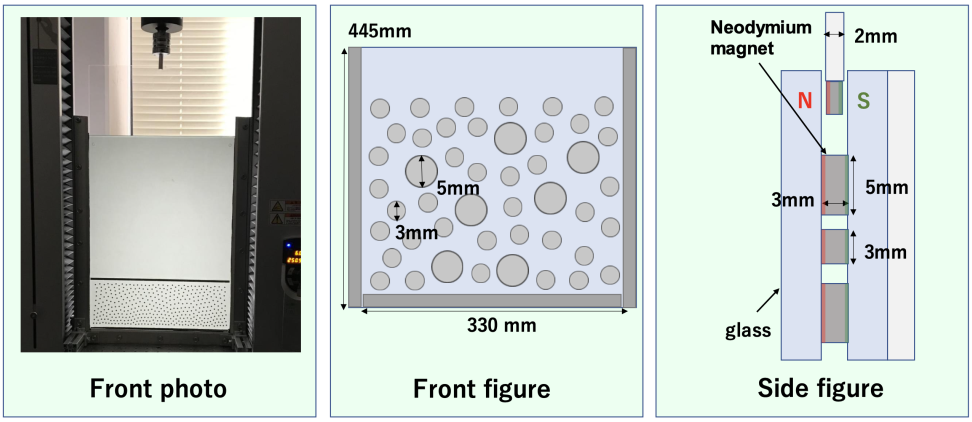

Front photo

Front figure

Side figure

Figure 1.2 Experimental setup of the bi-disperse systems, showing the two types of particles. Figure extracted from [16].

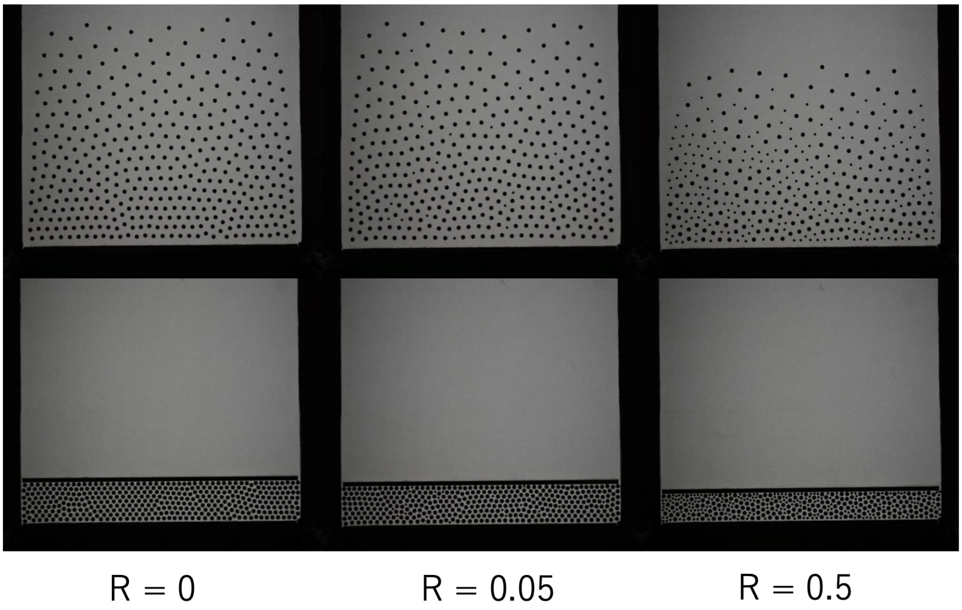

$R = 0$ $R = 0.05$ $R = 0.5$

Figure 1.3 Some experiments of the the bi-disperse systems with different values of mixing ratio (R). Figure extracted from [16].

We also looked at systems with more than one kind of particle [16], exploring the resulting dynamics as the proportion of each kind of particle varies in the system. Figs. 1.2 and 1.3 show schematics of the setup and a snapshot of some experiments conducted in this system.

Historically, the study of granular materials has been of significant interest in physics and engineering due to their complex mechanical properties, especially when external forces such as compression are applied. In particular, the interplay between magnetic interactions and granular mechanics introduces additional challenges and opportunities for modeling and simulation. Similar studies have explored the behavior of interacting particles, both magnetic and non-magnetic, under various conditions [15, 17]. These works establish the context for the present research, which seeks to consolidate previous findings by:

- performing systematic investigations on the effects of different parameters on the system dynamics;
- establishing a mathematical model that can be extended to poly-disperse systems;
- developing an optimized computational framework capable of simulating large-scale systems efficiently.

This dissertation is structured as follows: Part I presents the theoretical background and mathematical modeling of the system, followed by a detailed analysis of how simulation parameters, such as friction coefficients, piston velocity, and initial conditions, influence the system's behavior. Part II extends the study by introducing bi-dispersity, i.e., particles of two different sizes, and examining the effects of size ratio and composition on the overall system properties. The motivation for this extension arises from experimental investigations into bi-disperse granular systems [16], which revealed intriguing patterns of force distribution and particle arrangement under compression.

1.2 Magnetic granular systems

Magnetic granular systems have attracted increasing attention due to their rich and complex behavior. These systems exhibit a variety of phenomena, including self-assembly, magnetoresistance, magnetic hysteresis, and field-dependent phase transitions [18, 19]. Such properties enable applications in areas ranging from data storage to medical treatments, including magnetic hyperthermia [14, 20, 21].

Previous studies have investigated different configurations of magnetic particle interactions, highlighting the challenges associated with simulating large ensembles of such particles [22, 23]. One major issue in simulating many-body systems is the computational cost of calculating long-range interactions, which scales poorly with the number of particles. This work addresses this issue by optimizing simulation algorithms and implementing efficient numerical techniques to calculate particle-particle interactions.

In the specific system analyzed in this dissertation, cylindrical magnetic particles are compressed by a magnetic piston (see Fig. 1.1). Unlike typical granular materials, where contact forces dominate, our system relies solely on long-range magnetic interactions, as there is no direct contact between the magnets. This feature introduces a fundamental difference in force transmission and ordering mechanisms compared to conventional granular matter.

1.3 The richness of the setup

The confinement of the system within a Hele-Shaw cell introduces additional complexity and opportunities for exploration. The flexibility of the numerical model allows for the simulation of various physical conditions simply by adjusting key parameters, such as the strength of magnetic interactions and particle sizes. This adaptability makes the model highly versatile for exploring different scenarios.

Beyond the direct simulation of the experimental setup, the computational framework developed in this work has broader applicability. For example, by modifying boundary conditions, the same simulation can be adapted to study a magnetic damper, in which a piston moves under force excitations rather than being driven at a constant velocity. Such extensions highlight the potential of the model to explore related systems with minimal modifications.

Another intriguing aspect of the system is its evolving configuration, which shares similarities with phase transitions observed in melting processes [24, 25, 26, 27]. Motivated by this observation, we employ structural metrics commonly used in condensed matter physics to characterize the order and dynamics of the system.

1.4 Our approach

To simulate the physical system, we employ the Störmer-Verlet integration algorithm, which is well-suited for the study of conservative dynamical systems. The simulation code is implemented in Fortran for efficiency, while data analysis and visualization are conducted using Python.

Throughout the project, we have incorporated good software development practices, such as version control, to ensure reproducibility and facilitate further investigations. This approach not only enhances the reliability of the current study but also provides a robust foundation for future research on similar systems.

The combination of a well-defined numerical model, systematic parameter studies, and algorithmic optimizations ensures that this dissertation contributes to the broader understanding of magnetic granular systems while providing valuable tools for future investigations in the field.

More specifically, our objectives can be categorized into two main groups, as follows.

1.4.1 General objectives

Our primary goal is to simulate and mathematically characterize a granular system composed of repelling magnetic particles subjected to compression by a magnetic piston. The system may consist of either a single particle type (mono-disperse) or a mixture of two distinct particle types (bi-disperse). Additionally, we seek to optimize the numerical algorithm to enhance computational efficiency, facilitating faster and more scalable simulations. Finally, we take initial steps toward modeling a magnetic granular damper.

1.4.2 Specific objectives

More concretely, our aims include:

1. conducting a systematic investigation of the effects of various parameters on the dynamics and behavior of the mono-disperse system;

2. analyzing the force exerted on the piston and examining the evolution of particle arrangements during compression in the bi-disperse system;

3. studying the evolution of the Voronoi tessellation of particle configurations in the bi-disperse system, with a focus on the distribution of pentagons, hexagons, and heptagons;

4. implementing the Verlet lists algorithm within the simulation code to reduce computational cost, improving the time complexity from $O(n^2)$ to close to $O(n)$;

5. adapting the simulation framework to allow for the free fall of the piston and, based on its resulting motion, apply symbolic regression to derive the governing equation, thereby enabling a comprehensive characterization of the magnetic granular damper.

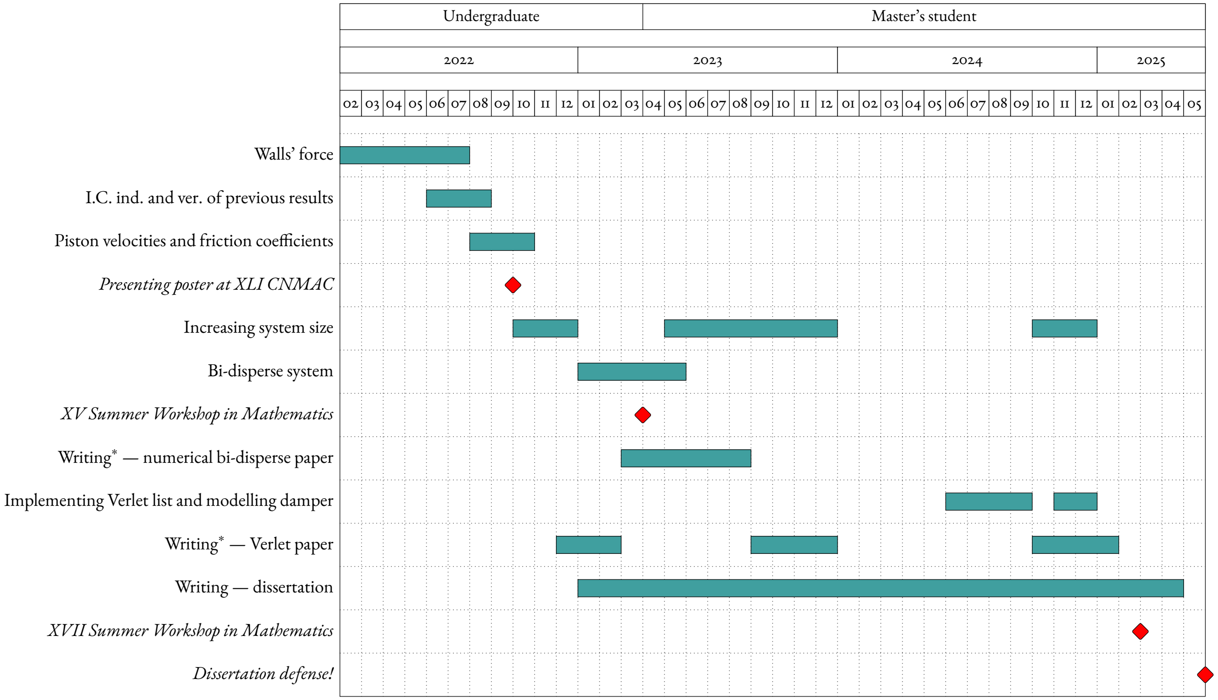

Figure 1.4 Gantt chart of the development and progress of the project. *The entries of the writing of the numerical bi-disperse and the Verlet papers correspond to my contributions to the work. Both are not published yet due to some pending work/review from coauthors.

Part I

Modelling a system of interacting magnets

CHAPTER 2

THEORETICAL BACKGROUND

> "What makes a house: ten-penny nails or blueprints? Is an opera the libretto or the music? Is an essay an exercise in syntax or an exposition of a subject? Is real physics done in a laboratory or on paper? The answer is the same in every case (namely both) and even to try to decide which component is more important is not much more meaningful than to debate whether for walking you need your right foot more or your left."
>
> — John Hammersley

2.1 What has already been done?

Figure 2.1 illustrates the standard system studied in this work: a layer of repelling magnetic particles confined in a Hele-Shaw cell and subject to compression by a piston. The indicated values of height, H, (45cm), width, W (36cm) and depth, E, (3.1mm) are the defaults ones used for our simulations, as shown in Table 2.1. Despite being shown as circles, the particles have cylindrical shape, as the cross-section in Figure 2.5 shows.

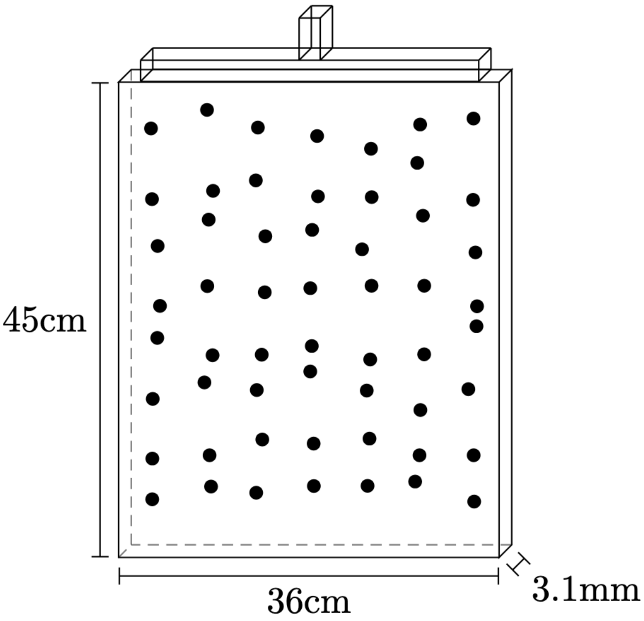

Figure 2.1 Illustration of the standard system studied in this work: a layer of repelling magnetic particles confined in a Hele-Shaw cell and compressed by a piston.

In our previous work [15], we investigated the dynamics of this system when subject to a compression-expansion cycle: the piston descends with a prescribed constant velocity up until a height of maximum compression (determined by the packing fraction of the system, that is, the proportion of area occupied by the particles) and then goes up with the same prescribed constant velocity until reaching the initial height, as shown in Fig. 2.2.

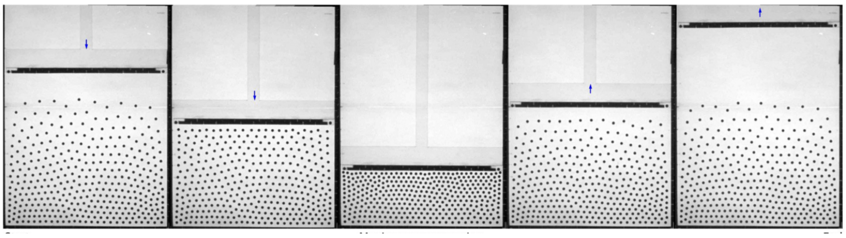

Figure 2.2 Snapshots of the compression for the experimental work. Figure extracted from [15].

On this system, we investigated how the force that the piston experiences during the compression-expansion cycle behaves, as well as how the instantaneous mean inter-particle changes throughout the cycle, which is defined as

$$\hat{D}(t) = \frac{1}{N(N-1)} \sum_i \sum_j \left| r_i(t) - r_j(t) \right|, \tag{2.1}$$

where $r_i(t)$ and $r_i(t)$ are the position vectors of particles i and j, respectively, and N is the total number of particles on the system. In Figs. 2.3 and [fig:snapshot_force_experiments] we show the behaviour of the normalized force (that is, the force on the piston at a given time divided by the maximum force on the piston during the cycle) on the piston during the cycle and the instantaneous mean inter-particle distance, respectively. Both figures exhibit two curves, one regarding a "standard" packed bed and another regarding a "loose" packed bed. These are two different configurations that were studied in the experimental section of [15]. The standard configuration refers to experiments where the magnets are initially positioned (manually) and the compression is carried out right after, while in the loose configuration there is a perturbation on this initial configuration that spaces the particles out on the cell before the compression starts. Lastly, we would like to make and observation about the x-axis in both figures. In Fig. 2.3, the x-axis indicates the displacement of the piston from the initial height, as in the bottom x-axis of Fig. 2.4. In this last figure, the top x-axis shows the packing fraction of the system, ϕ, during the compression. This number is defined as

$$\phi = \frac{\text{Total area occupied by the particles}}{\text{Area of the rectangle defined by the walls of the cell and the piston}}. \tag{2.2}$$

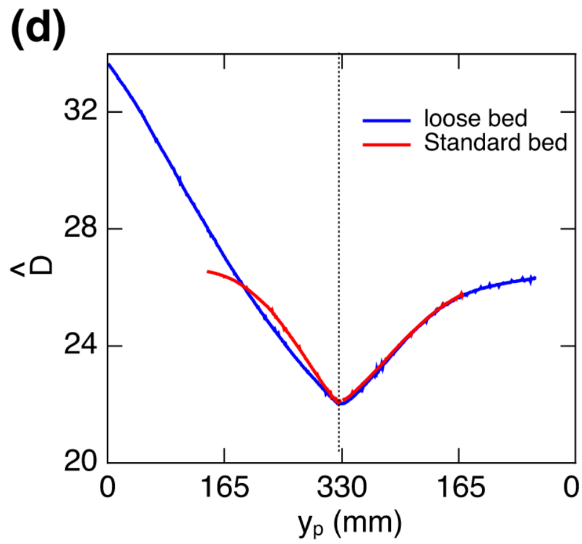

Figure 2.3 Mean distance between particles ($\hat{D}$) normalized by the particle diameter (D) during compression and expansion for the experiments. The x-axis represents the displacement of the piston, in millimeters, from the starting position from where the compression begins. Figure extracted from [15].

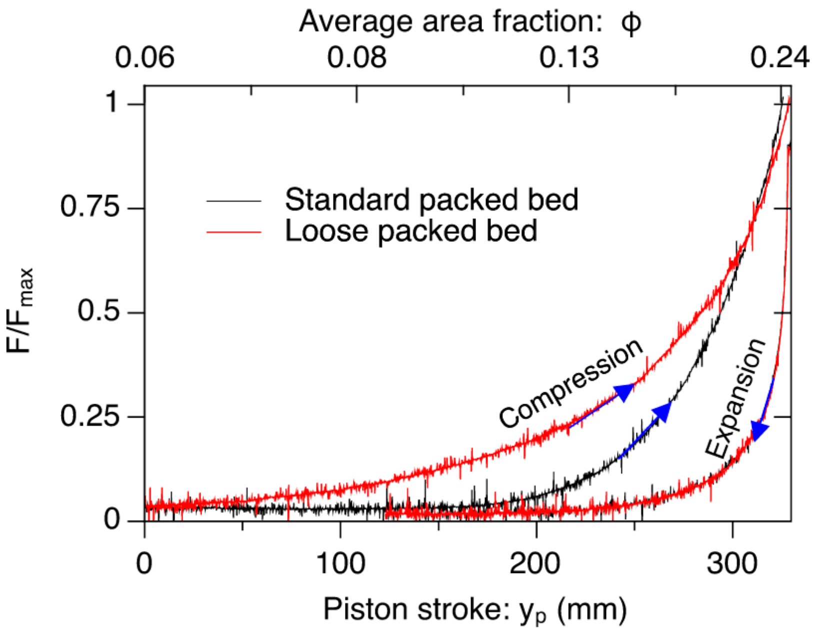

Figure 2.4 Normalized force on the piston ($F/F_{\max}$) versus piston stroke during the compression-expanstion cycle for the experiments. The x-axis represents the displacement of the piston, in millimeters, from the starting position from where the compression begins. Figure extracted from [15].

In the next sections, we shall discuss the details of the mathematical modelling of this system and the numerical method used in our simulations, together with a validation of such method. This will lay the foundation for the results that will be discussed from Chapter 3 onwards.

2.2 Governing equations and non-dimensionalization

As discussed in [15], the governing equations of our system are Newton's second law of motion applied to each particle:

$$m_i \frac{d^2 r_i}{dt^2} = F_M^i + F_F^i + F_g^i, \tag{2.3}$$

with m_i being the mass of the i-th particle,

$$r_i(t) = (x_i(t), y_i(t)) \tag{2.4}$$

their position at an instant t. Furthermore, F_F^i represents the friction force that opposes the movement of the i-th particle. In this work, as in [15], we work with two different models of friction: a dry friction model, in which the opposing force is constant up to a threshold and from that threshold onwards it becomes proportional to the contact force; and a viscous friction model, in which the opposing force is always proportional to the particle velocity. In this part of the work, we shall only use the dry friction model, since the viscous friction model was analysed, for the mono-disperse system, in our previous work [15]. The viscous model will be explored in the next part, when we explore the bi-disperse system. We also take F_g^i to represent the weight of particle i,

$$F_g^i = mg, \tag{2.5}$$

where m is the mass of a particle and g is the acceleration of gravity; and F_M^i represents the magnetic forces acting on the i-th particle, which are of two types: particle-particle interaction, F_{pp}^i, and particle-wall interaction, F_{pw}^i.

2.2.1 Particle-particle interaction

We consider that the particle-particle interaction is governed by the law [28]

$$F_{pp}^i = \frac{3\mu_0\mu_i\mu_j}{4\pi r_{ij}} \sum_{j\neq i} \left[(\hat{r}_{ij}\cdot\hat{\mu}_i)\hat{\mu}_j + (\hat{r}_{ij}\cdot\hat{\mu}_j)\hat{\mu}_i + (\hat{\mu}_i\cdot\hat{\mu}_j)\hat{r}_{ij} - 5(\hat{r}_{ij}\cdot\hat{\mu}_i)(\hat{r}_{ij}\cdot\hat{\mu}_j)\hat{r}_{ij}, \right] \tag{2.6}$$

where $\hat{r}_{ij}$ is the unitary vector pointing from the center of particle i to the center of particle j. Since we are considering a 2D configuration in which the particles' magnetic moments are perpendicular to the plane of motion, the dot product involving $\hat{r}_{ij}$ and any of the magnetic moments is 0. Also, since the particles are identical, $\mu_i = \mu_j$, which simplifies the expression down to

$$F_{pp}^i = \frac{3\mu_0\mu^2}{4\pi} \sum_{j\neq i} \frac{\hat{r}_{ij}}{r_{ij}^4}. \tag{2.7}$$

2.2.2 Particle-wall interaction

We also consider that the particle-wall magnetic interaction is given by

$$F^i_{pw} = \frac{\mu_0 \mu M}{2\pi} \sum_j \frac{\hat{w}_{ij}}{w_{ij}^{3.5}}, \tag{2.8}$$

where $\mu_0 = 4\pi \cdot 10^{-7}$ H/m is the magnetic permeability of free space, μ is the magnetic moment of the particles and $\hat{w}_{ij}$ is the unitary vector pointing from wall i to particle j. This law was numerically obtained in our previous work [15] from experimental data: it consists of the best fit to the data obtained from experiments. We will discuss this law further in Section 3.6.

2.2.3 Friction forces

Furthermore, we consider that the friction force between the grains and the glass walls of the cell obeys the dry model given in [15, 29]. The model assumes that particles tilt under the influence of misaligned dipoles, such as shown in Fig. 2.5. The torque generated on particle i by a particle j is given by [30, 31]

$$\tau_{ij} = \frac{\mu_0 \mu^2}{4\pi r_{ij}^3} \left[3(\hat{\mu}_j \cdot \hat{r})(\hat{\mu}_i \times \hat{r}) + (\hat{\mu}_i \times \hat{\mu}_j) \right]. \tag{2.9}$$

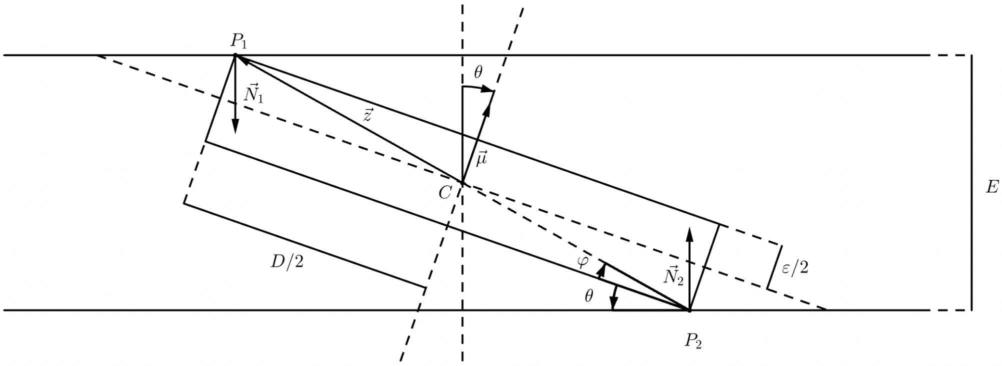

Figure 2.5 Geometry of the contact between a particle and the glass walls of the Hele-Shaw cell. View of one particle from the top of the Hele-Shaw cell.

We define

$$\theta = \arcsin\left(\frac{E}{\sqrt{\varepsilon^2 + D^2}}\right) - \varphi, \qquad \varphi = \arctan\left(\frac{\varepsilon}{D}\right). \tag{2.10}$$

In this setup, the rotation of particle i about its center is a consequence of the sum of magnetic torques τ_{ij} exerted upon it by another particle j in the system. This torque seeks to align particle dipoles μ_i and μ_j, so one of our assumptions for this derivation is that all particle dipoles in the system are parallel to one another. The reaction forces N_1 and N_2 are related to the magnetic torque by the following balance equation:

$$z \times N_1 + (-z) \times N_2 + \tau_{ij} = 0 \tag{2.11}$$

Now, using the geometry presented in Fig. 2.5, we see that

$$\hat{\mu}_i = \hat{\mu}_j, \quad \|\hat{\mu}_j \cdot \hat{r}\| = \cos(\pi/2 - \theta) = \sin(\theta), \quad \|\hat{\mu}_i \times \hat{r}\| = \sin(\pi/2 - \theta) = \cos(\theta), \quad \|\hat{\mu}_i \times \hat{\mu}_j\| = 0. \tag{2.12}$$

Therefore, Eq. (2.9) simplifies to

$$\tau_{ij} = \frac{3\mu_0\mu^2}{8\pi r_{ij}^3} \sin(2\theta). \tag{2.13}$$

Now, by noting that $N_2 = -N_1$, we get

$$-\tau_{ij} = 2z \times N_1 \implies 2zN\sin(\alpha) = \frac{3\mu_0\mu^2}{8\pi r_{ij}^3} \sin(2\theta), \tag{2.14}$$

where $\alpha = \pi/2 - \varphi - \theta$ and N is the normal force reacting to particle's i contact on the walls due to the torque of particle j. Isolating N, substituting $z = \sqrt{D^2 + \varepsilon^2}/2$ and summing over all particles j of the system, we have that the total normal force on particle i is given by

$$N_i = \frac{3\mu_0\mu^2}{8\pi} \cdot \frac{\sin(2\theta)}{\cos(\varphi + \theta)\sqrt{D^2 + \varepsilon^2}} \sum_{j \neq i} \frac{1}{r_{ij}^3}. \tag{2.15}$$

Table 2.1 Default values (in SI units) for the parameters of the simulation.

Particle properties						Cell dimensions		
m	ρ	D	μ	ε	Br	H	W	E
0.000625	7368.0	0.006	0.08775	0.003	1.3	0.45	0.36	0.0031

2.3 Numerical methodology

2.3.1 Integration of the equations of motions

In this work, we used the Verlet integration method, also known as Störmer-Verlet integration method [32]. This method is of order two and consists of approximating the solution to second-order differential equation

$$\begin{cases} x''(t) = A(x(t)), \\ x(t_0) = x_0, \\ x'(t_0) = v_0 \end{cases} \tag{2.16}$$

by the numerical solution $x_n \approx x(t_n)$ at the instants $t_n = t_0 + nh$, with a step $h > 0$, given by

1. $x_1 = x_0 + v_0 h + A(x_0)h^2/2$;
2. $x_{n+1} = 2x_n - x_{n-1} + A(x_n)h^2$, for $n \geqslant 1$.

The velocity at the n-th step is then approximated by

$$v_n = \frac{x_{n+1} - x_{n-1}}{2h}, \tag{2.17}$$

which is simply the well-known central finite-difference of order 2.

2.3.2 Generation of the initial condition

We start the simulation by positioning the particles in a grid and assingning initial velocities with random orientation and magnitude of 10^{-2}, as shown in the leftmost plot of the first row in Fig. 2.6. Then, during a relaxation time T_r, we allow the particles to fall and accomodate themselves (hence the name relaxation), as shown in the remaining snapshots of Fig. 2.6. During this relaxation, that takes 5 million steps, the piston starts to descend following an exponential law: very slowly at first and more rapidly as the relaxation ends. This is represented by the updating of the variable H, that represents the height of the piston.

When the relaxation ends, the height of the piston is set to H_0, the initial height at which the compression starts. After that, the compression starts and the height of the piston is updated at each step considering a constant velocity of descent. Furthermore, at each step of the simulation we compute the forces acting on the system (particle-particle, wall-particle, gravitational, friction), save the data and call the integration method.

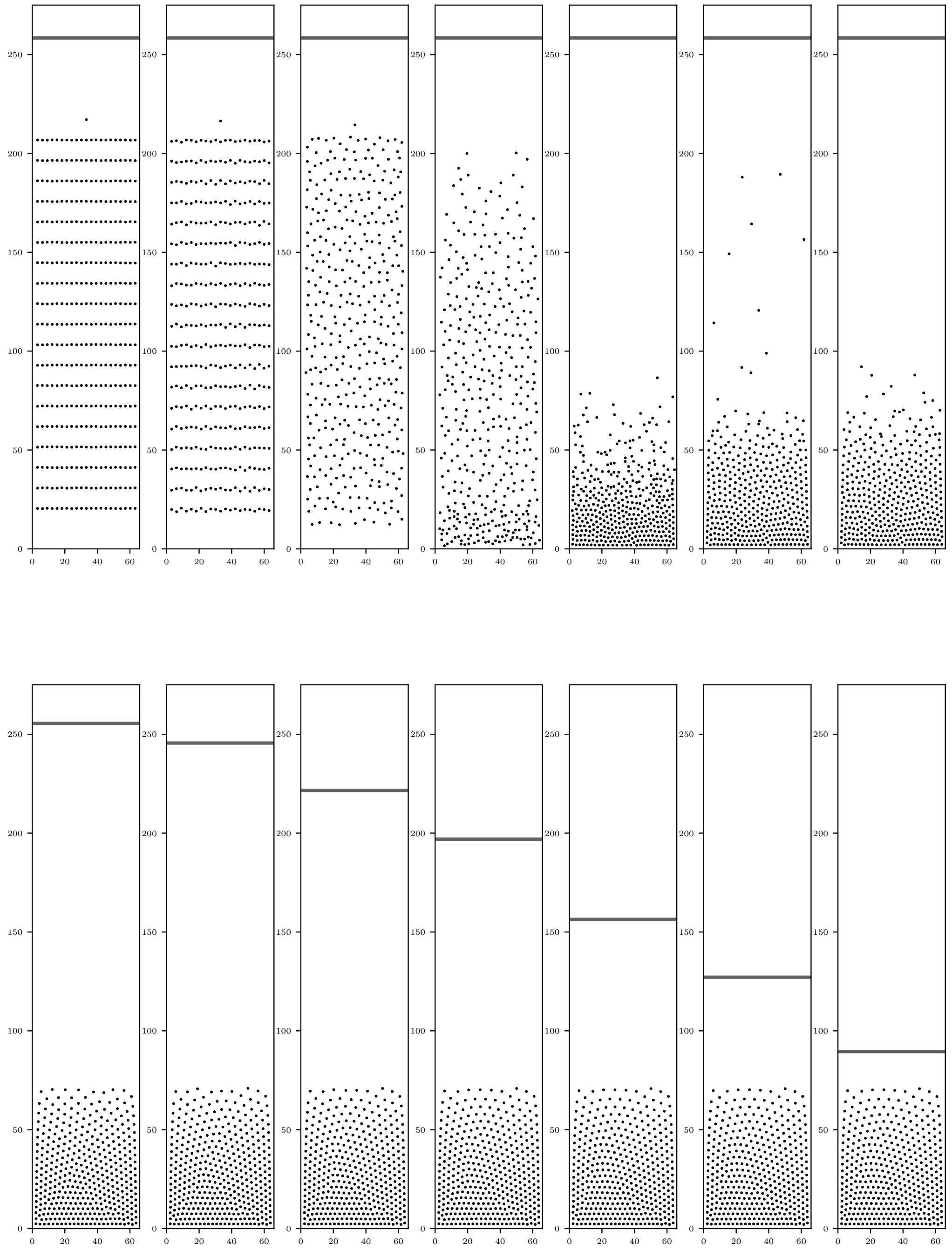

Figure 2.6 Snapshots of the first few moments of the simulation (first row, iterations 0, 80, 160, 640, 1500, 3000 and 3500 from left to right) and the remaining of the relaxation (second row, iterations 1.25M, 2.5M, 3.5M, 4M, 4.5M, 4.75M and 5M).

2.3.3 General algorithm

Algorithm 2.1 details the logic of our simulation code and where exactly the integration method is used.

Algorithm 2.1 MD algorithm for the (mono-disperse) granular system.

```
initialize variables
open output files
position particles in a perturbed ordered grid with random initial velocities of the order of $10^{-2}$ ▷ this is done before the compression starts!
for $t \leqslant T_{\max}$ do
    if $k < T_r$ then
        descend the piston with an exponential law $\exp(t-5)$ ▷ that is, the piston lowers smoothly during relaxation
    end if
    if $k = T_r$ then
        $H = H_0$ ▷ that is, when the relaxation ends the piston is positioned at the initial compression height
    end if
    if $T_r \leqslant k \leqslant T_b$ then
        $H = H - \Delta t \cdot V_c T/L$ ▷ that is, during the compression time we lower the piston by a constant factor related to the constant velocity
    end if
    for each particle $p$ do
        compute the magnetic force of the walls on $p$
        compute the gravitational force on $p$
        for every particle $q$ with index grater than $p$ do
            compute the magnetic force between $q$ and $p$
        end for
        compute the friction force on $p$
    end for
    save computed interactions on output files
    call the Verlet integration subroutine ▷ effectively updating the position of the particles
    advance the time step
    update $k = k + 1$
end for
save last iteration computed interactions on output files
close output files
```

2.3.4 Validation of the numerical method

As detailed in Part I, our simulations use the Störmer-Verlet method to integrate the movement and velocity of the particles in the system. In this section, we aim to validate the numerical method, showing its convergence and order. Furthermore, since this method is symplectic [32], we present a phase diagram that exhibits the energy-conserving property inherent to this class of methods. The simulations used for the following validations considered a single particle, starting from rest at a given height and in the horizontal middle of the Hele-Shaw cell, subject only to the action of gravity and the magnetic force of the bottom wall, that is, no friction forces and no piston acting on the particle. The simulations were conducted for a total time of $T = 2$ and for seven different time steps: 10^{-6}, $5 \cdot 10^{-7}$, $2 \cdot 10^{-7}$, 10^{-7}, $5 \cdot 10^{-8}$, $2 \cdot 10^{-8}$ and 10^{-8}, from coarser to finer.

2.3.4.1 Convergence and order validation

Our first object of validation was to check if the fall of the particle obeyed the law of a free-falling object starting from rest under the action of gravity and subject to no drag, namely

$$\Delta H = v_0 t - g t^2, \tag{2.18}$$

where ΔH is the variation in height (position) of the particle, v_0 is the particle's initial velocity (in our case, 0), g is the acceleration of gravity and t is the time passed from the moment the particle was "dropped", i.e., the start of the simulation. In Figure 2.7 we show in dashed lines with hollow circles the height of the particle for two different time steps, 10^{-6} in black and 10^{-5} in orange (which was only used for this analysis). The solid blue line represents Eq. (2.18). We see that the three curves align very closely up until T surpasses 0.20, when the particle starts going upwards due to the magnetic force of the bottom wall, thus reassuring that the integration provided by the method is correct.

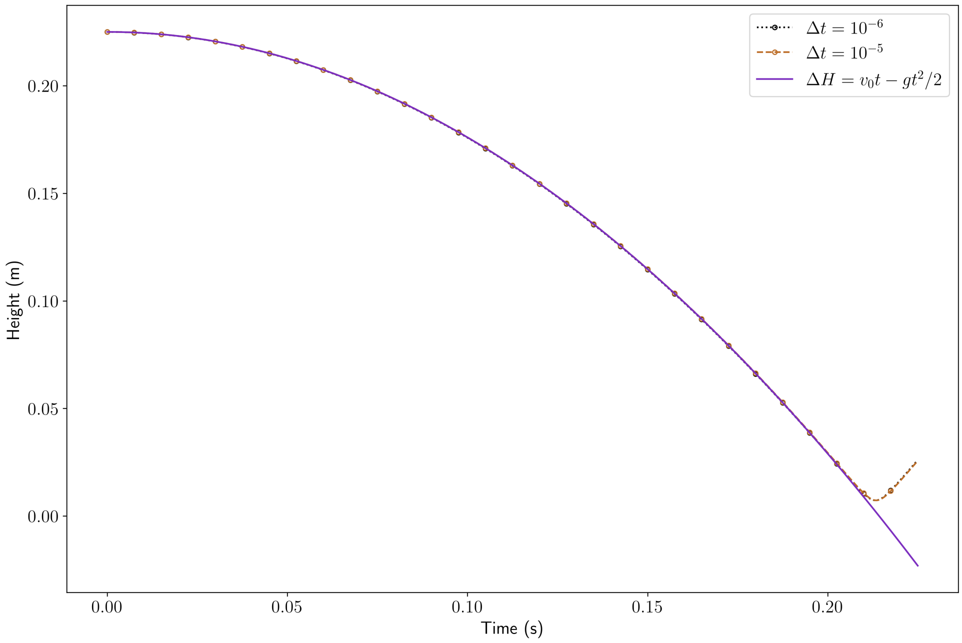

Figure 2.7 Particle height during the free fall for two different time steps h (dashed lines) versus the expected behaviour given by Eq. (2.18). We see the very close agreement between the three curves up until the particle "bounces" upwards due to the bottom wall magnetic force.

In Figure 2.8 we exhibit a convergence and order plot of the method. We plot a log-log plot of the error of each time step relative to the finer time step ($h = 10^{-8}$) at $T = 2$ versus the time step (h), shown in the blue dots. In orange we show the best fit line, which had angular coefficient of 2, thus confirming that the integration method used is of order 2. We note, nonetheless, the small oscillations of the points from the line, which we believe that can be attributed to the fact that we are computing relative and not absolute errors.

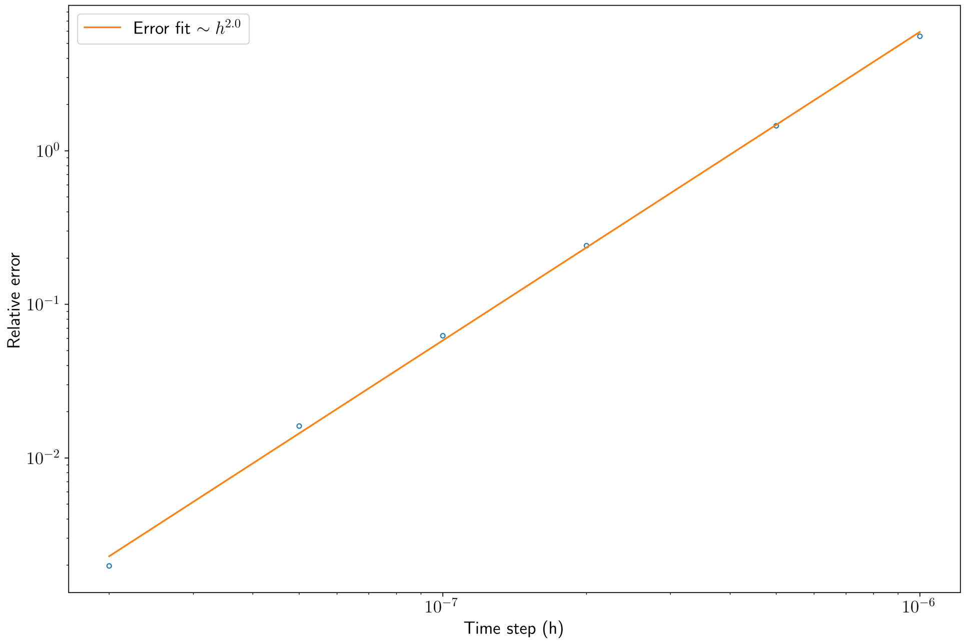

Figure 2.8 Log-log plot of the error of each time step relative to the finer time step ($h = 10^{-8}$) at $T = 2$ versus the time step (h) (blue dots). In orange the best fit line, which has angular coefficient of 2.

2.3.4.2 Energy conservation

Since the Störmer-Verlet method is symplectic, it dispersion of energy of the system takes longer simulation times than non-symplectic methods such as Euler's method. To verify this behaviour, we show Figures 2.9 and 2.10.

Figure 2.9 shows the phase diagram of the particle, that is, its velocity versus its position throughout the simulation. One sees that almost no spread can be oserved, which is indicative of the energy preserving behaviour of the method. To further corroborate this, Figure 2.10 exhibits a zoomed in portion of the phase diagram, showing that there is some energy variation, but ina very slow pace.

Lastly, to better qualify how little the energy of the system varies using this method, we present Fig. 2.11. It shows the particle's height in the first few stages of the simulation. We see that the peak height after each "bounce" is practically the same, confirming that very little energy is being lost or created after each "bounce". To better quantify how little this variation is, we note that the greatest difference between two peaks was of $6.8 \cdot 10^{-9}$ meters, that is, $1.36 \cdot 10^{-6}$ particle diameters.

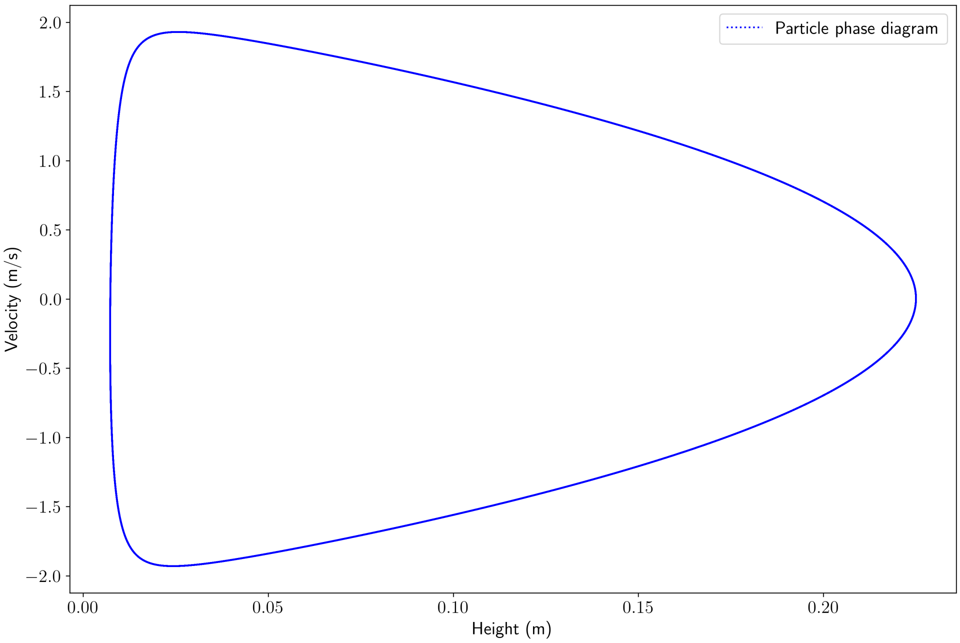

Figure 2.9 Particle's phase diagram exhibiting very little energy dissipation.

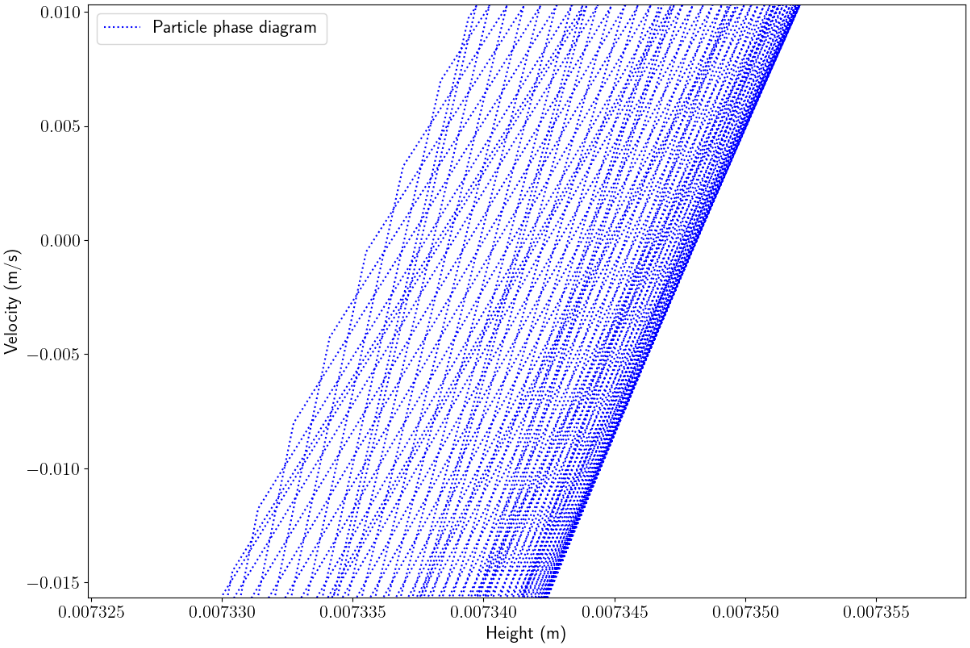

Figure 2.10 Zoom-in on the particle phase diagram, exhibiting the very slow pace of energy dissipation.

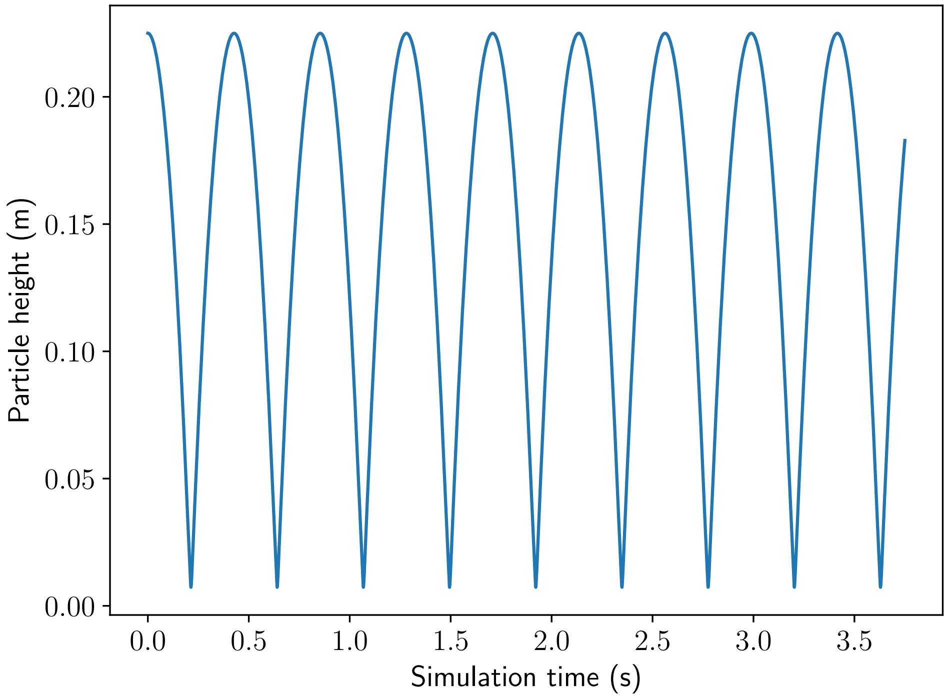

Figure 2.11 Particle's height in the first few stages of the simulations for the finer time step ($h = 10^{-8}$).

CHAPTER 3

MATHEMATICAL MODELLING OF REPELLING MAGNETIC PARTICLES

> "The greatest strategy is doomed if it's implemented badly."
>
> — Bernhard Riemann

3.1 Building upon previous work: a systematic approach

Previous work [15] investigated the compression and expansion dynamics of a two-dimensional granular bed composed of cylindrical repelling magnets, highlighting the role of dry friction and magnetic interactions in shaping the system's response. By combining experiments and numerical simulations, the authors demonstrated that the force on the piston follows distinct exponential trends during compression and expansion, with a notable sensitivity to the initial packing conditions. Fig 3.1 shows the comparison between simulations and experimental data.

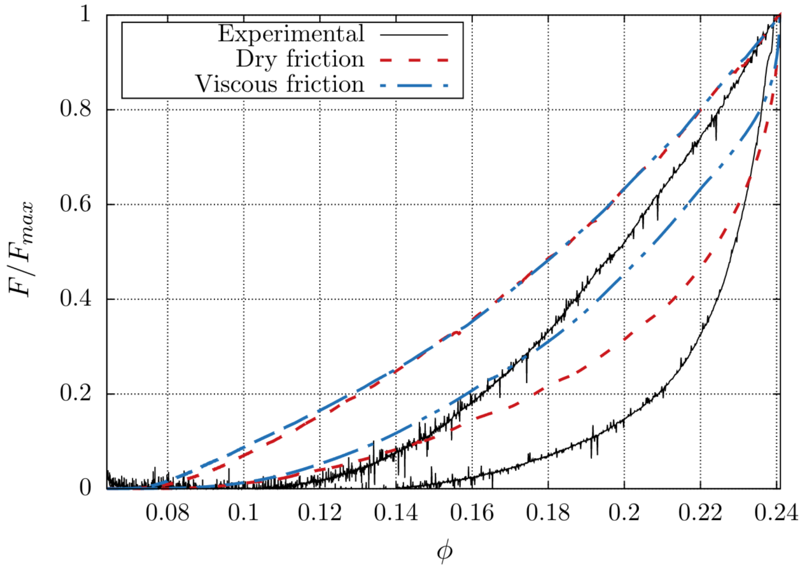

Figure 3.1 Exponential trends of the piston during the compression and expansion showing the normalized force on the piston as a function of the packing fraction ϕ of the system. Figure extracted from [15].

Unlike conventional granular materials, where force chains and stick-slip motion govern compaction, the magnetic system exhibited continuous force growth and density inversion effects, that is, a smaller density at the center of the cell, suggesting unique structural rearrangements due to the strong short-range repulsive interactions, as shown in Fig. 3.2.

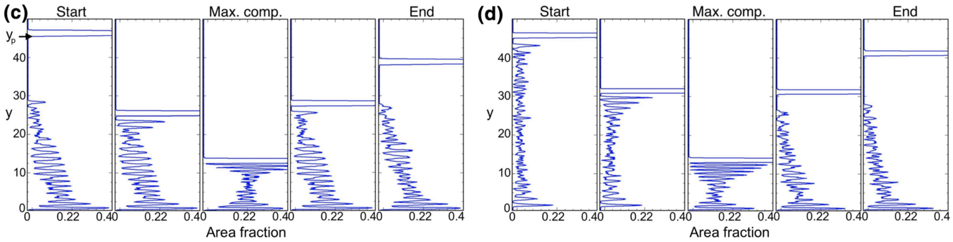

Figure 3.2 Local area fraction profiles obtained from two snapshots in [15]. The profiles indicate the area occupied by particles in a row at a given depth y. Note the density inversion observed close to the piston at the maximum compression. Figure extracted from [15].

Building upon these findings, in this chapter we conduct a systematic study of the simulation parameters, which are crucial to further understand the interplay between friction, packing conditions, and magnetic interactions in this system. By varying key parameters such as the friction coefficients, and system size, we explore their influence on the system's hysteresis, force evolution, and structural transitions. This approach will provide deeper insight into the fundamental mechanisms governing magnetically interacting granular materials and could contribute to optimizing their potential applications, such as in magnetic granular dampers, as will be discussed Chapter 5.

3.2 Independence on the initial conditions

To analyse the influence of the initial conditions on the results, we ran 10 simulations with $N = 368$ particles, with different random initial conditions and for the same piston velocity, namely $v = 5.63 mm/s$.

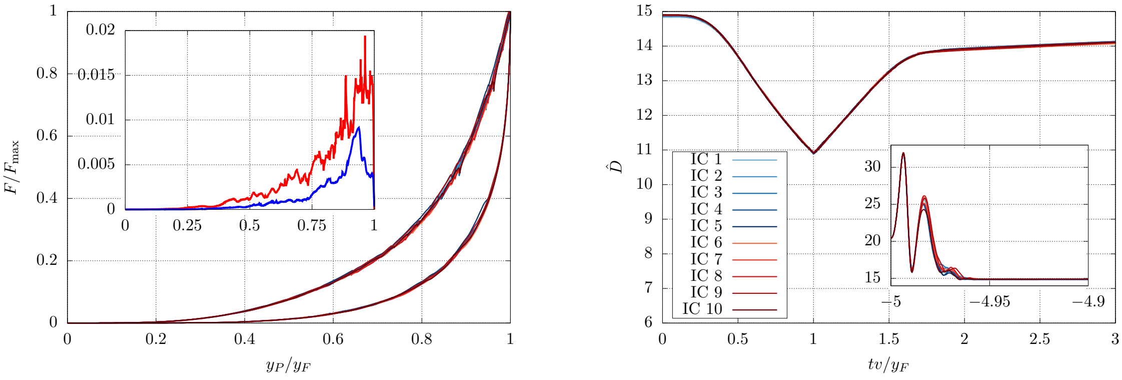

(a) (b)

Figure 3.3 (a) Piston force through the simulation for all 10 initial conditions. The x-axis represents the piston displacement y_P from the start of the compression relative to the maximum displacement y_F at maximum compression. The inset shows the behaviour of the standard deviation of the average force normalised by the mean maximum force, with the red portion corresponding to the compression and the blue portion corresponding to the expansion. All simulations were ran for the parameters given in Table 2.1. (b) Mean inter-particle distance for all 10 initial conditions. The inset shows the oscillations of $\hat{D}$ during the relaxation of the system. The x-axis represents the simulation time starting from the beggining of the compression (0) and ending at the end of the expansion (3).

Figure 3.3a shows that the different initial conditions cause different oscillations of the force, but the global behaviour of the system is preserved. This is also confirmed by the inset of Figure 3.3a that shows the standard deviation of the average force of the 10 initial conditions normalised by the mean maximum force of the 10 initial conditions. We can see that the standard deviation grows during the compression phase and decays during the expansion phase. Nevertheless, the maximum value of $\sigma(\overline{F}/\overline{F}_{\max})$ is ≈ 0.02, which is very small and indicates that the specific positions of the particles in the initial condition are not relevant for the overall dynamics of the system. Also, the standard deviation of the forces at the maximum compression, $\sigma(F_{\max})$, is ≈ 0.001, which is again very small (since the average of $F_{\max}$ is 15.26N) and indicative of the same behaviour.

Finally, Figure 3.3b shows that the behaviour of the mean inter-particle distance, $\hat{D}$, is also independent of the initial condition. This metric is nothing more than the sum of all inter-particle distances divided by the number of particles.

3.3 Dependence on the piston velocity

The influence of the piston velocity on the dynamics of the system is investigated as follows. Figure 3.4a shows that the dynamic of the compression-expansion cycle remains globally unaltered when the velocity of the piston is increased up to 128mm/s, the maximum value tested in this work, which is approximately 15 times the one used in [15].

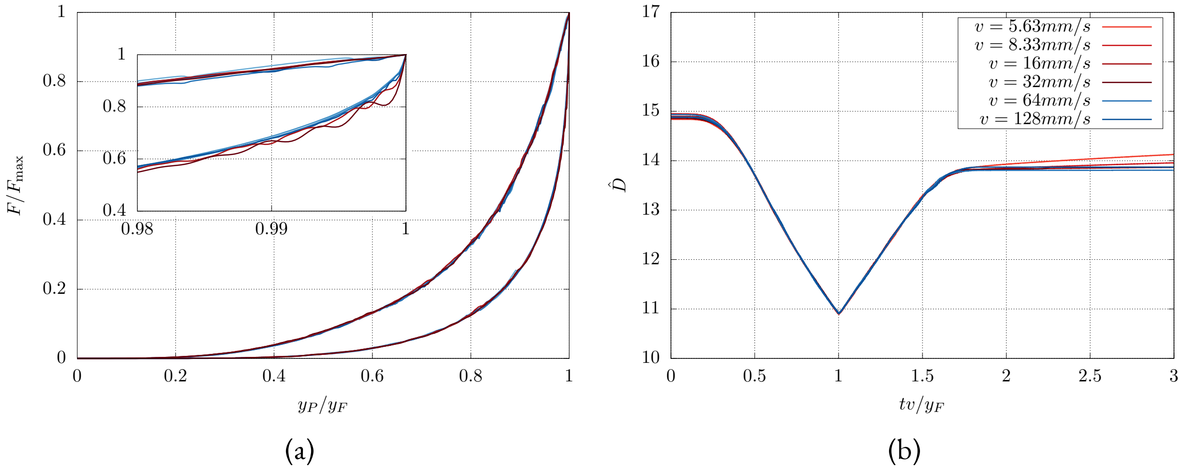

(a) (b)

Figure 3.4 (a) Compression-expansion cycle for several velocities in the dry model. The x-axis represents the piston displacement y_P from the start of the compression relative to the maximum displacement y_F at maximum compression. (b) Mean inter-particle distance of several velocities in the dry model. The x-axis represents the simulation time starting from the beggining of the compression (0) and ending at the end of the expansion (3).

The inset of Figure 3.4a shows a zoom into the region near the end of the compression and the beginning of the expansion. It is quite interesting to note that the force at the beginning of the expansion (which corresponds to the inferior part of the curve) oscillates more for higher velocities. On the other hand, during the compression phase the situation is reversed: we observe more abrupt changes in the force for smaller velocities. Both of these behaviours can be explained through the following heuristics: for compressions at high velocities, the particles have less time to adjust to the changing positions of the piston as it descends, so there are more abrupt motions of the particles that cause changes during this phase. On the other hand, when the piston goes up rapidly the force of the piston decreases very rapidly and the particles are free to move under small frictions and readjust to a new instantaneous equilibrium induced by the interaction with the neighbouring particles. The force of the piston then becomes important again and friction increases on the particles, causing some to remain static until the piston moves further away from them. This "stick-slip" motion is responsible for the oscillations during the expansion phase.

Finally, we analysed the dependence on the velocity of the mean inter-particle distance, showed in Figure 3.4b. We observe clearly that the global behaviour is the same as previously observed.

3.4 Dependence on the friction coefficients

Understanding the role of friction in our system is of crucial importance for accurately describing not only the behavior of the particles as individuals, but primarily the system as a whole, where rotational and translational motions are coupled. In many physical and computational models, friction forces are often approximated to simplify calculations while retaining the essential characteristics of the system, as will be the case in our work, to some degree. However, the choice of approximation can significantly influence the resulting dynamics, potentially altering both qualitative and quantitative predictions. To gain deeper insight into these effects, it is essential to assess the impact of higher-order corrections in the friction modelling and also the impact of the coefficients used.

In order to study how the friction affects the dynamics, we altered slightly the modelling of the friction forces. In [15], the authors consider a first order approximation for the torque between two dipoles. To see how the modelling of this friction force affects the system, we considered the second order term, $\hat{\mu}_i \times \hat{\mu}_j$, in Eq. (2.9). This gives

$$\tau_{ij} = \frac{\mu_0 \mu^2}{4\pi r_{ij}^3} \left[3\cos(\theta)\sin(\theta) + \sin(\theta)\right] = \frac{3\mu_0\mu^2}{8\pi r_{ij}^3}\left[\sin(2\theta) + \frac{2}{3}\sin(\theta)\right] \tag{3.1}$$

and, accordingly, changes Eq. (2.15) to

$$N_i = \frac{3\mu_0\mu^2}{8\pi} \cdot \frac{\sin(2\theta) + (2/3)\sin\theta}{\cos(\varphi+\theta)\sqrt{D^2+\varepsilon^2}} \sum_{j\neq i} \frac{1}{r_{ij}^3}. \tag{3.2}$$

With these two new formulae, we ran two new simulations: one with the new friction modelling, maintaining the same friction coefficients as previously in [15]; and one with the new friction modelling and high friction coefficients, namely $\mu_s = 0.8 = \mu_d$. We compared the results with our standard model.

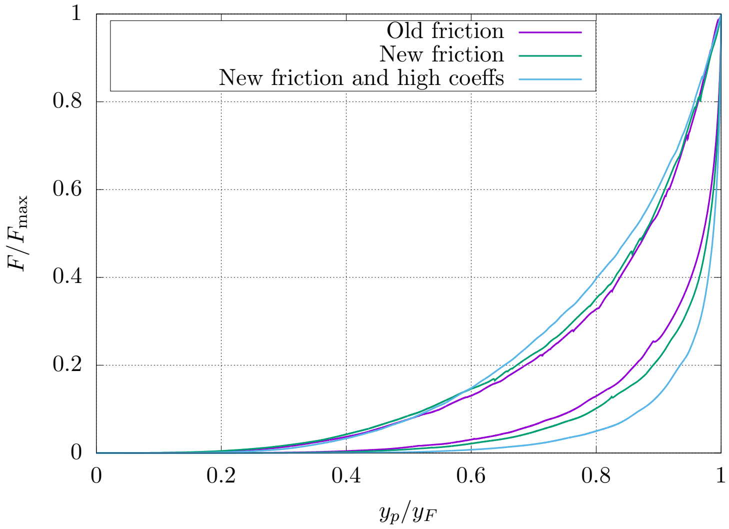

Figure 3.5 Normalised piston force versus piston stroke comparing the friction model established in [15] with our new friction. All simulations were done for a velocity of $v = 5.63$ mm/s. The x-axis represents the piston displacement y_P from the start of the compression relative to the maximum displacement y_F at maximum compression.

Figure 3.5 shows the behaviour of the normalised force versus the piston stroke during the compression/expansion. We see first that the old and new friction are quite similar, which corroborates to the fact that the first order approximation done in [15] is reasonable. Secondly, we see that the new friction with high coefficients has significant differences to the other two simulations, mostly in the expansion (bottom half of the curve). The behaviour shown is, indeed, expected: with a high dynamic friction coefficient, as the piston moves up during the expansion, the particles take longer to move and, therefore, they do not stay as close to the piston during the expansion as they do when the coefficients are lower, or when the approximation is of first order.

Figure 3.6 shows the mean inter-particle distance for our simulations with the friction, with the inset showing the variation of $\hat{D}$ during the initial relaxation of the system. This plot has a similar explanation than Figure 3.5: the old and new friction with the same coefficients behave similarly, with the new friction exhibiting a slightly greater hysteresis, while the new friction with high coefficients exhibit a much greater hysteresis, which is justified in the preceding paragraph.

The behaviour of the normalised force as a function of the packing fraction follows a very similar reasoning as the previous two plots, as shown in Figure 3.7. There is only one remark to add: with increased friction, the piston has to get closer to the particles to make them move in the compression, be it in the new friction with previous or higher coefficients. Therefore, to reach a given packing fraction, the piston has to exert more force the greater the friction is, which is shown in the upper half of the curves in Figure 3.7. During the expansion, the behaviour is reversed, as we explained in Fig. 3.5.

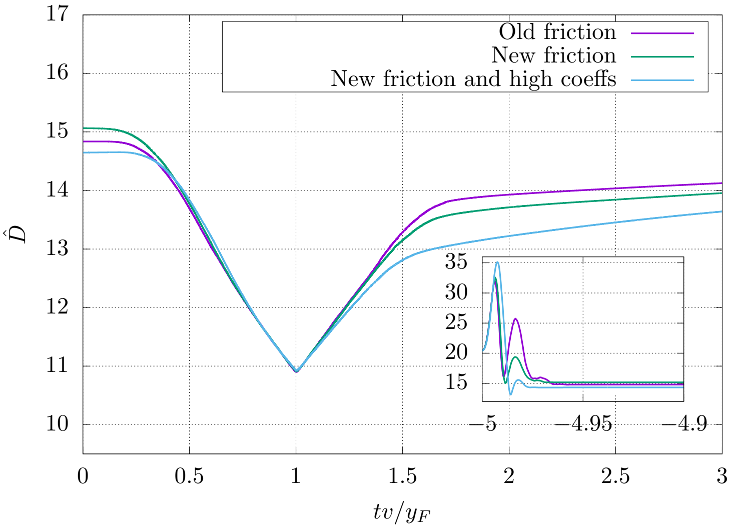

Figure 3.6 Mean inter-particle distance versus time comparing the friction models. All simulations were done for a velocity of $v = 5.63$ mm/s. The x-axis represents the simulation time starting from the beggining of the compression (0) and ending at the end of the expansion (3).

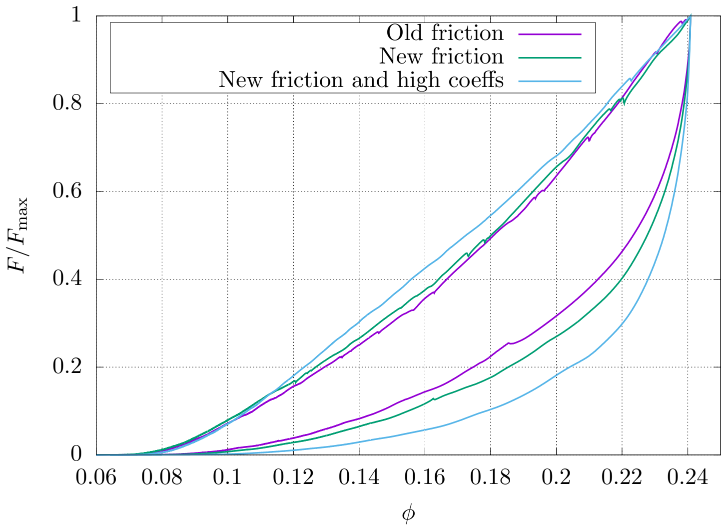

Figure 3.7 Behaviour of the normalised force as a function of the packing fraction comparing the friction models. All simulations were done for a velocity of $v = 5.63$ mm/s.

3.5 Dependence on the system's size

One of our main points of interest is to study the dynamics of the system as the number of particles grows. This, in particular, is interesting for the modelling of a magnetic damper, which is a clear possible application of our model.

As a first stride towards this goal, we ran a few simulations with a greater number and also with a smaller number of particles as compared to [15]. Namely, we ran our simulation increasing the number of particles by 92 at a time (which corresponds to 1/4 of 368, the original number of particles in [15]), ranging from 92 particles (a quarter of the original system) to 736 particles (double the original system).

For these simulations with different number of particles, we kept the geometry of the Hele-Shaw cell unaltered, only changing our system's dimensions and number of particles in such a way to keep ϕ unaltered at the maximum compression state. To be precise, if we want, say, aN particles in the system, we scale all linear dimensions by a factor of $\sqrt{a}$, so that the height, H, and width, W, of the Hele-Shaw cell are scaled by $\sqrt{a}$ and the piston starts the compression at a initial height scaled by $\sqrt{a}$, and it finishes the compression at a height also scaled by $\sqrt{a}$, as illustrated in Fig. 3.8.

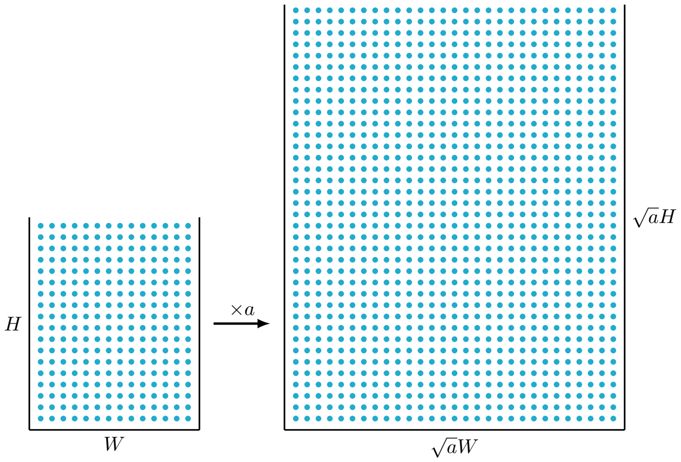

Figure 3.8 Illustration of how we scaled our system's size.

Therefore, the area occupied by the particles at the maximum compression state scales by a factor of a and, consequently, the packing fraction remains the same, since the number of particles is also scaled by a. Before discussing the results, we have to point out that, for our smallest system (92 particles), it was not possible to start the compression at 1/4 of the initial height, since the relaxed state of the granular bed attained a height higher than this initial height of the piston. So, in this particular case, we started the compression a bit higher and descended the piston to the expected height.

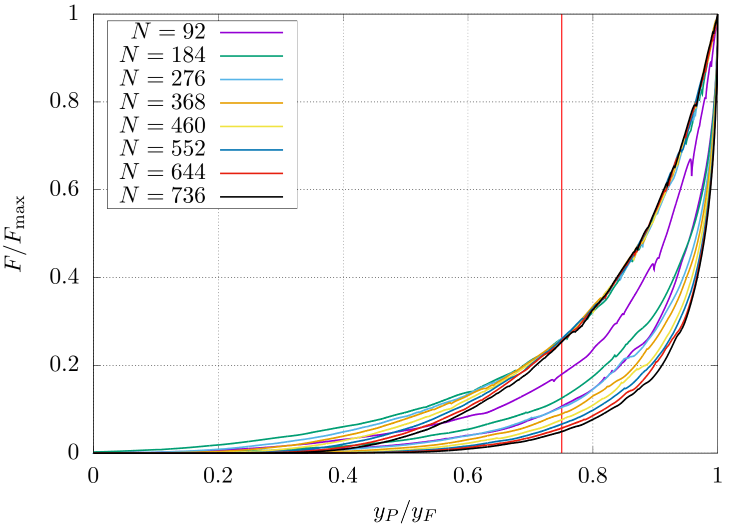

Figure 3.9 Behaviour of the force on the piston for several system sizes. We remark the similar behaviour across all sizes. All simulations were ran at a velocity of $v = 8.33$ mm/s. The vertical line at 0.75 represents, approximately, the point from which all systems behave very similarly during the compression.

Figure 3.9 shows the behaviour of the normalised force versus the piston stroke for all the system's sizes. We observe that the global behaviour is, again, the same, with a few differences from one size to another and, noticeably, a smoothing of the curves as the number of particles increases (compare the purple curve, for $N = 92$, to the black one, for $N = 736$, for example), probably because the absolute value of the force increases with the system size.

In the expansion phase, the curves begin to diverge quite early. This occurs because, in larger systems, the piston must travel a greater absolute distance. For instance, when $y_P/y_F = 0.8$, the piston in the system with 184 particles is closer (in absolute terms) to the top of the bed than in the system with 736 particles. As a result, the force ratio $F/F_{\max}$ is higher in the smaller system for the same piston position. We believe this also explains why, for $y_P/y_F \geqslant 0.75$, the compression behavior is the same across all systems, even though the curves are slightly spaced apart before reaching this point. This spacing arises because, in this simulation, the piston had to start compression from a relatively higher position compared to the other systems.

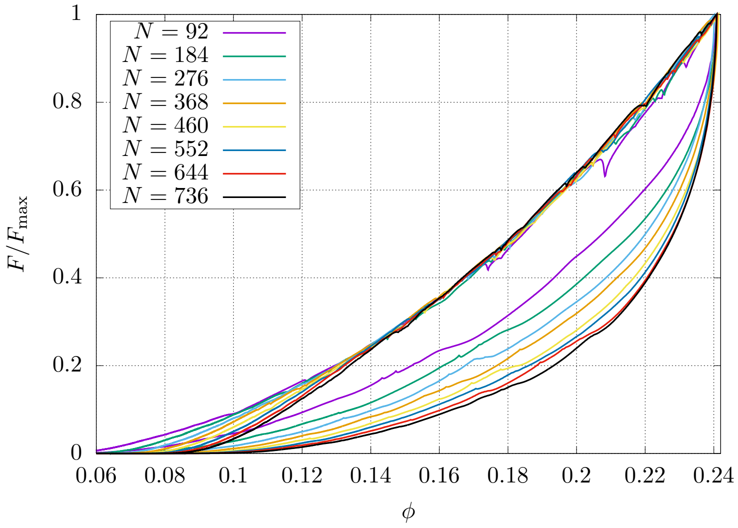

Figure 3.10 Behaviour of the normalised piston force as a function of the packing fraction of the system. We note that for $\phi \approx .14$, the compression on all systems is essentially the same. All simulations were ran at a velocity of $v = 8.33$ mm/s.

Nevertheless, as Figure 3.10 shows, we see that all the systems have the same packing fraction at the maximum compression and, furthermore, that for $\phi \approx 0.14$ on, all the systems exhibit the same behaviour during the compression (in terms of the packing fraction).

We point out that the purple curve, which corresponds to the 92 particles system, exhibits a seemingly different behaviour during the compression (note the three downward spikes). We think that the reason for this is quite simple: the fewer the particles, the farther away the system is from being “continous”, i.e., the particles can move more abruptly when they have fewer neighbours and forces fluctuations are important to the overall force. This also explains the smoothing shown in Figure 3.9 as N grows.

We also analysed how the mean distance between particles behaved as the system’s size varied, as shown in Figure 3.11. We observe that all the curves, as in the plot of the force, behave similarly. In this case, though, we see that as the number of particles increases, the hysteresis (i.e., the difference between $\hat{D}$ at beginning and end of the compression) of the system also increases. We believe this is due to the fact that the greater the number of particles, the greater the friction force on the system is, which in turn increases the resulting hysteresis.

To better show the increasing hysteresis through the different system sizes, we plotted the mean inter-particle distance normalised by the mean distance at the maximum compression state, $\hat{D}_{\min}$, as shown in Figure 3.12. We quantify the histeresis in Table 3.1. Wee see that although the absolute histeresis ($\hat{D}_{t=3} - \hat{D}_{t=0}$) increases with the system size, the normalised histeresis actually oscillates very little.

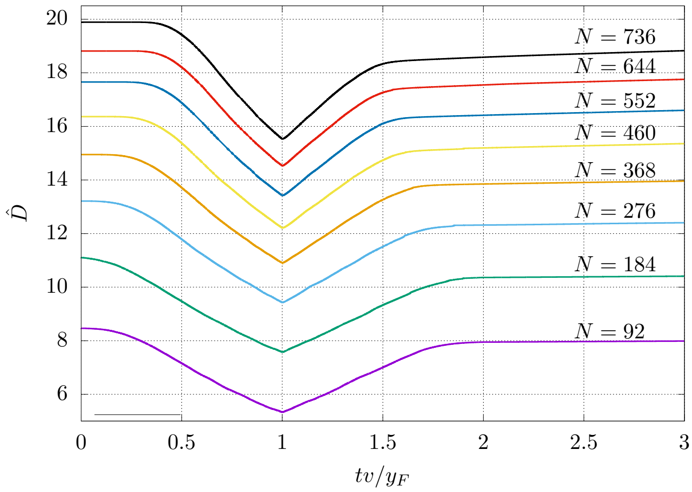

Figure 3.11 Mean inter-particle distance for the different system's size. We can see that, as the size increases, the hysteresis (difference between initial $\hat{D}$ and final $\hat{D}$) also increases. We do not exhibit the inset showing the relaxation of the system because, as shown in the plots above, it is already established that there are no significant changes in how the system relaxes in the dry model. All simulations were ran at a velocity of $v = 8.33$ mm/s.

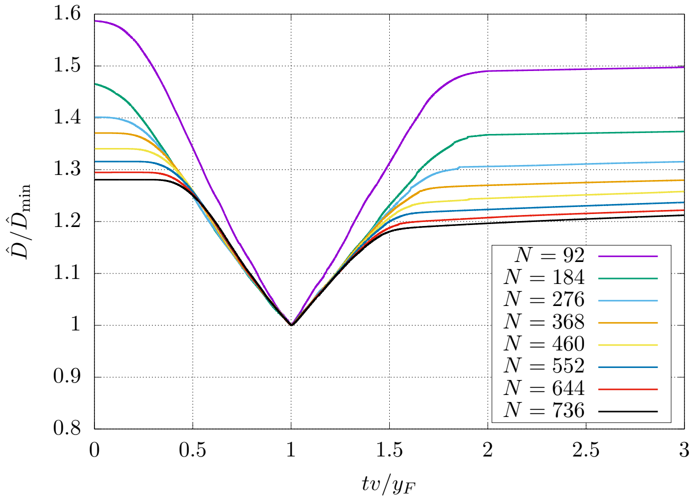

Figure 3.12 Mean inter-particle distance normalised by the mean distance at the maximum compression state for the different system's size. All simulations were ran at a velocity of $v = 8.33$ mm/s.

Table 3.1 Values for $\hat{D}$ in the different system sizes.

System	$\hat{D}_{\text{min}}$	$\hat{D}_{t=0}$	$\hat{D}_{t=3}$	$\hat{D}_{t=0}/\hat{D}_{\text{min}}$	$\hat{D}_{t=3}/\hat{D}_{\text{min}}$	$\hat{D}_{t=3} - \hat{D}_{t=0}$	$(\hat{D}_{t=3} - \hat{D}_{t=0})/\hat{D}_{\text{min}}$
92	5.33	8.46	7.99	1.59	1.50	0.48	0.09
184	7.58	11.10	10.41	1.47	1.37	0.70	0.09
276	9.43	13.21	12.40	1.40	1.32	0.81	0.09
368	10.90	14.95	13.96	1.37	1.28	0.99	0.09
460	12.21	16.36	15.36	1.34	1.26	1.01	0.08
552	13.42	17.66	16.60	1.32	1.24	1.06	0.08
644	14.53	18.81	17.76	1.29	1.22	1.06	0.07
736	15.53	19.89	18.82	1.28	1.21	1.06	0.07

We remark that, as it was the case in Figure 3.9, the curve for the 92 particles system stands out. The reason is the same as before: since the piston starts higher up (proportionally) than for the other systems, the initial mean distance is greater (and also the final mean distance, as the piston goes back to the initial compression height). As a final remark, we note that at this point, the simulations are executed with the “standard” algorithm, of $O(n^2)$. Therefore, it becomes increasingly more expensive and prohibitive to simulate larger and larger systems. This issue of performance/optimization will be discussed in Chapter 5.

Table 3.2 exhibits the average and standard deviation of the dimensional force on the piston at maximum compression for the standard simulations, with averages taken over 3 simulations for each system size.

Table 3.2 Average and standard deviation of the dimensional force (in Newtons) on the piston at maximum compression for the standard simulations. Averages taken on 3 simulations for each system size.

# particles	Avg. force ($O(n^2)$)	Std. ($O(n^2)$)
368	15.26	0.24
460	17.63	0.12
552	19.44	0.19
644	21.33	0.17
736	23.23	0.14

In Fig. 3.13 we plot the data of this table, together with the best fit line. We see a good linear trend, with the linear fit having $R^2 = 0.997$.

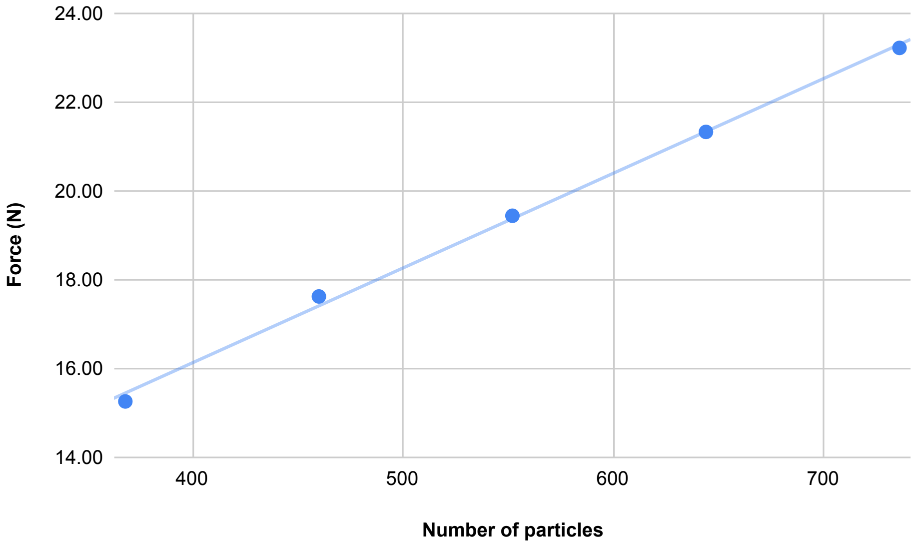

Figure 3.13 Force vs system size for the systems explored in this section. We see a good linear trend, with best fit line in light blue havin $R^2 = 0.997$.

3.6 An attempt to improve the force of the walls

The law in Eq. (2.8), as explained in [15], is completely experimentally-based. In that work, the authors attemped to use the force that an infinite wall exerts on a dipole, given by

$$F^i_{pw_\infty} = \frac{\mu_0 \mu^2}{\pi} \sum_j \frac{1}{r^3_{ij}}. \tag{3.3}$$

However, running simulations with this law did not produce results similar enough to the experiments.

The experimentally-based law captures well the overall behaviour of the system, but there is not a proper physical model or explanation supporting the power law dependence of 3.5. Let's propose, in this section, a new model that considers the wall as a finite magnetic slab.

We shall consider the geometry shown in Figure 3.14. In this situation, the point dipole feels a magnetic force element in the x direction exerted by dm which is given by

$$\mathrm{d}F_x = \frac{3\mu_0 \mu}{4\pi r^4} \sin\theta \mathrm{d}m, \tag{3.4}$$

with

$$r^2 = \ell^2 + y^2, \quad \theta = \arctan\left(\frac{\ell}{y}\right), \tag{3.5}$$

so we can rewrite

$$r = \frac{\ell}{\sin\theta}, \quad y = -\ell\cot\theta, \quad \frac{\mathrm{d}y}{\mathrm{d}\theta} = \frac{\ell}{\sin^2\theta}. \tag{3.6}$$

The negative sign on the expression for y comes from the fact that when $0 < \theta < \pi/2$, we have $y < 0$ and $\cot\theta > 0$ and, when $\pi/2 < \theta < \pi$, we have $y > 0$ and $\cot\theta < 0$. With this, we can write our differential forms as

$$\mathrm{d}y = \frac{\ell}{\sin^2\theta}\mathrm{d}\theta, \quad \mathrm{d}m = M\mathrm{d}y, \tag{3.7}$$

and this gives, after some cancellations,

$$\mathrm{d}F_x = \frac{3\mu_0 M\mu}{4\pi\ell^3}\sin^3\theta\mathrm{d}\theta. \tag{3.8}$$

Substituting $M = \mu/D$ and $\mathcal{J} = 3\mu_0\mu^2/4\pi$, we integrate the force element $\mathrm{d}F_x$ from θ_i to θ_f and obtain

$$F_x^W = -\frac{\mathcal{J}}{D\ell^3}\left(\frac{\cos^3\theta}{3} - \cos\theta\right)\Bigg|_{\theta_i}^{\theta_f} = -\frac{\mathcal{J}}{D\ell^3}\left[\frac{1}{3}\cos^3\left(\theta_f\right) - \cos\left(\theta_f\right) - \frac{1}{3}\cos^3\left(\theta_i\right) + \cos(\theta_i)\right], \tag{3.9}$$

with $\mathcal{J} = 3\mu_0\mu^2/4\pi$ and

$$\theta_i = \arctan\left(\frac{\ell}{fL}\right) = \arctan A, \tag{3.10}$$

$$\theta_f = \pi - \arctan\left(\frac{\ell}{(1-f)L}\right) = \pi - \arctan B, \tag{3.11}$$

considering, for simplicity, $\arctan(+\infty) = \pi/2$ and f to be the vertical distance of the dipole from the bottom of the bar in terms of the fraction of L that this distance represents and $A, B \in \mathbb{R}_+$, given by (see Fig. 3.14).

$$A = \frac{\ell}{fL}, \quad B = \frac{\ell}{(1-f)L}. \tag{3.12}$$

We can then simplify Eq.(3.9) using

$$\cos\left(\arctan x\right) = \frac{1}{\sqrt{x^2+1}}, \quad x \in (-\pi/2, \pi/2), \tag{3.13}$$

and Eqs. (3.10) and (3.11) to obtain:

$$F_x^W = -\frac{\mathcal{J}}{D\ell^3}\left[\frac{1}{3}\cos^3\left(\theta_f\right) - \cos\left(\theta_f\right) - \frac{1}{3}\cos^3\left(\theta_i\right) + \cos(\theta_i)\right] \tag{3.14}$$

$$= -\frac{\mathcal{J}}{D\ell^3}\left[-\frac{1}{3}\cos^3\left(\arctan B\right) + \cos(\arctan B) - \frac{1}{3}\cos^3\left(\arctan A\right) + \cos(\arctan A)\right] \tag{3.15}$$

$$= -\frac{\mathcal{J}}{D\ell^3}\left(\frac{1}{\sqrt{A^2+1}} + \frac{1}{\sqrt{B^2+1}} - \frac{1}{3}\frac{1}{A^2+1}\frac{1}{\sqrt{A^2+1}} - \frac{1}{3}\frac{1}{B^2+1}\frac{1}{\sqrt{B^2+1}}\right) \tag{3.16}$$

$$= -\frac{\mathcal{J}}{D\ell^3}\left[\frac{1}{\sqrt{A^2+1}}\left(\frac{3A^2+2}{3A^2+3}\right) + \frac{1}{\sqrt{B^2+1}}\left(\frac{3B^2+2}{3B^2+3}\right)\right]. \tag{3.17}$$

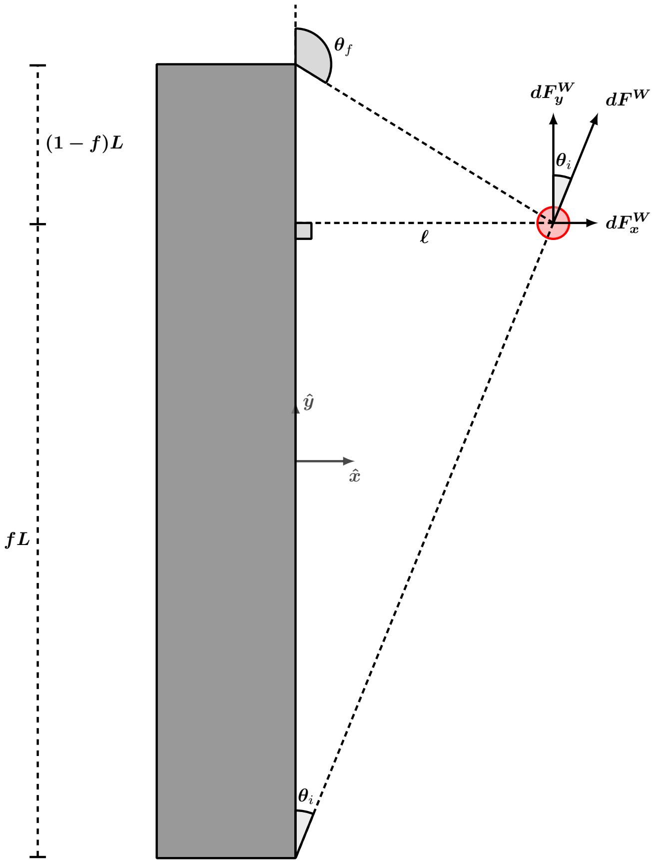

Figure 3.14 Sketch of the model considered for the finite wall.

We plotted the normalized force $F_x^W D/\mathcal{J}$ *vs.* ℓ in a log-log plot for fixed $L = 100D$ and several values of f. We also plotted the experimental dependence obtained in [15] and given by Eq. (2.8). The resulting plots are shown in Figure 3.15, which shows that $F_x^W \propto \ell^\alpha$, $\alpha < 0$, and also that α does not vary much for different values of f, as observed in the tan sheaf of lines; these lines were obtained for f varying from 0.005 to 0.995 with a step of 0.01 and ℓ in the range of 0.5 to 59 with a step of 0.01 as well, with a fit of the form $y = ax^b$. Moreover, we remark that the average of the values of α is ≈ -3.008. This shows that, although the wall is finite, we should not be too far out in modelling it as infinite, since for the infinite wall we have

$$A, B \xrightarrow[L\to\infty]{} 0 \tag{3.18}$$

$$F_x^W \xrightarrow[L\to\infty]{} -\frac{4}{3}\cdot\frac{\mathcal{J}}{D\ell^3}, \tag{3.19}$$

that is, $F_x^W \propto \ell^{-3}$, with the same constant of proportionality.

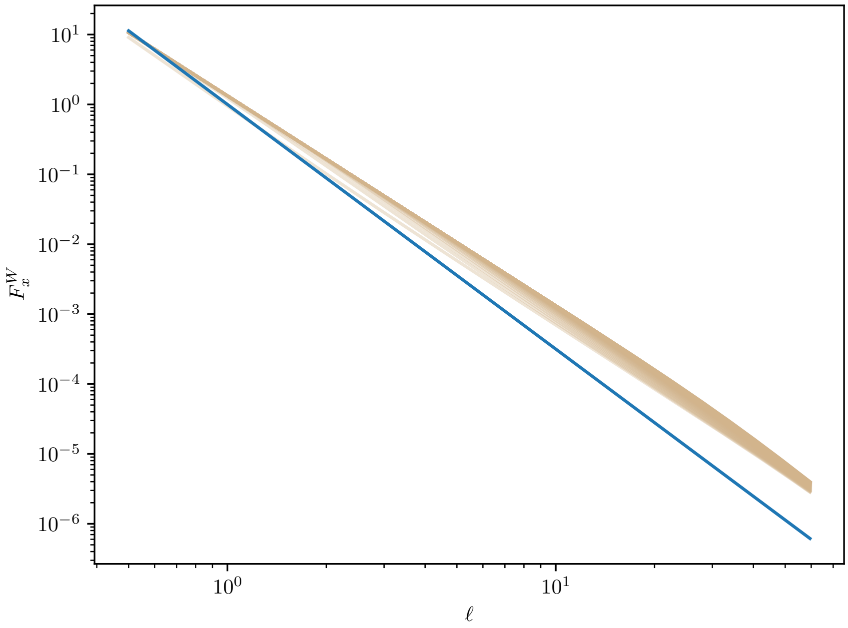

Figure 3.15 Log-log plot of the repulsion force versus ℓ. In blue we see the experimental form, Eq. (2.8).

In particular, we see that the expected proportionality, $F_x^W \propto \ell^{-3.5}$ given in Eq. (2.8), is not recovered by this model. This indicates that the mathematical model proposed in [15] for the particle-wall interaction is not capturing correctly the expected dependence on ℓ. We attribute this to two reasons: firstly, the edge effects that are present in the experiment are not considered, since we model an arrangement of magnets to be a solid bar; secondly, we believe that the experimental law given by Eq. (2.8) has the 3.5 exponent due to friction forces that were not considered in our modelling, such as the friction that the piston suffers and also other factors that are not directly linked solely to the nature of the magnetic interactions of the particles and the walls. However, when we attemped to model the walls as finite rectangular magnets and implemented this on our simulation code, the force of the bottom wall was not sufficient to sustain the bed of particles and, therefore, we could not perform any simulations.

3.7 Summary and comment on bi-disperse system

In this chapter, we systematically examined the influence of various model parameters on the qualitative and quantitative behavior of the system, thereby extending and complementing the analysis presented in [15]. Our investigation included exploring an alternative formulation for the wall-particle interaction force, confirming that the global dynamics of the system remain unaffected by the initial conditions of the particles, and analyzing the effects of friction, piston velocity, and system size on the overall behavior. These findings provide a more comprehensive understanding of the key mechanisms governing the system's dynamics and lay the groundwork for further refinements in modeling approaches.

In the next stage of this work, we will extend our analysis to a *bi-disperse system*, wherein the system consists of particles of two distinct sizes. While the fundamental modeling framework developed for the mono-disperse system remains applicable, modifications will be necessary to account for the interactions between the two different particle types. These adaptations, along with their effects on the system's behavior, will be discussed in detail in the following chapter.

Part II

Bi-disperse system: structural order

CHAPTER 4

BI-DISPERSE SYSTEM

> "A mathematician is a person who can find analogies between theorems; a better mathematician is one who can see analogies between proofs and the best mathematician can notice analogies between theories. One can imagine that the ultimate mathematician is one who can see analogies between analogies."
>
> — Stephan Banach

4.1 On systems with different kinds of particles: a brief overview of polidispersity

In this chapter we will explore a variation of the system studied in Part I that consists of introducing a second type of particle in the system, making it *bi-disperse*. This was motivated by our experimental work carried out in Japan by our collaborators [16]. This bi-disperse system is a particular case of general *poly-disperse* systems, that can have several different types of particles. This kind of system is a model to study ordering in crystals and can develop quasicrystals and structures that resemble DNA [16].

In Fig. 1.2 we show the experimental setup of the bi-disperse system [16]. The left figure is a frontal photo of the experimental setup, showing the Hele-Shaw cell with a compressed system. The central figure is a representation of the photo, showing the real dimensions of the cell and the two kinds of particles: big (5mm) and small (3mm). The right figure is a representation of the side view of the cell, again illustrating the two kinds of particles present in the system. Fig. 1.3 shows the initial and final configuration of the experimental compression of the granular bed for three different values of mixing of the two kinds of particles. We will denote the proportion of small particles by R, the mixing ratio. In the left figure we have a system with only big particles ($R = 0$); in the center we have a system with only 5% of small particles ($R = 0.05$) and in the right we have a system with half big and half small particles ($R = 0.5$). The ratio between the small particles diameter to the big particles diameter is called the *aspect ratio* of the system, and we will denote this quantity by a. The experimental work was conducted for small particles having 3mm in diameter and big particles having 5mm in diameter, i.e., for a system with aspect ratio $a = 3/5 = 0.6$. Experimentally, it is very labour intensive and expensive to work with systems with different aspect ratios. Numerically, working with different values of a is very simple and cheap.

Furthermore, our numerical setup allowed us to explore aspects that were not explored in the experiments conducted in [16]. Namely, we investigated the dynamics of the compression on this bidisperse system, as we did for the monodisperse system; the distances between particles (which is particularly hard to do in the experiments, but very easy in simulations); and we also explored the effects of using a viscous friction model and removing gravity, as we will see in Subsection 4.3.3. These last variations are also very hard to be carried out experimentally, since they are equivalent to having the particles neutrally buoyant in an interstitial fluid, which would have to be able to flow out of the cell in a given rate in order to keep the particles neutrally buoyant as the piston compresses the bed.

4.2 Mathematical modelling of the system

4.2.1 Setup and governing equations

Following our previous work [15] and the discussion in Part I, the governing equations of the system are given by Newton's second law of motion applied to each particle:

$$m_i \frac{d^2 r_i}{dt^2} = F_F^i + F_g^i + F_M^i, \tag{4.1}$$

with m_i being the mass of the i-th particle and $r_i(t) = (x_i(t), y_i(t))$ its position at an instant t. Furthermore, F_F^i represents the friction force that opposes the movement of the i-th particle, F_g^i represents the weight of particle i and F_M^i represents the magnetic forces acting on the i-th particle, which are of two types: particle-particle interaction, F_{pp}^i, and particle-wall interaction, F_{pw}^i.

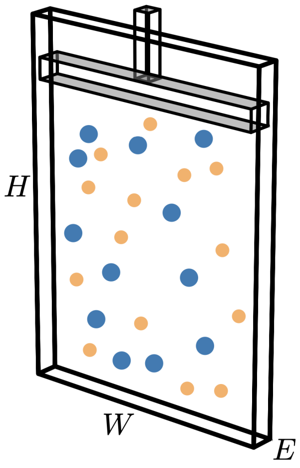

Figure 4.1 Illustration of the bi-disperse system (not to scale). Big particles are represented in blue and small particles are represented in orange.

The system is now bi-disperse, i.e., it is composed of two kinds of particles: big particles and small particles, as shown in Fig. 4.1. Except for the diameter of the particles and cell dimensions, all the remaining parameters contained in Table 2.1 remained unchanged for the bi-disperse system. The numerical Hele-Shaw cell dimensions were 33cm×44.5cm. The total number of particles was $N = 400$, with big particles having $D_1 = 5$mm of diameter and small particles having $D_2 = 3$mm in diameter.

The fundamental hypothesis made in this work is that the magnets are made of the same material, so that they have the same magnetization M. Since the magnetic dipole moment intensity of the

i-th particle is given by $\mu_i = MV_i$, where V_i is the volume of the particle, and since both types of particles have the same thickness ε, we can derive, for the two particle species in the system, the following equalities:

$$\frac{\mu_2}{\mu_1} = \frac{V_2}{V_1} = \frac{\pi D_2^2 \varepsilon/4}{\pi D_1^2 \varepsilon/4} = \left(\frac{D_2}{D_1}\right)^2 = a^2 = p, \tag{4.2}$$

where the subscripts 1 and 2 denote, respectively, the big and the small particles, and D_i stands for the diameter of the particles. The aspect ratio a, which is the square root of the parameter p of the particles, and which remained fixed in our experimental study [16], is one of the key parameters of the present investigation.

In the bi-disperse system, we consider that the force between particle i and particle j and the force that the walls exert on particle i are respectively given by

$$F^i_{pp} = \frac{3\mu_0}{4\pi} \sum_{\substack{j=1 \\ j\neq i}}^{N} \mu_i \mu_j \frac{\hat{r}_{ij}}{r_{ij}^4}, \quad \text{and} \quad F^i_{pw} = \frac{\mu_0 \mu_i M}{2\pi} \sum_{j=1}^{4} \frac{\hat{w}_{ij}}{w_{ij}^{3.5}}, \tag{4.3}$$

as discussed in Part I. Note, however, that in this case the magnetic moments, denoted by μ, are inside the summation in the particle-particle force expression and have an index in the particle-wall force expression. This is due to the fact that, since now there are two different kinds of particles in the system, we must have two different magnetic moments, one for each kind of particle.

We considered two types of friction in this study: dry friction, that accounts for the friction force with the walls, and viscous friction, that accounts for a fluid-like viscous drag resistance to the motion of the particles. The latter was successfully implemented in this model in our previous work [15], and proved to be crucial to predict the correct velocity-independent force in the piston during the compression of the granular bed. The former, which does not reproduce accurately this behaviour, is still kept in this work as a tool to generate a stratification free configuration, as it will be discussed later.

The friction models use here as the same used in the monodisperse case we studied in the previous chapter. The viscous friction model [33, 17, 15] assumes that the friction force is proportional to the velocity of the particle and that it opposes its motion, that is,

$$F^i_F = -\gamma v_i, \tag{4.4}$$

where γ is the viscous friction coefficient and v_i is the velocity of particle i.

The dry model is based on a regularized Coulomb model [29, 34] and is given by

$$F^i_F = \begin{cases} -F^i_T, & \text{if } |F^i_T| \leqslant \mu_e N_i \text{ and } |v_i| < v_t \\ -\mu_d N_i \dfrac{v_i}{|v_i|}, & \text{otherwise.} \end{cases}, \tag{4.5}$$

where

$$F^i_T = F^i_M + F^i_g, \tag{4.6}$$

μ_e and μ_d are the static and dynamic friction coefficients, respectively, and $N_i = |N_i|$ is the normal force due to the contacts of particle i with the walls. Also, v_t is a velocity threshold that characterizes negligible motion. As in our previous work [15], v_t is added to the denominator on the second condition to prevent divisions by zero in the numerical implementation. We have set this value to 10^{-6} [15].

The calculation of the normal force N_i depends on the contacts of the particles with the walls of the cell which, in turn, can be calculated from the torques acting on the particles. In fact, the torque acting on particle i caused by particle j is given by [31]

$$\tau_{ij} = \frac{\mu_0 \mu_i \mu_j}{4\pi r_{ij}^3} \left[3(\hat{\mu}_j \cdot \hat{r})(\hat{\mu}_i \times \hat{r}) + (\hat{\mu}_i \times \hat{\mu}_j) \right], \tag{4.7}$$

where $\hat{\mu}_i$ is the unitary magnetic dipole moment vector of the i-th particle and $\hat{r}$ is the unitary vector pointing from the center of particle i to the center of particle j. Using the same reasoning as in Subsection 2.2.3 but now with two different types of particles, we note that

$$\hat{\mu}_i \neq \hat{\mu}_j, \quad \|\hat{\mu}_j \cdot \hat{r}\| = \cos(\pi/2 - \theta_j) = \sin(\theta_j), \quad \|\hat{\mu}_i \times \hat{r}\| = \sin(\pi/2 - \theta_i) = \cos(\theta_i), \quad \|\hat{\mu}_i \times \hat{\mu}_j\| = 0. \tag{4.8}$$

Therefore,

$$\tau_{ij} = \frac{3\mu_0 \mu_i \mu_j}{4\pi r_{ij}^3} \cos(\theta_i) \sin(\theta_j), \tag{4.9}$$

with the angles $\theta_{i,j}$ the same as in Fig. 2.5, formed between the particles and the walls, given by

$$\theta_{i,j} = \arcsin\left(\frac{E}{\sqrt{D_{i,j}^2 + \varepsilon^2}} \right), \tag{4.10}$$

with E denoting the separation between the walls and $D_{i,j}$ denoting the two possible diameters. Thus, using the same balance equation as in Subsection 2.2.3, the normal force on particle i can be approximated by the sum of all torques acting on particle i as it was done for the monodisperse case, that is,

$$N_i = \frac{3\mu_0}{4\pi} \sum_{\substack{j=1 \\ j \neq i}}^{N} \mu_i \mu_j \frac{\cos(\theta_i) \sin(\theta_j)}{\cos(\varphi_i + \theta_i) \sqrt{D_i^2 + \varepsilon^2}} \cdot \frac{1}{r_{ij}^3}, \tag{4.11}$$

where we define the auxiliary angle

$$\varphi_i = \arctan\left(\frac{\varepsilon}{D_i} \right) \tag{4.12}$$

just as was done in Part I, Fig. 2.5. Note that the small particles have more room to rotate against the walls of the system, since their diameter is smaller: they are able to "tilt" more. At first sight, this could suggest that they experience a greater normal force and, consequently, a greater friction force proportionally. Nevertheless, this is not as straightforward as it seems, since the small particles have smaller magnetic dipole moment.

The computations are made using dimensionless equations that are obtained by dividing both sides of Eq. (4.1) by $m_1 D_1 / T^2$, with T being a characteristic time of the system, m_1 and D_1 the mass and diameter of the big particles. This results in the governing dimensionless numbers $\mathcal{G}_i$, $\mathcal{J}_{ij}$, $\mathcal{A}_{ij}$ and $\mathcal{D}_i$ that are related, respectively, to the gravity force, viscous friction, dry friction and magnetic forces. These numbers fully characterize the system and are given by:

$$\mathcal{G}_i = \alpha \frac{g T^2}{D_1}, \tag{4.13}$$

$$\mathcal{J}_{ij} = \beta \frac{\mu_0 \mu_1^2 T^2}{\pi m_1 D_1^5}, \tag{4.14}$$

$$\mathcal{A}_{ij} = \frac{3}{8} \cdot \frac{\sin(\theta_i + \theta_j) - \sin(\theta_i - \theta_j)}{\cos(\varphi_i + \theta_i) \sqrt{D_i^2 + \varepsilon^2}} D_1, \tag{4.15}$$

$$\mathcal{D}_i = \alpha \frac{\gamma T}{m_1} \tag{4.16}$$

with

$$D_i = \sqrt{\alpha} D_1, \tag{4.17}$$

$$\alpha = \begin{cases} 1, & \text{if the particle is big} \\ p, & \text{if the particle is small} \end{cases}, \tag{4.18}$$

$$\beta = \begin{cases} 1, & \text{if the interaction is between two big particles} \\ p, & \text{if the interaction is between a big and a small particle} \\ p^2, & \text{if the interaction is between two small particles} \end{cases} \tag{4.19}$$

The differences between these constants on the bi-disperse system to the mono-disperse system considered in Part I are listed in Table 4.1.

Table 4.1 Summary of the differences in the characteristic constants of the mathematical model between the bi-disperse system and the mono-disperse system considered in Part I.

Symbol	Previous expression	Bi-disperse expression	Physical interpretation
$\mathcal{J}$	$\frac{\mu_0 \mu^2 T^2}{\pi m D^5}$	$\beta \frac{\mu_0 \mu_1^2 T^2}{\pi m_1 D_1^5}$	Intensity of magnetic interactions
$\mathcal{A}$	$\frac{3}{8} \cdot \frac{\sin(2\theta) D}{\cos(\varphi + \theta) \sqrt{D^2 + \varepsilon^2}}$	$\frac{3}{8} \cdot \frac{\sin(\theta_i + \theta_j) - \sin(\theta_i - \theta_j)}{\cos(\varphi_i + \theta_i) \sqrt{D_i^2 + \varepsilon^2}} D_1$	Geometrical aspects of the system
$\mathcal{G}$	$\frac{g T^2}{D}$	$\alpha \frac{g T^2}{D_1}$	Gravitational pull
$\mathcal{D}$	$\frac{\gamma T}{m}$	$\alpha \frac{\gamma T}{m_1}$	Dissipation coefficient

Note that it would not be difficult to generalize the bi-disperse formulas for a poly-disperse system: in the case of r types of particles, one would define not p, but $p_1 = D_2/D_1, \dots, p_{r-1} = D_r/D_1$, and the α and β parameters would be represented by r and $\binom{r}{2}$ different cases, respectively, according to which pairs of particles they would refer to.

4.2.2 Defining the initial conditions and final compressed states

In the experimental work [16], the *mixing ratio*, R, is defined: this number represents the proportion of small particles in the system, ranging from 0 (only big particles) to 1 (only small particles). In contrast to the experiments in [16], instead of compressing the granular bed until the piston reached a 110N force we opted to impose the condition that the packing fraction ϕ at the maximum compression should be constant across all values of R. In a mono-disperse system ($R = 0$) with N_r big particles in a cell of dimensions $W_r \times H_r$, the packing fraction is given by the area of the cell occupied by the particles (assuming the system is 2D). Since the area of a particle is

$$\pi \frac{D_1^2}{4} \tag{4.20}$$

and the area of the cell is, in big particle diameters, given by

$$H_r W_r D_1^2, \tag{4.21}$$

we have that the packing fraction is given by

$$\phi_r = \frac{N_r \pi D_1^2/4}{H_r W_r D_1^2} = \frac{N_r \pi}{4 W_r} \cdot \frac{1}{H_r}. \tag{4.22}$$

Therefore, in a system with N_r particles, of which a proportion of R are small, in a cell of dimensions $H_r \times W_r$, the height of the piston at the maximum compression, H_f, such that the packing fraction is ϕ_r must satisfy

$$\frac{R N_r \pi D_2^2/4 + (1-R) N_r \pi D_1^2/4}{H_f W_r D_1^2} = \phi_r,$$

which is equivalent to

$$\frac{1 + R(p-1)}{H_f W_r} N_r = \frac{N_r}{W_r} \cdot \frac{1}{H_r},$$

that is,

$$H_f = \left[1 + R(p-1)\right] H_r. \tag{4.23}$$

Therefore, if we have the reference height H_r, we can alter the dimensions of the system and/or the mixing ratio of particles such as to keep the packing fraction unaltered using Eq. (4.23). Figure 4.2 illustrates how the genereation of the initial conditions for the bi-disperse system is carried out.

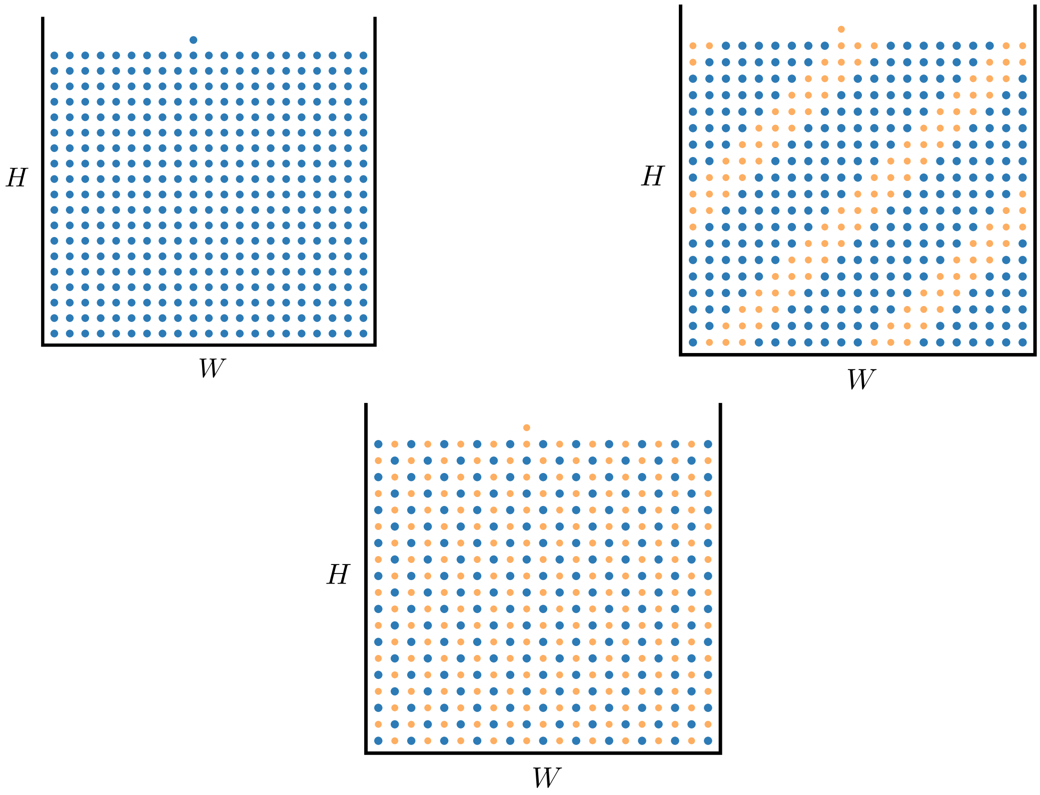

Figure 4.2 An illustration of the generation of the initial conditions for the simulations. In the left picture, the initial arrangement of the particles for the mono-disperse case corresponding to $R = 0$. In the right picture, the grid constructed to generate initial conditions for the case $R = 0.3$, with blue particles in blue and small particles in yellow. In the bottom picture, the grid to generate initial conditions for $R = 0.5$.

The big particles are drawn in blue and the small particles are drawn in yellow. Clockwise from the top left, we exhibit an illustration of the initial positioning for the generation of initial conditions for systems with $R = 0$, $R = 0.3$ and $R = 0.5$, respectively. We intersperse big and small particles according to the value of R in the following manner: given a value of R less than half, we check if the number of the particle being positioned is a multiple of $\lfloor 1/R \rfloor$; if it is, then that particle is small; if it is not, then that particle is big. For example, if $R = 0.3$, then $\lfloor 1/R \rfloor = 3$ so that particles 1 and 2 are big and particle 3 is small; particles 4 and 5 are big and particle 6 is small and so on. If R is greater than half, we check if the number of the particle being positioned is a multiple of $\lfloor 1/(1-R) \rfloor$; if it is, then that particle is big; if it is not, then that particle is small. For example, if $R = 0.7$, then $\lfloor 1/(1-R) \rfloor = 3$ so that particles 1 and 2 are small and particle 3 is big and so on. If $R = 0.5$, we alternate between big and small particles: particle 1 is big, particle 2 is small, particle 3 is big and so on.

4.2.3 Voronoi diagrams, Delaunay triangulations and convex hulls

We detain ourselves briefly to explain what are Voronoi diagrams together with its relations to Delaunay triangulations and convex hulls. This diagram will be utilised to analyse the ordering of the particles in our bidisperse system.

4.2.3.1 Definitions and properties

Definition 4.1 (Convex hull). The convex hull of a set X is the (unique) minimal convex set containing X.

If X is a finite collection of unaligned points in the Euclidean plane, the boundary of the convex hull is the simple closed curve with minimum perimeter containing X. One may imagine, for the 2D case, stretching a rubber band so that it surrounds the entire set and then releasing it, allowing it to contract; when it becomes taut, it encloses the convex hull of the set.

For objects in three dimensions, the first definition states that the convex hull is the smallest possible convex bounding volume of the objects.

Definition 4.2 (Voronoi diagram). Let X be a metric space with distance function d. Let K be a set of indices and let $(P_k)_{k\in K}$ be a tuple (ordered collection) of nonempty subsets (the sites) in the space X. The Voronoi cell, or Voronoi region, R_k, associated with the site P_k is the set of all points in X whose distance to P_k is not greater than their distance to the other sites P_j, where j is any index different from k. In other words, if $d(x, A) = \inf\{d(x, a) \mid a \in A\}$ denotes the distance between the point x and the subset A, then

$$R_k = \{x \in X \mid d(x, P_k) \leqslant d(x, P_j) \text{ for all } j \neq k\}. \tag{4.24}$$

The Voronoi diagram is simply the tuple of cells $(R_k)_{k\in K}$. It has numerous applications, ranging from the geometry of numbers, passing through crystallography and even biology. To put it simply, each cell in the Voronoi diagram represents the set of points which are neighbours to P_k in a given metric.

When X is a finite-dimensional Euclidean space, each site is a point, there are finitely many points and all of them are different, then the Voronoi cells are convex polytopes. We have precisely that in our setting, with $X = \mathbb{R}^2$ and $K = \{1, 2, \dots, N\}$ (where N is the number of particles in the system) and the Voronoi cells are, therefore, convex polygons.

Definition 4.3 (Delaunay triangulation, [35]). Given a Voronoi diagram where generator points are not collinear and their number is three or more but finite, we join all pairs of generator points whose Voronoi polygons share the common Voronoi edge. As a result, we obtain a second tessellation. If this tessellation consists of only triangles, we call it a Delaunay triangulation. If not, we call it a Delaunay pretriangulation. For the Delaunay pretriangulation, we partition non-triangular polygons into triangles by non-intersecting line segments joining the vertices. As a result, the Delaunay pretriangulation becomes a triangulation. We also call it a Delaunay triangulation.

One can obtain the Voronoi diagram from the Delaunay triangulation by marking the circumcenters of the triangles of the Delaunay diagram: they correspond to the vertices of the Voronoi diagram, and the edges are traced through circumcenters whose triangles share an edge.

With these three definitions, the following properties are immediate [36].

1. Convex hull: the boundary of the exterior face of the Delaunay triangulation is the boundary of the convex hull of the point set.

2. Circumcircle property: the circumcircle of any triangle in the Delaunay triangulation is “empty”, that is, the interior of the associated circular disk contains no sites of P.

3. Empty circle property: two sites p_i and p_j are connected by an edge in the Delaunay triangulation if and only if there is an empty circle passing through p_i and p_j.

4. Closest pair property: the closest pair of sites in P are neighbors in the Delaunay triangulation.

5. Combinatorial Complexity: given a point set P with n sites where there are h sites on the convex hull, it is not hard to prove by Euler’s formula that the Delaunay triangulation has $2n - 2 - h$ triangles and $3n - 3 - h$ edges. Generally, in $\mathbb{R}^d$ the number of simplices (the d-dimensional generalization of a triangle) can range from $O(n)$ up to $O(n^{\lceil d/2 \rceil})$. For example, in $\mathbb{R}^3$ the Delaunay triangulation of n sites may have as many as $O(n^2)$ tetrahedra.

4.2.3.2 Calculating the diagram computationally

The library used for computing the Voronoi tessellation is SciPy. This library, in turns, uses the Qhull library for computing the Voronoi diagram, i.e., the Qhull library does the “hardwork” of computing the diagram. It does so by first computing the Delaunay triangulation of the set of points and, then, extracts the Voronoi diagram from it [37], “Qhull computes the Voronoi diagram via the Delaunay triangulation. Each Voronoi vertex is the circumcenter of a facet of the Delaunay triangulation. Each Voronoi region corresponds to a vertex (i.e., input site) of the Delaunay triangulation.” (the Delaunay triangulation and the Voronoi diagram are dual graphs, with the circumcenters of the triangles of the first being the vertices of the regions of the second.).

According to the documentation [37], “Qhull computes the Delaunay triangulation by computing a convex hull. It lifts the input sites to a paraboloid by adding the sum of the squares of the coordinates. It scales the height of the paraboloid to improve numeric precision (‘Qbb’). It computes the convex hull of the lifted sites, and projects the lower convex hull to the input.”

We will show that this process of lifting the points to a paraboloid, computing the convex hull of the lifted points and then projecting the “lower-half”, i.e., the downward-pointing facets, gives you the Delaunay triangulation of the original set of points, as illustrated in Fig. 4.3.

Definition 4.4 (Delaunay condition, [36]). Three points $p, q, r \in P$ form a Delaunay triangle if and only no other point of P lies within the circumcircle of the triangle defined by these points.

Definition 4.5 (Convex hull condition, [36]). Three points $p^{\uparrow}, q^{\uparrow}, r^{\uparrow} \in P^{\uparrow}$ form a face of the convex hull of $P^{\uparrow}$ if and only if no other point of $P^{\uparrow}$ lies below the plane passing through $p^{\uparrow}, q^{\uparrow}$ and $r^{\uparrow}$.

Figure 4.3 The projection of the lower-half of the convex hull giving the Delaunay triangulation. Figure reproduced from [36, p. 80].

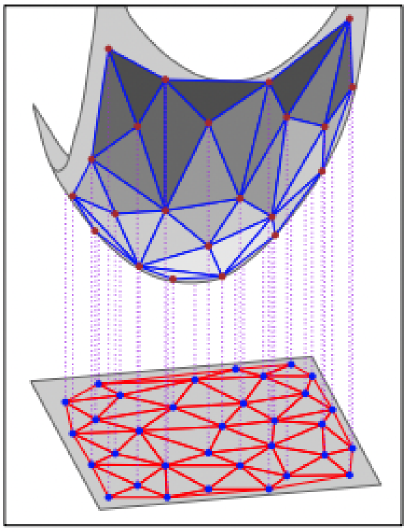

Lemma 4.1. Consider four distinct points p, q, r, and s in the plane, and let $p^\uparrow$, $q^\uparrow$, $r^\uparrow$, and $s^\uparrow$ denote their respective vertical projections onto the paraboloid $\mathcal{P}$ given by $z = x^2 + y^2$. The point s lies within the circumcircle of $\triangle pqr$ if and only if $s^\uparrow$ lies beneath the plane passing through $p^\uparrow$, $q^\uparrow$ and $r^\uparrow$.

Proof. Consider an arbitrary nonvertical plane in space that is tangent to $\mathcal{P}$ at $(a, b, a^2 + b^2)$, as illustrated in Fig. 4.4. The equation of this plane is of the form

$$z = 2ax + 2by + \gamma,$$

since the gradient of $z = x^2 + y^2$ is $(2x, 2y)$. Using the fact that the point $(a, b, a^2 + b^2)$ is in the plane, we obtain

$$a^2 + b^2 = 2a^2 + 2b^2 + \gamma \iff \gamma = -(a^2 + b^2).$$

Therefore, the plane has equation

$$z = 2ax + 2by - (a^2 + b^2).$$

Now, if we shift it upwards by r^2 we obtain the plane of equation

$$z = 2ax + 2by - (a^2 + b^2) + r^2,$$

whose intersection with $\mathcal{P}$ is given by

$$x^2 + y^2 = 2ax + 2by - (a^2 + b^2) + r^2 \iff (x - a)^2 + (y - b)^2 = r^2,$$

which is a circumference centered at (a, b)! This shows that the intersection of $\mathcal{P}$ with a plane gives a plane curve (in fact, an ellipse) that, when projected to the xy plane, is a circumference centered at

(a, b) with radius r. We conclude that the intersection of an arbitrary lower halfspace with $\mathcal{P}$, when projected to the xy plane, is the interior of a circle.

To prove the lemma, observe that the lifts $p^\uparrow$, $q^\uparrow$ and $r^\uparrow$ define a (unique) plane Π. By what we just showed, p, q, r lie on the circumference that is the projection of $\Pi \cap \mathcal{P}$. Therefore, the circle defined by this circumference is the unique one through p, q and r, so that s is within it if and only if its projection $s^\uparrow$ is within the lower halfspace of Π. □

Figure 4.4 Illustration of the proof of Lemma 4.1. Figure reproduced from [36, p. 82].

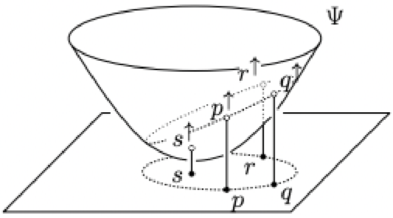

With this, we can prove the main assertion.

Theorem 4.1 (Delaunay and Convex hulls). Given a set of points P in the plane (assuming no four are cocircular), and given three points $p, q, r \in P$, the triangle $\triangle pqr$ is a triangle of the Delaunay triangulation of P if and only if triangle $\triangle p^\uparrow q^\uparrow r^\uparrow$ is a face of the lower convex hull of the lifted set $P^\uparrow$.

Proof. From the definition of Delaunay triangulations we know that $\triangle pqr$ is in the Delaunay triangulation if and only if there is no point $s \in P$ that lies within the circumcircle of $\triangle pqr$. From Lemma 4.1, this is equivalent to saying that there is no point $s^\uparrow$ that lies in the lower convex hull of $P^\uparrow$, which is equivalent to saying that $\triangle p^\uparrow q^\uparrow r^\uparrow$ is a face of the lower convex hull, completing the proof. □

Remark 4.1. The documentation says that "After scaling with option 'Qbb', the lower bound of the last coordinate will be 0 and the upper bound will be the maximum width of the other coordinates. Scaling happens after projecting the points to a paraboloid and scaling other coordinates. Option 'Qbb' should be used for Delaunay triangulations with integer coordinates. Since the last coordinate is the sum of squares, it may be much larger than the other coordinates."

Also [37], "Qhull implements the Quickhull algorithm for computing the convex hull. It handles roundoff errors from floating point arithmetic. It computes volumes, surface areas, and approximations to the convex hull."

So, the step-by-step of Qhull to compute the Voronoi diagram of a set of points in the Euclidean plane is the following:

Table 4.2 Flow of steps performed by Qhull to compute the Voronoi diagram.

Lift set of points to $\mathcal{P}$

↓

Compute the convex hull of the lifted points

↓

Project the lower-half of the convex hull, obtaining the Delaunay triangulation

↓

Compute the Voronoi diagram via circumcenters in the Delaunay triangulation

4.2.3.3 The Quickhull algorithm

The Quickhull algorithm is an approach for computing the convex hull of a finite set of points in *d*-dimensional space. It uses a divide and conquer approach similar to that of the quicksort algorithm, hence its name.

The *d*-dimensional Quickhull was invented in 1996 by C. Bradford Barber, David P. Dobkin and Hannu Huhdanpaa [1]. It was an extension of Jonathan Scott Greenfield's 1990 planar Quickhull algorithm, although the 1996 authors did not know of his methods [38]. Instead, Barber et al. describe it as a deterministic variant of Clarkson and Shor's 1989 algorithm.

4.2.3.4 About the coloring of the Voronoi diagram

We introduce a coloring of the regions based on the number of sides it has: regions with 5 or less sides are grey, hexagons are green and regions with 7 or more sides are red. The darker the green color of the hexagons, the more regular they are, following the expression

$$\mathcal{R} = \frac{4}{\sqrt{3}} \cdot \frac{A}{\sum_k \ell_k^2}, \tag{4.25}$$

that is, a constant times the area of the region divided by the sum of the square of the side lengths. Using this metric, regular hexagons with side length ℓ have

$$\mathcal{R} = \frac{4}{\sqrt{3}} \cdot \frac{6\ell^2\sqrt{3}/4}{6\ell^2} = 1, \tag{4.26}$$

and irregular hexagons have $\mathcal{R} < 1$.

We thought about using the area-to-perimeter ratio as a metric of regularity, i.e.,

$$\mathcal{R}'_{\text{hex}} = \frac{4}{\sqrt{3}} \cdot \frac{A}{\left(\sum_i \ell_i\right)^2}. \tag{4.27}$$

However, since $0 < \mathcal{R}'_{\text{hex}} \leqslant 1/6$, we opted to use the metric given in Eq. (4.26) since it possess a wider range of variation, allowing for finer subtleties in the color gradient. This reflexion and discussion of possible metrics was conducted in StackOverflow, an open forum of discussion [39].

Algorithm 4.1 Quickhull algorithm for a convex hull in $\mathbb{R}^d$. Extracted from [1].

```
create a simplex of $d + 1$ points
for each facet $F$ do
    for each unassigned point $p$ do
        if $p$ is above $F$ then
            assign $p$ to $F$'s outside set
        end if
    end for
end for
for each facet $F$ with non-empty outside set do
    select the furthest point $p$ of $F$'s outside set
    initialize the visible set $V$ to $F$
    for all unvisited neighbours $N$ of facets in $V$ do
        if $p$ is above $N$ then
            add $N$ to $V$
        end if
    end for
    the set of horizon ridges $H$ is the boundary of $V$
    for each ridge $R$ in $H$ do
        create a new facet from $R$ and $p$
        link the new facet to its neighbours
    end for
    for each new facet $F'$ do
        for each unassigned point $q$ in an outside set of a facet in $V$ do
            if $q$ is above $F'$ then
                assign $q$ to $F'$'s outside set
            end if
        end for
    end for
    delete the facets in $V$
end for
```

4.2.4 Defining and characterizing the order of the system

Furthermore, to characterize the ordering of the system we used both the Voronoi tessellation and the global orientational order parameter, Ψ_6, defined by [24, 25]

$$\Psi_6 = \left\langle \left| \frac{1}{n} \sum_{j=1}^{n} \exp\left(i6\theta_{ij}\right) \right| \right\rangle_i , \tag{4.28}$$

where n is the number of neighbours of the i-th particle, θ_{ij} is the angle between the horizontal axis and the segment joining the i-th to the j-th particle and $\langle \cdot \rangle_i$ denotes the average over all particles. This metric basically measures the ordering of the system as a whole: the expression inside the absolute value is a complex number whose magnitude, that is at most 1, represents, for each particle i, how close the arrangement of particle i and its neighbours is from a regular hexagon. When we average this quantity over all the particles, we obtain $\Psi_6 \leqslant 1$, that represents how close the system as a whole is to a perfectly crystaline structure formed only by regular hexagons[1]. This metric is widely used in crystallography [24, 25], in the context of studying regularities and defects in the strucuture of crystals as they change phase (in special, as they melt).

As in [16], the regions of the Voronoi tessellation considered in the analysis were the ones contained in the rectangle with vertices defined by the centers of the left-most, right-most, top-most and bottom-most particles.

Table 4.3 Default values (in SI units) for the parameters of the simulation. Properties given for the big particles.

Particle density (ρ)	7368.0
Particle width (ε)	0.003
Residual magnetization (B_r)	1.3
Cell height (H)	0.45
Cell width (W)	0.36
Wall separation (E)	0.0031
Vacuum magnetic permeability (μ_0)	$4\pi \cdot 10^{-7}$
Gravity acceleration (g)	9.8
Static friction coefficient (μ_e)	0.6
Dynamic friction coefficient (μ_d)	0.45

---

[1] As a sugestion from one of the members of the examining committee, we also looked at the radial distribution function (RDF) $g(r)$, a function that describes how the density of particles varies as a function of distance from a reference particle. If a system has a periodic RDF, this suggests that there is a regular structure to be observed in such system. If there is no such pattern to be observed in the RDF, so that it contains broader and less defined features, this suggests that there is no long-range order on the system. The former was the case in our work.

Algorithm 4.2 MD algorithm for the bi-disperse granular system.

```
initialize variables
open output files
position particles with a random initial velocity of the order of $10^{-2}$    ▷ this is done before the compression starts!
for $t \leqslant T_{\max}$ do
    if $k < T_r$ then
        descend the piston with an exponential law $\exp(t - 5)$    ▷ that is, the piston lowers smoothly during relaxation
    end if
    if $k = T_r$ then
        $H = H_0$    ▷ that is, when the relaxation ends the piston is positioned at the initial compression height
    end if
    if $T_r \leqslant k \leqslant T_b$ then
        $H = H - \Delta t \cdot V_c T / L$    ▷ that is, during the compression time we lower the piston by a constant factor
    end if
    for each particle $p$ do
        compute the magnetic force of the walls on $p$, with the $\alpha$ factor
        compute the gravitational force on $p$, with the $\alpha$ factor
        for every particle $q$ with index grater than $p$ do
            compute the magnetic force between $q$ and $p$, with the $\beta$ factor
        end for
        compute the friction force on $p$, with the $\varphi_p$ and $\theta_p$ angles
    end for
    save computed interactions on output files
    call the Verlet integration subroutine
    advance the time step
    update $k = k + 1$
end for
save last iteration computed interactions on output files
close output files
```

Algorithm 4.3 Algorithm for computing the Voronoi tessellation of the system.

```
read position file output by the simulation
retrieve the maximum and minimum $x$-coordinates and $y$-coordinates
calculate the Voronoi tessellation of the set of particles' 2D coordinates with Python's Voronoi class
for each polygon in the set of Voronoi cells do
    if polygon is inside the box of vertices $(x_{\min}, y_{\min})$, $(x_{\min}, y_{\max})$, $(x_{\max}, y_{\max})$, $(x_{\max}, y_{\min})$ then
        consider the polygon for the analysis
    end if
end for
```

Furthermore, in the next sections we will compare systems with different aspect ratios. In Table 4.4 we list each aspect ratio investigated, together with the respectives small and big particle diameters. Note that there are two systems with $a = 0.75$. We will explore this further in Section 4.3.4.

Table 4.4 Aspect ratios investigated in our work, together with the respectives small and big particle diameters. We note that there are two systems with $a = 0.75$.

Aspect ratio	Big particle diameter (mm)	Small particle diameter (mm)
0.5	5	2.5
0.6	5	3
0.75	5	3.75
0.75	8	6

4.3 Results from the simulations

4.3.1 Dynamics of the compression

Fig. 4.5 shows the effect of the size ratio of the particles in the compression of the bed of particles. Note that in all cases, R is kept constant at 0.5, indicating that half of the particles are of each species. We plot, together with the particles, their Voronoi regions (that is, the Voronoi tessellation of the system).

During the compression, the Voronoi cells change shape due to the rearrangement of the particles, which is a consequence of the reduction of the space available for them. The systems are compressed until the packing fraction reaches $\phi = 0.34$. We note that the final strokes of the piston are different, as they are related to the geometry of the system via Eq. (4.23). Namely, the smaller the aspect ratio, the lower the final stroke. Conversely, when the particles are roughly the same size, as in the case of $a = 0.75$, we note a larger number of dark green cells in the domain, indicating a larger presence of more regular hexagons. This is an indication of a more ordered structure in this case than in the other cases, where the particle size difference is more pronounced.

The force acting on the piston during the compression is shown in Fig.4.7. We observe that all curves follow the same trend in terms of dimensionless force, regardless of the particular values of

a and R of the system, indicating a scalable macroscopic behaviour of the system in terms of the variables tested here. The inset of Fig.4.7 also shows that the dimensional force on the piston at the final compression state increases with R. This is due to the fact that the stroke of the piston increases as the amount of small particles increases in the system. Furthermore, it is also observed that the dimensional force on the piston at the final compression state increases as a decreases, as the systems with the smaller particles need to be compressed further down to maintain the packing fraction constant, as mentioned in the first paragraph of the section, therefore getting closer to the piston and exerting larger forces. This is confirmed with Fig. 4.6, which plots, for each aspect ratio with $R = 0.5$, the minimum distance to the piston attained by a particle of the system from half of the compression onwards, which we denote by

$$\delta_a^t, \quad 0.5 \leqslant t \leqslant 1. \tag{4.29}$$

We observe a more pronounced separation at the end of the compression, and we note that in all these three systems the minimum distance at the maximum compressed state was attained by a small particle. For completeness, the values of δ_a^1 were, in (big) particle diameters:

$$\delta_{0.75}^1 = 0.96, \tag{4.30}$$

$$\delta_{0.6}^1 = 0.88(\downarrow 7.63\% \text{ from } \delta_{0.75}^1), \tag{4.31}$$

$$\delta_{0.5}^1 = 0.81(\downarrow 8.64\% \text{ from } \delta_{0.6}^1 \text{ and } \downarrow 15.61\% \text{ from } \delta_{0.75}^1). \tag{4.32}$$

Figure 4.8 shows the dependence of the maximum force on the piston at the end of the compression as a function of R, $F_{\max}^R$ normalized by the largest value $F_{\max}^{R=1}$ that $F_{\max}^R$ can achieve for each aspect ratio, which happens when $R = 1$. The lines are bi-exponential fits of the form $A\exp(\lambda_1 x) + B\exp(\lambda_2 x)$, and the parameters for each value of a are summarized in Table 4.5. One sees that this fit captures well the behaviour of the data, but the coefficients of the $a = 0.75$ system are notably different from the other two systems. We believe that this is due to the fact that, since this system has an aspect ratio close to 1, the maximum force on the piston does not vary as much from $R = 0$ to $R = 1$, hence the bi-exponential behaviour is less pronounced. To be precise, our analysis was conducted for a fixed packing fraction through all aspect ratios and mixing ratios. Therefore, the higher the aspect ratio is the greater the height at which the piston will be at the end of the compression for $R = 1$, causing the system with greater aspect ratio to have a smaller variation in the final compression height between $R = 0$ and $R = 1$ and, consequently, a smaller variation on the force felt by the piston between $R = 0$ and $R = 1$.

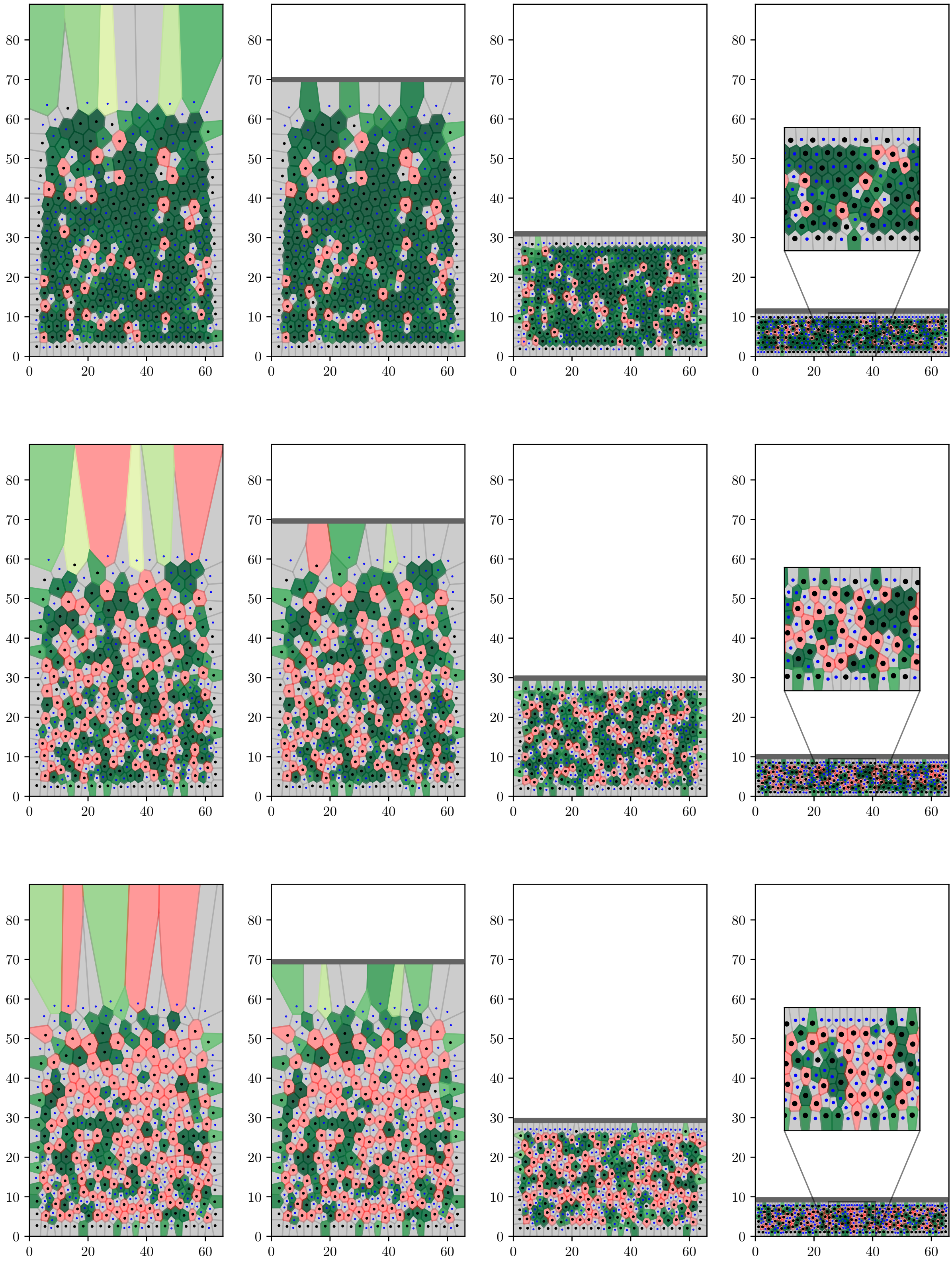

Figure 4.5 Snapshots of the compression of the system for $R = 0.5$ and for different values of a. From top to bottom, $a = 0.75, 0.6, 0.5$. The colors of the regions denote the different shapes of the polygons obtained by the Voronoi tesselation. See text for notation. The insets on the right columns show a zoom of the arrangement of the particles in the final compressed state. Small particles are colored blue and big particles are colored black

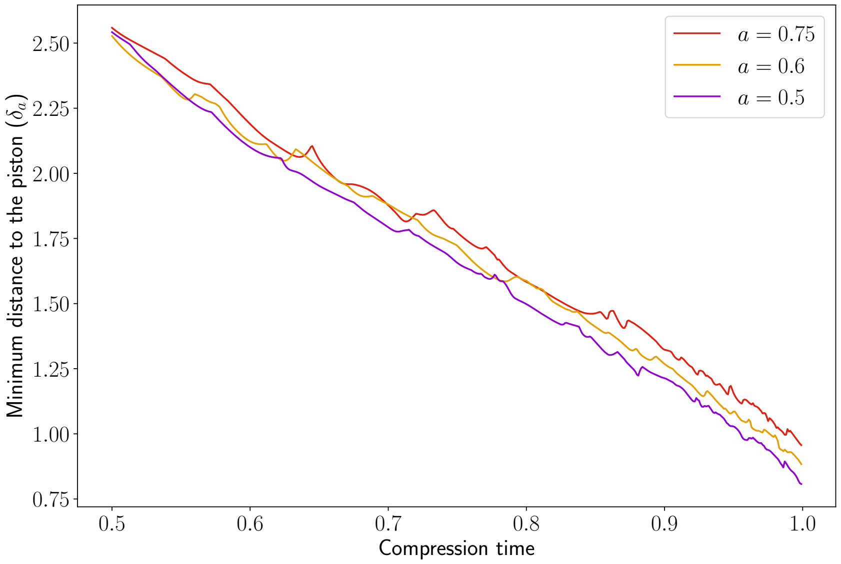

Figure 4.6 Minimum distance to the piston (δ_a) for each aspect ratio with $R = 0.5$ from half of the compression time onwards. We see a separation between the curves, with smaller aspect ratios having closer distances to the piston at the compressed state. As pointed in the text, these distances were achieved by small particles in all three systems.

This smaller variation also explains the inversion of the colored curves from the inset of Fig. 4.7 to Fig. 4.8. Since Fig. 4.8 shows the piston forces normalized by the maximum force (at $R = 1$) for that system and since smaller aspect ratios present greater variation on the piston force from $R = 0$ to $R = 1$, the order of curves is inverted from one plot to the other.

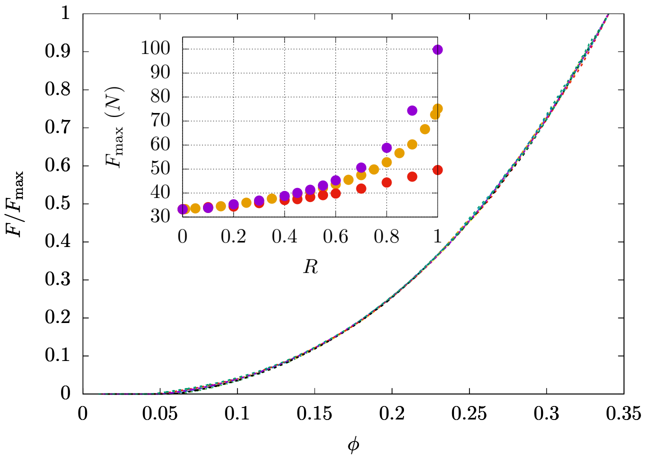

Figure 4.7 Normalized piston force as a function of the the packing fraction during the compression for the systems with different a and R. The inset shows the maximum dimensional force $F_{\max}$ obtained at the maximum stroke as a function of R for $a = 0.5$ (purple), $a = 0.6$ (orange) and $a = 0.75$ (red). Each of the simulations was run at least twice and the plots shown represent the average. The maximum difference observed on the value of $F_{\max}$ between simulations for the same parameters was 0.2N.

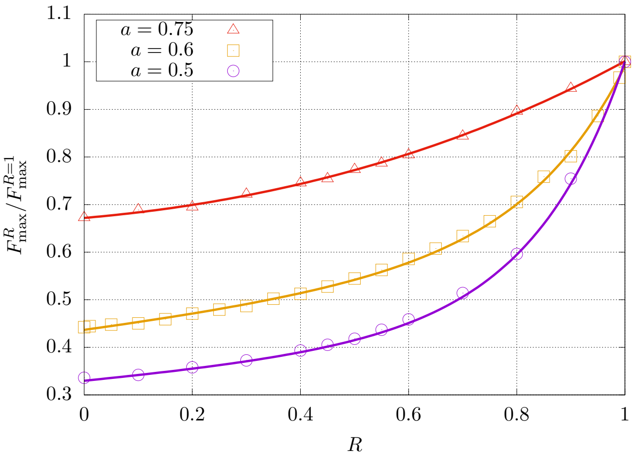

Figure 4.8 Normalized force on the piston at the compressed state for the different aspect ratios. The lines correspond to bi-exponential fits of the form $A\exp(\lambda_1 x) + B\exp(\lambda_2 x)$, as proposed in [15].

Table 4.5 Parameters of the bi-exponential fit $A\exp(\lambda_1 x) + B\exp(\lambda_2 x)$ for the different aspect ratios.

System	$a = 0.75$	$a = 0.6$	$a = 0.5$	$a = 0.75$ $(6:8)$
A	0.351254	0.435046	0.328226	0.654726
λ_1	-0.556311	0.343908	0.322588	0.18066
B	0.320667	0.00168275	0.00157644	0.0190259
λ_2	0.914147	5.41306	5.84935	2.42801

We note that the bi-exponential fits were carried out using Gnuplot [40] and that the two systems with $a = 0.75$ had the greatest relative errors. Despite this, we still have a good fit of the curve to the data points (where the curve and data for the aspect ratio $6:8$ was omitted to avoid cluttering of the plot). Once again, we believe this behaviour is due to the "flattening" of the bi-exponential curve related to the smaller variation in the piston force between $R = 0$ and $R = 1$ for systems with greater aspect ratios, as discussed in the previous paragraph.

A brief commentary on the nature of the aspect ratio as a parameter. As a last commentary on this section, we would like to note that the aspect ratio a, as a parameter, is not universal, that is, it depends on the specific values of the diameters of the big and small particles. However, the overall behaviour of systems with the same aspect ratio but with different particle sizes remain the same. We will discuss this further in Section 4.3.4.

4.3.2 Changes in the arrangements of the particles during compression

Figure 4.9 shows the evolution of the proportion of hexagons during the compression of the system for each of the aspect ratios shown in Fig. 4.5, and for the same $R = 0.5$, as well as the proportion of hexagons during the compression for a monodisperse system that corresponds to $R = 0$ in the $a = 0.6$ aspect ratio system. The early stages of the compression do not seem to affect much the value of n_6, but as the system becomes more and more compressed, important fluctuations are observed, indicating the continuous, yet abrupt, changes of the regions as the particles change their arrangement in the system. Note, however, that there is a higher proportion of hexagons for larger value of a, indicating that, as the particles are of more similar sizes, the system becomes more ordered.

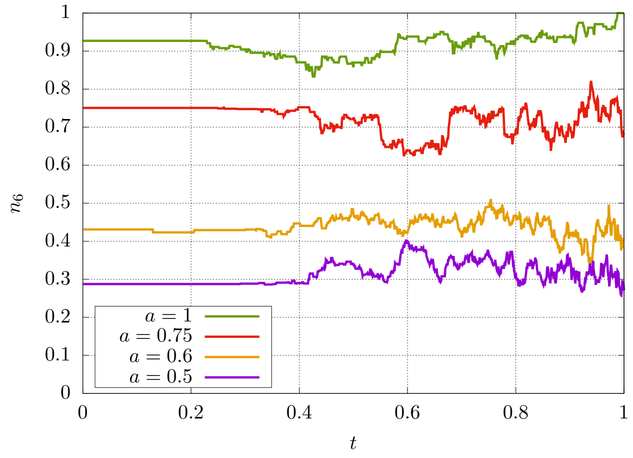

Figure 4.9 The proportion of hexagons (n_6) during the compression of the particles, plotted for the different aspect ratios and $R = 0.5$. The simulations shown here are the same presented in Fig. 4.5.

To better qualify this behaviour, we present Fig. 4.10. It shows the average of $\mathcal{R}_{\hexagon}$, given in Eq. (4.25), the hexagon regularity metric, for each of the three aspect ratios studied (in solid lines), together with the variations of one standard deviation from the average (in dotted lines) during the compression. In green, we also plot these curves for the standard aspect ratio system with only big particles, to represent a monodisperse system, that is, a system with $a = 1$. We see that the higher the aspect ratio is, the more regular the hexagons are, on average, with similar fluctuations ocurring during compression as in Fig. 4.9. We also note that the average hexagon regularity at the end of the compression is slightly lower than at the beggining, as Table 4.6 details.

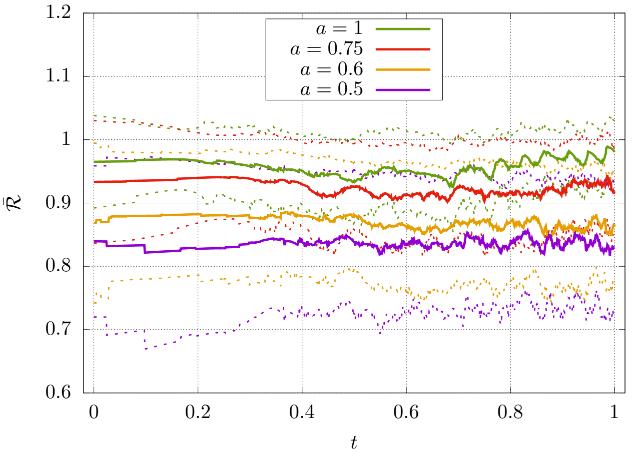

Figure 4.10 Average (solid lines) and standard deviation (dashed lines) of the hexagon regularity ($\mathcal{R}_{\hexagon}$) for each of the aspect ratios. The $a = 1$ curve consists of the standard aspect ratio system with $R = 0$, that is, only big particles.

Table 4.6 Average and standard deviation of the hexagon regularity ($\mathcal{R}$) at the beggining ($t = 0$) and end ($t = 1$) of the simulation for each of the aspect ratios.

	$a = 1$		$a = 0.75$		$a = 0.6$		$a = 0.5$	
Time	$\bar{\mathcal{R}}$	$\sigma(\mathcal{R})$	$\bar{\mathcal{R}}$	$\sigma(\mathcal{R})$	$\bar{\mathcal{R}}$	$\sigma(\mathcal{R})$	$\bar{\mathcal{R}}$	$\sigma(\mathcal{R})$
$t = 0$	0.96	0.07	0.93	0.10	0.87	0.13	0.84	0.12
$t = 1$	0.98	0.05	0.92	0.07	0.87	0.09	0.83	0.10

Figure 4.11 show the dependence of the proportions n_5, n_6 and n_7 on R for the three systems with different aspect ratios, respectively. Firstly, one observes that the $a = 0.6$ curves follow very similar trends to the ones observed in the experiments[16], indicating that the numerical approach also captures very well the essence of the structure of the system, in addition to its dynamics. Note that, in the simulations, almost identical results were obtained for the values $R = 0$ and $R = 1$, so that the curves for all the proportions are almost symmetrical with respect to $R = 0.5$. This was not the case in the experiments, however, and we argue that this was due to the fact that the small size particles in the experiments had relatively greater individual variation in the magnitude of the magnetic dipole moment and that they perturbed the force measurements, and therefore the packing arrangements, for R in the vicinity of 1. Another possible reason for this discrepancy between experiments and simulations is the fact that the approaches are different: in the experiments, the granular bed is compressed until a given force (namely, 110N) is obtained; in the simulations, the granular bed is compressed until a given height is reached. We believe that compressing to such a high force introduces a small but not negligible amount of contact between the particles, perturbing the order that should, in a contactless system, be attained.

Figure 4.11 shows that the larger the aspect ratio, the larger the value of n_6, indicating, as discussed above, that the system becomes more ordered. Furthermore, for $a = 0.75$, we observe that the variation of n_6 induced by changes in R is much smaller than for the other two cases. This behaviour is due to the fact that in such systems the big and small particles have more similar dimensions, so that it becomes harder for a small particle to "infiltrate" in the midst of big particles and disrupt the organization. This can also be explained by the same argument related to the particle sizes: the more similar the values of the diameter of the particles are, the less perturbed the system will be by bi-dispersity. Finally, we also note that the maximum values of n_5 and n_7 are obtained near the region of $R = 0.5$, indicating that most disordered states are obtained for $50\% - 50\%$ mixtures of small-big particles regardless of their aspect ratio. This is in agreement with our experimental findings [16].

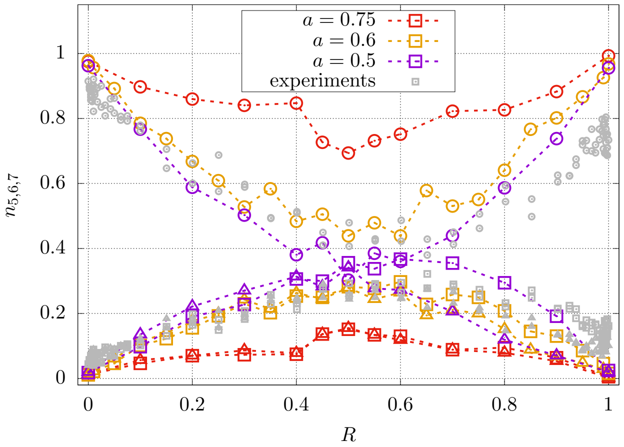

Figure 4.11 Distribution of the proportion of pentagons (n_5, squares), hexagons (n_6, circles) and heptagons (n_7, upwards triangles) at the compressed state for different mixing ratios. The light-grey symbols with the same notations represent the experimental data presented in [16].

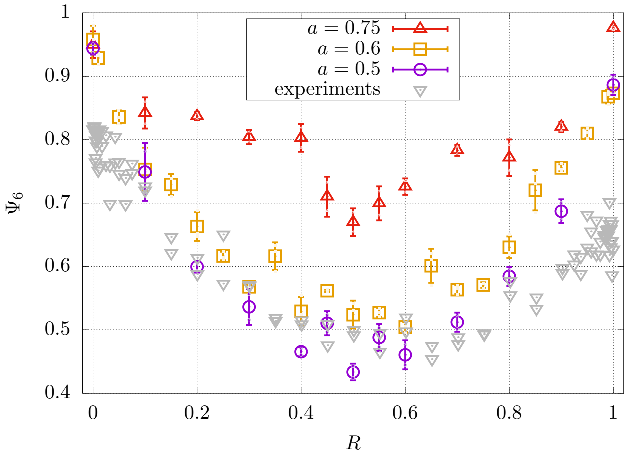

Figure 4.12 Behaviour of Ψ_6 against the mixing ratios. For the systems with more than one run, we plot the mean with the error bars of standard deviations.

Figure 4.12 shows the comparison of Ψ_6 between the different aspect ratios simulated and the experiments conducted in previous work [16]. Figure 4.13 exhibits the linear correlations between Ψ_6 and n_6 for the different aspect ratios, confirming once again [16] the good correlations between these two parameters. The lines in the plot are the best fit lines and the (Pearson's) correlation coefficients obtained were 0.988, 0.986 and 0.982 for the aspect ratios 0.6 and 0.5 and 0.75, respectively.

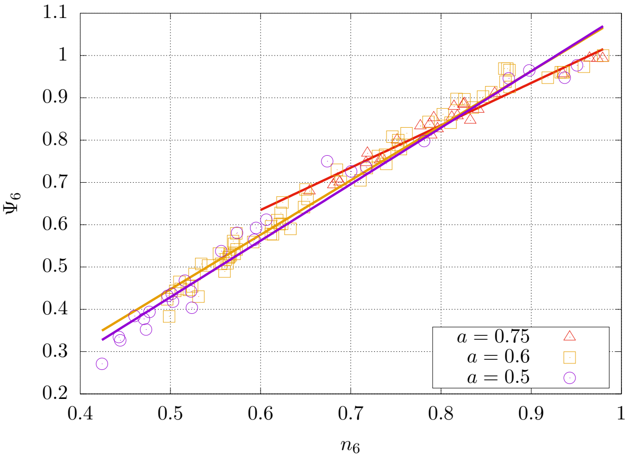

Figure 4.13 Correlation between our two order parameters for systems with different aspect ratios. One sees that all four scenarios are quite similar from the distribution of points and also from the best fit lines, plotted in the corresponding colors. The (Pearson's) correlation coefficients obtained were 0.988, 0.986 and 0.982 for the $a = 0.6$, 0.5 and 0.75 systems, respectively.

4.3.3 Introducing viscous friction and removing gravity

In this section we explore simulations with viscous friction and/without gravity for the default aspect ratio $a = 0.6$. The introduction of a viscous friction and the removal of gravity aim to mimic the compression of the bed with an interstitial fluid with neutrally buoyant particles, respectively. To be precise, three other scenarios were considered, besides from the standard system with dry friction and gravity:

- a system with both dry and viscous friction and gravity during the compression, hereafter referred to as “dry + vis” system;
- a system with only dry friction and no gravity during the compression, hereafter referred to as “dry + no grav” system;
- a system with both dry and viscous friction and no gravity during the compression, hereafter referred to as “dry + vis + no grav” system.

As a first overview of how these systems compare to each other, we present Fig. 4.14. It shows the behaviour of the 4 different systems throughout the compression for $R = 0.5$. From top to bottom we have: the standard system, with dry friction and gravity; the system with dry and viscous friction and gravity; the system with only dry friction and no gravity; and the system with dry and viscous friction and no gravity. We see that, apart from the wildly different initial arrangement when the compression starts, the gravity and no gravity systems differ only on the distance that the particles get to the piston at the beggining of the compression and on the random arrangement at the end of the compression.

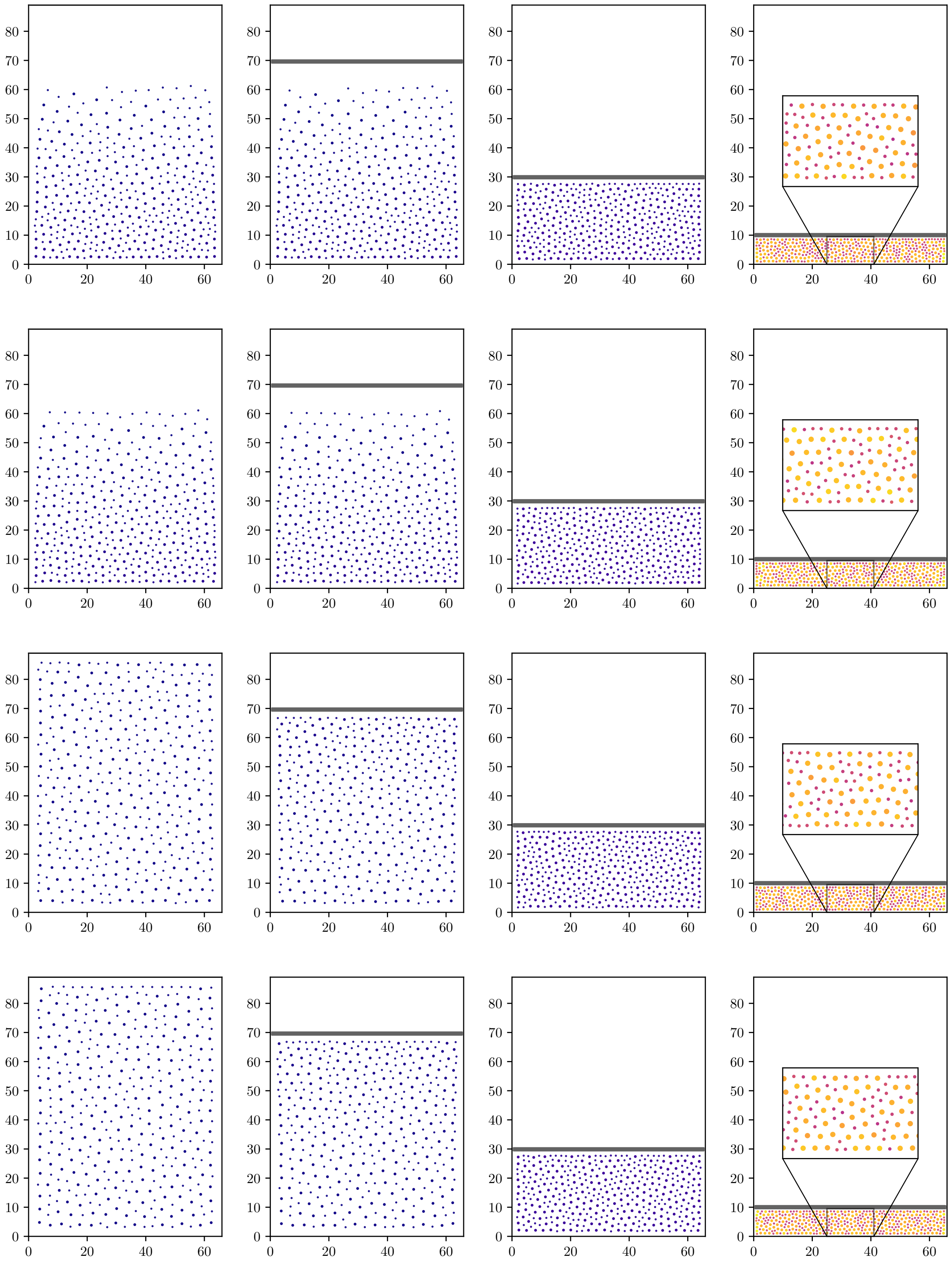

Figure 4.14 Compression snapshots for the standard system, with dry friction and gravity (first row); the system with dry and viscous friction and gravity (second row); the system with only dry friction and no gravity (third row); and the system with dry and viscous friction and no gravity (last row).

This indicates that there is no significant difference in behaviour when we remove gravity. This is further confirmed by Fig. 4.15 and Fig. 4.16, which present the behaviour of the normalized force at compression for several values of R and the Voronoi regions distributions for several values of R, respectively. To be precise, the removal of gravity removes the stratification on the system, as the different initial conditions show. This stratification does not play a role on the final compressed state, since the layer of particles is too thin for the stratification to have any effect. Furthermore, removing stratification with an intersticial fluid would imply in an important fluid drag and, therefore, the need for a viscous drag force in the model.

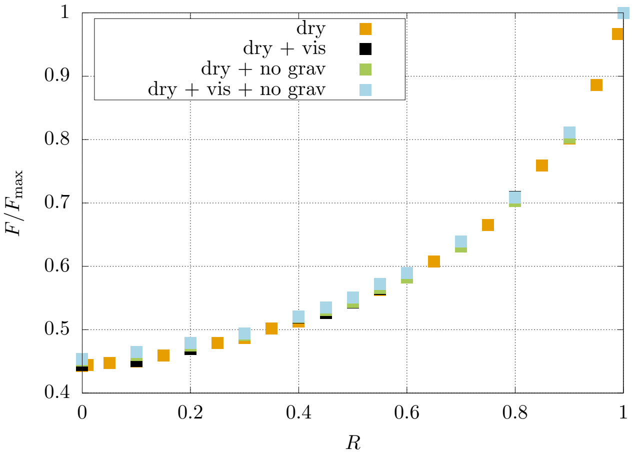

Figure 4.15 Normalized piston force at maximum compression for systems with one/both frictions models and with/without gravity throughout the different values of mixing ratios.

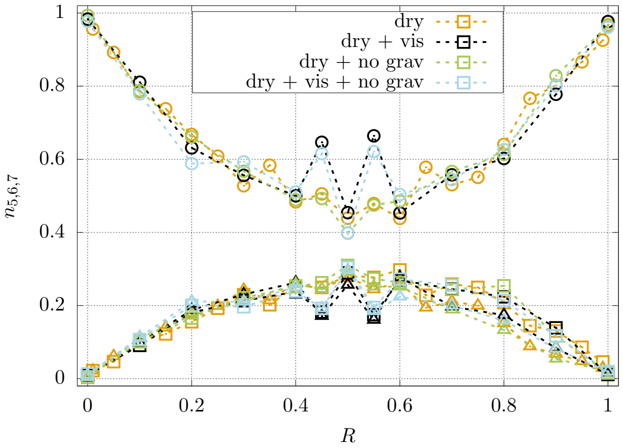

Figure 4.16 Distribution of the proportion of pentagons (n_5, squares), hexagons (n_6, circles) and heptagons (n_7, upwards triangles) at the compressed state for different mixing ratios. Both plots show that all four systems have similar behaviours with respect to the order parameters.

The viscous friction coefficient adopted was $\gamma = 0.1$, in order to introduce just a small perturbation on the standard system. It is important to note that reproducing any of these three scenarios experimentally is really challenging (and, to the best of our knowledge, has not been done yet), since one would have to, for example, allow the interstitial fluid to exit the system in the exact rate as to keep the particles neutrally buoyant.

Figure 4.16 show the dependence of $n_{5,6,7}$ on R for the dry system and the viscous/no gravity systems. One sees that, for the most part, the systems with viscous friction and/or no gravity do not differ much from the standard system. We noted, for the viscous systems for $R = 0.45$ and 0.55, important fluctuations on the values pf $n_{5,6,7}$. Since only one run was executed for the viscous/no gravity systems, we can not say for sure if that is an innate behaviour of the system or, most likely, simply a statistical variation. One can thus see that introducing a viscous friction and disconsidering the effects of gravity during the compression does not change the fact that the maximum disorder is still achieved at $R \approx 0.5$. Essentially, gravity becomes practically irrelevant at the end stages of the compression. We note that the Pearson's correlation coefficient between n_6 and Ψ_6 calculated for these systems were all greater than 0.97.

4.3.4 Is the aspect ratio sufficient to characterize the system?

In this section we would like to show that the aspect ratio a, as a parameter, is sufficient to characterize the system, that is, systems with the same a but different values of the diameters of the big and small particles have the same behaviour. Here we will explore the differences between two systems with $a = 0.75$, one with big particles having diammeter of 5mm and another with big particles having diameter of 8mm.

In Fig. 4.17, we show the behaviour of the normalized force at maximum compression for the two systems with $a = 0.75$. We see that, despite the few occasional differences, the two curves are very similar, pointing to the fact that the systems are very alike.

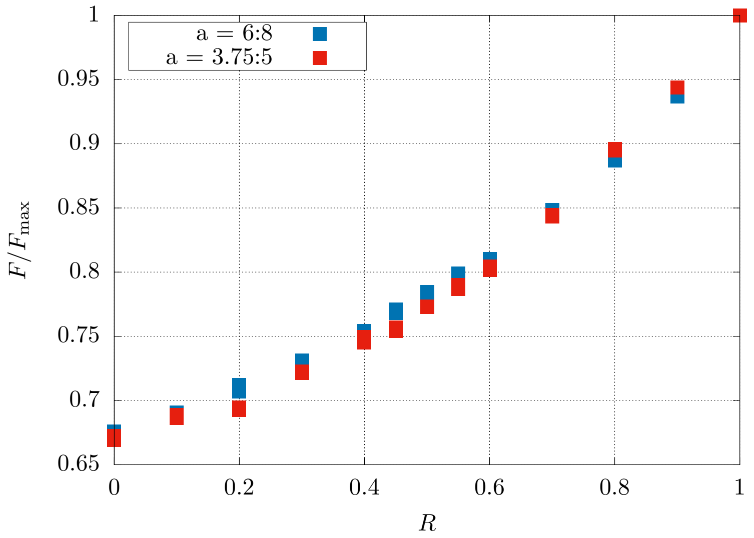

Figure 4.17 Normalized piston force at maximum compression for the two systems with aspect ratio 0.75 throughout the different values of mixing ratios. We see that there are few differences in the behaviour.

In Figure 4.18 we show the evolution of $n_{5,6,7}$ with the mixing ratio R for the two systems with $a = 0.75$. Note that the general behaviour is preserved, which suggests that the aspect ratio is the most relevant parameter instead of the particle's diameter.

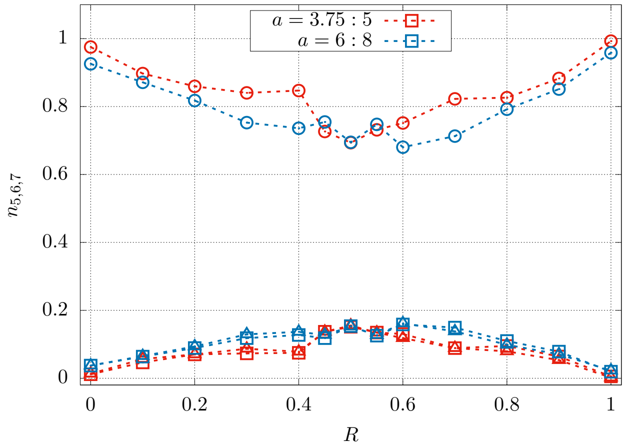

Figure 4.18 Distributions of $n_{5,6,7}$ vs the mixing ratio for both systems with aspect ratio 0.75. One sees that both systems behave very similarly, with n_6 attaining the minimum in the range $0.5 \lesssim R \lesssim 0.6$.

We also note that the Pearson's correlation coefficient between n_6 and Ψ_6 calculated for these systems were both greater than 0.97.

4.3.5 Force chains

Force chains in granular materials are networks of particles that carry the majority of the mechanical load through the system. These chains form along paths where contact forces between particles are significantly higher than average, creating a heterogeneous stress distribution. Rather than being evenly spread, the forces in granular assemblies tend to concentrate along these chain-like structures, which can span across the material and play a key role in its overall mechanical behavior, such as stability, flow, and jamming. Fig. 4.19 exhibits two such examples: on the left we show the force chains in a numerical simulation of a granular material, and on the right we show the force chains on a real granular material, visualized through birefringence.

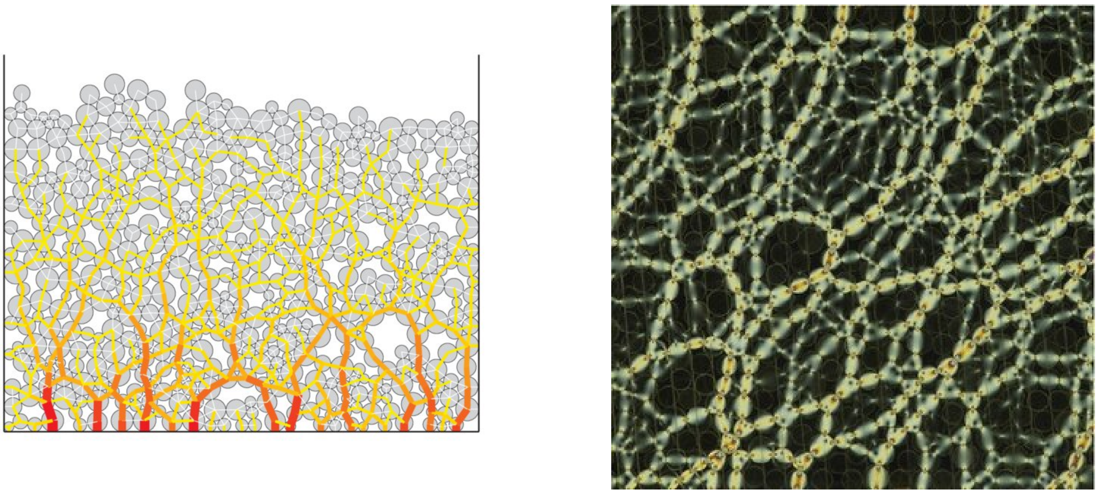

Figure 4.19 Force chains examples: a numerical simulation result on the left (extracted from [41]), and a fabric of force chains ocurring in a real granular material (extracted from [42]).

We attempted to define force chains in our system, but with only partial success. Figure 4.20 exhibits a snapshot of the standard system for $R = 0, 0.10, 0.5$ and 0.90 at maximum compression. The color gradient follows the intensity of the force on the particle: the lighter the color, the greater the force. Despite the fairly homogeneous color distribution, it can be seen that the small particles experience forces of smaller amplitude than the big particles.

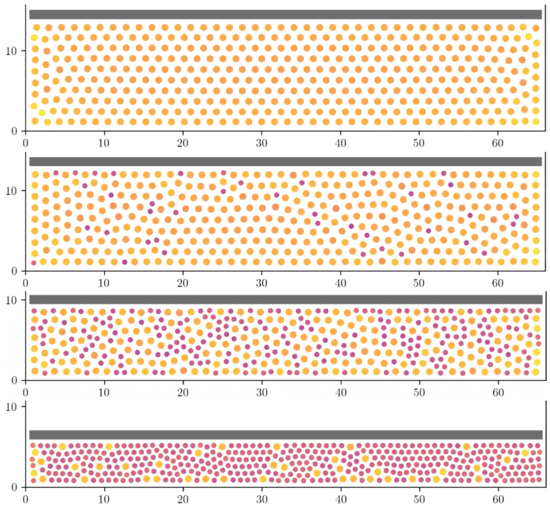

Figure 4.20 Final compressed state in the standard system ($a = 0.6$) for $R = 0, 0.10, 0.50$ and 0.90 (top to bottom). The coloring follows the intensity of the force on the particle: the lighter the color, the greater the force. One observes that the small particles, compared to the big particles, experience forces of smaller magnitude.

In an attempt to quantify this qualitative difference, we performed a statistical analysis on the force distribution. Namely, we looked at the histogram and probability density function of the normalized force on the particles, comparing different values of R for the $a = 0.6$ system, as shown in Figure 4.21. We also compared the same value of R, namely 0.5, across the different aspect ratios, as shown in Figure 4.22. One can observe that the force distributions are bi-modal and that an almost perfect 50 — 50 split is observed in the PDF's of Figure 4.22. This is in agreement with the homogeneous color distribution among the particles. The number of bins/bin-width were computed using Knuth's rule[2] presented in [44].

---

[2] Knuth's rule is a fixed-width, Bayesian approach to determining the optimal bin width of a histogram. The rule says that the optimal number of bins is the value M which maximizes the function

$$F(M|x, I) = n\log(M) + \log\Gamma\left(\frac{M}{2}\right) - M\log\Gamma\left(\frac{1}{2}\right) - \log\Gamma\left(n + \frac{M}{2}\right) + \sum_{k=1}^{M}\log\Gamma\left(n_k + \frac{1}{2}\right), \tag{4.33}$$

where I represents the prior knowledge about the problem, which includes the range of the data and the bin alignment, Γ is the gamma function,

$$\Gamma(z) = \int_0^\infty t^{z-1}e^{-t}\,\mathrm{d}t,\ \mathrm{Re}(z) > 0, \tag{4.34}$$

n is the number of data points and n_k is the number of measurements in bin k. We chose this rule for computing bin-width for two main reasons: first, it is a straightforward data-based method of determining the optimal number of bins in a uniform bin-width histogram; second, it is already implemented in the well established Python library Astropy, produced by [43].

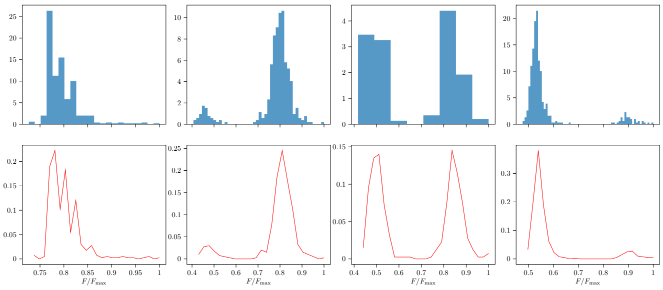

Figure 4.21 Histograms (top) and probability density functions (bottom) of the normalized force on the particles for $R = 0, 0.10, 0.50, 0.90$ (left to right) in the $a = 0.6$ system. The number of bins/bin-width was calculated using Knuth's rule presented in [44].

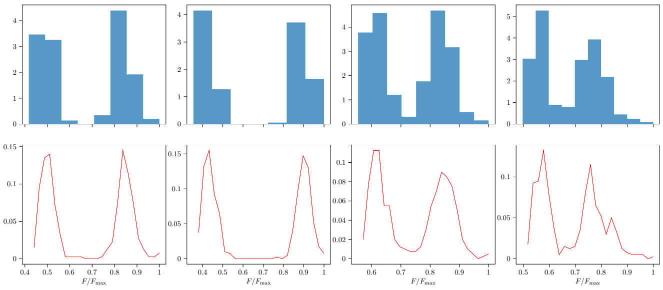

Figure 4.22 Histograms (top) and probability density functions (bottom) of the normalized force on the particles for $a = 0.6, 0.5, 0.75(3.75 : 5), 0.75(6 : 8)$ (left to right) with $R = 0.5$. The number of bins/bin-width was calculated using Knuth's rule presented in [44].

The prevalence of two values of forces is a hint that, in this system, we shall not observe the presence of force chains as in usual granular materials [45]. Note that since the particles are randomly distributed in the bed, which is clearly seen for $R = 0.5$ in Fig. 4.20, and the fact that in our system the particles are contactless and the forces are field-long-range forces, there are no preferred channels for the force chains to form.

To further illustrate this we show Figs. 4.23 and Fig. 4.24. In Fig. 4.23 we exhibit the resulting magnetic forces (particle-particle and wall-particle) acting on each particle inside the box considered for the Voronoi tesselation (which is why the more “outer” particles do not have arrows drawn on them), normalized by absolute value of the greatest force for each particle species throughout the compression. From top to bottom are the standard systems ($a = 0.6$ and only dry friction) for $R = 0.25, 0.50$ and 0.75. We see that there is no preferred direction that the vectors tend to point to, hinting to the absence of force chains.

In Fig. 4.24 we show the compression of the same systems mentioned above, where the colormaps represents the quantity

$$\frac{|F_i^k - \bar{F}_i|}{\bar{F}_i}, \tag{4.35}$$

where F_i^k indicates the absolute value of the resulting magnetic forces acting on particle k, which is of type i (big or small) and $\bar{F}_i$ indicates the average intensity of the resulting magnetic forces acting on the particles of type i. In essence, we are showing fluctuations from the average and we see that there is no pattern on the color distribution, which indicates, once again, the absence of force chains in this system. As a last comment, we note that the particles considered in each snapshot are, as in the previous figure, the ones contained in the box considered for the Voronoi tesselation. Particles outside this box where attributed 0 fluctuation.

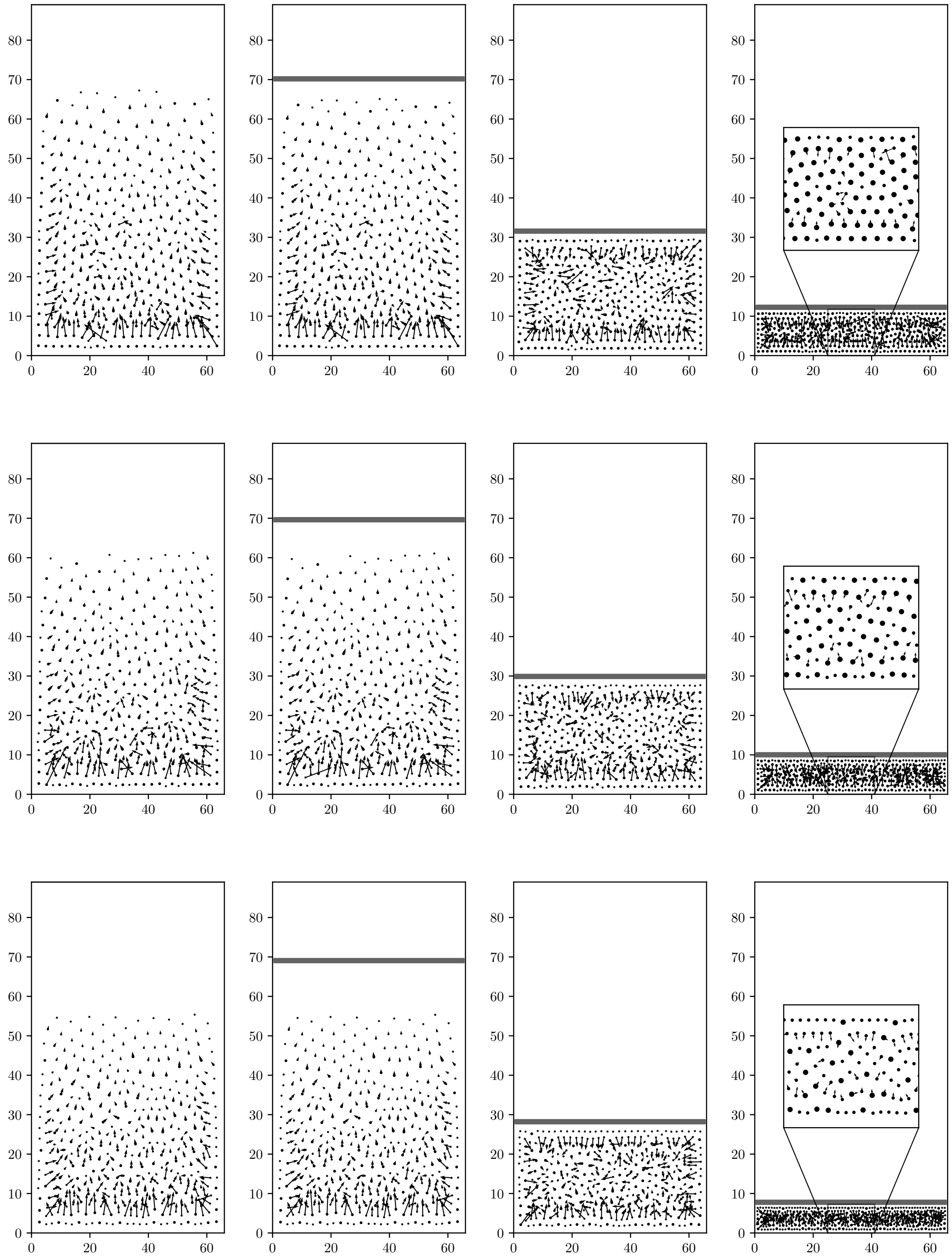

Figure 4.23 Resulting magnetic forces (particle-particle and wall-particle) acting on each particle, normalized by absolute value of the greatest force for each particle species throughout the compression. From top to bottom are the standard systems with $R = 0.25$, 0.50 and 0.75. We see that there is no preferred direction to which the vectors point to, indicating the absence of a force chain in the system.

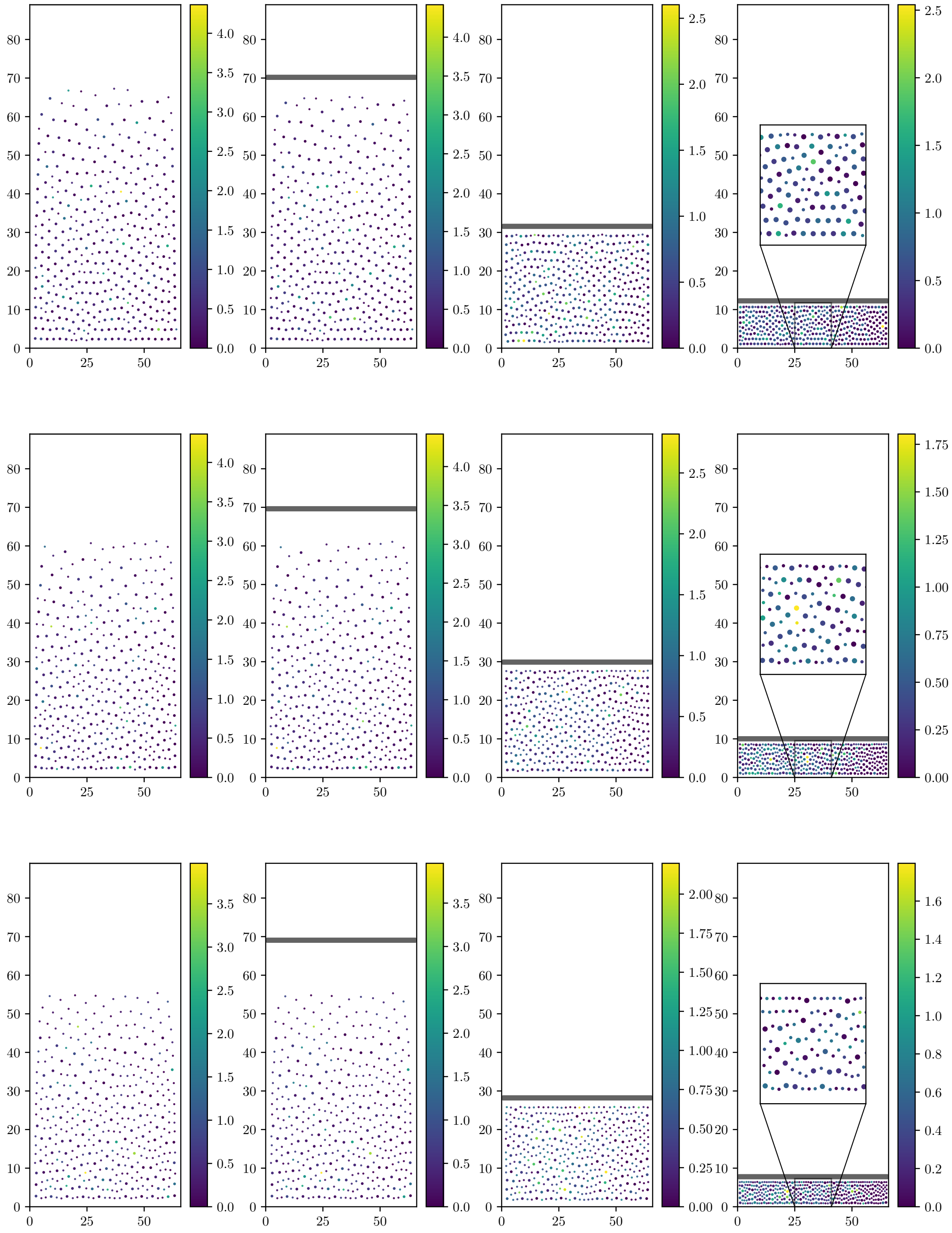

Figure 4.24 Fluctuations from the average resulting magnetic forces acting on each particle (see Eq. (4.35)). From top to bottom are the standard systems with $R = 0.25, 0.50$ and 0.75. We see that there is no pattern on the coloring of the particles, indicating, once again, the absence of a force chain in the system.

Part III

Large systems and an application

CHAPTER 5

HIGH EFFICIENCY COMPUTATION OF NEIGHBOURS FOR LARGE SYSTEMS

> "The price of metaphor is eternal vigilance."
>
> — Norbert Wiener.

5.1 The Verlet list algorithm

In order to escalate the size of the system, i.e., simulate with more particles, an optimization was needed to improve the performance of the code. Up until now, the results presented were obtained from simulations using a naïve $O(n^2)$ algorithm, where for each particle every other particle was taken into account to compute the inter-particle force. This results in a theoretically "complete" simulation in the physical sense, but a very slow one: for the standard system with 368 particles, the simulation takes ≈ 18 hours to run. For the system to be scaled towards thousands (or even tens of thousands) of particles, there was no way around but to numerically optimize the code.

To accomplish this goal, the Verlet list algorithm was used [46, 47, 48, 49]. This algorithm is frequently used in molecular dynamics simulations, where the potential decays very rapidly and there is no need to compute every interaction to accurately simulate the system as a whole. In a simulation that uses this algorithm, one constructs a list of all the neighbours of each particle at the first step of the simulation. Then, during a fixed number of steps or until a given threshold is reached, all interactions for each particle are computed considering only its respective neighbours: to compute the forces acting on particle *i* one need only look to its neighbours list and, for each neighbours in that list, check if it is at a given distance to *i*; if it is, then this particle's effect on *i* is considered; if it is not, then this particle is not considered. On the other hand, one of the possible downsides of using Verlet lists, if the algorithm is not used carefully, is simplifying the interactions too much and affecting the results, essentially making the system non-physical.

That is the "standard" way of using the algorithm. As explained, this original, and most used variation of the algorithm makes use of three parameters: r_v, the Verlet list radius, which determines the particles that *can* be considered when computing the forces;

$$r_c < r_v, \tag{5.1}$$

the cut-off radius, which determines the particles that *will* be considered when computing the forces; and

$$r_s = r_v - r_c, \tag{5.2}$$

the skin, which determines the frequency at which the Verlet lists will be updated throughout the simulation.

In fact, let $\widehat{d_p}$ be the average particle displacement per simulation step. One must have $\widehat{d_p} < r_s$, that is, the skin must be greater than the distance that a particle travels in one simulation step. Furthermore, the average amount of simulation steps necessary until the Verlet lists are rebuilt is

$$r_s/\widehat{d_p} = s_r, \tag{5.3}$$

so that throughout a simulation with N_T steps, the Verlet lists will be rebuilt (on average) a total of $N_T/s_r = N_T \cdot \widehat{d_p}/r_s$ times. With this formulation it is easy to see that the greater r_s is, the less we need to update the lists, which tends to improve the speed of the algorithm. On the other hand, greater r_s means greater r_v and r_c, i.e., more particles will be considered when computing forces, which tends to decrease the speed of the algorithm. To use Verlet lists efficiently, a fine balance between these two opposing sides must be found.

In this work, we did not use the Verlet list algorithm in the "standard" way. Figure 5.1 illustrates the Verlet list parameters: in the left we show the "standard" algorithm, and in the right we illustrate how we are using it in this work, as will be explained shortly in the following.

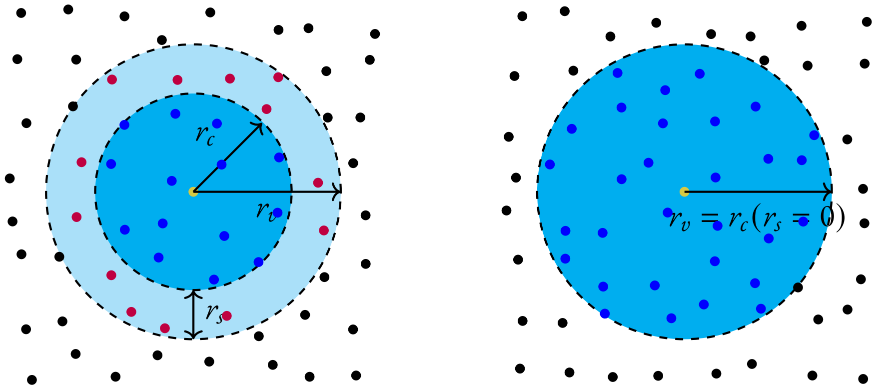

Figure 5.1 Illustration of the Verlet list algorithm. The blue particles are inside the cut-off radius of the yellow particle, the purple particles are outside the cut-off radius but inside the Verlet radius of the yellow particle and the black particles are outside the Verlet radius of the yellow particle. In the left we illustrate the "standard" algorithm, and in the right we illustrate how we are using it in this work.

We note that this optimization is only applied for computing the inter-particle forces. Therefore, the interactions of each particle with every wall are computed at each time step. This is justified since the forcing that one inputs into the "material" (i.e., the particles) has to be felt by all the particles. It is more the complexity with which particles interact with one another, on a distance basis, that can be numerically "simplified" with the Verlet list algorithm.

In Algorithm 5.1 we exhibit a pseudo-code implementation of this algorithm. In the work presented here,

$$r_c = r_v \iff r_s = 0, \tag{5.4}$$

that is, there was no skin in the physical sense: for each particle i, all particles j in i's Verlet list were considered when computing the inter-particle force on i. This choice is justified due to the fact that the system being analysed is magnetic: the interactions are all at a distance with inter-particle force decaying proportionally to d^{-4}. Therefore, it is reasonable to consider "neighbouring" particles to compute interactions without distinguishing between these neighbours. In practical terms, this means that the we implemented the pseudo-code in Algorithm 5.1 without the condition in lines 20–22.

Furthermore, the parameter r_s, despite not existing physically in this application, was still necessary as a numerical parameter and fixed at $4.13D$. This choice is arbitrary but nonetheless justified: the average particle displacement every 10^3 simulation steps throughout the complete simulation (initial relaxation, compression, expansion, final relaxation) is on the order of $2 \cdot 10^{-2}D \ll 4.13D$. Also, the number of $4.13D$ has a meaning: it is the exact distance at which the magnetic force of a particle equals the weight of a particle. In fact, consider the force between two particles as given in Eq. (2.7), where μ is the magnetic dipole moment of the magnets (here assumed identical), r is the distance separating the center of the magnets and μ_0 is the magnetic permeability of the vacuum. Writing $\mu = \mathrm{Br} \cdot V_p/\mu_0$, where Br is the residual magnetization of the material and $V_p = \pi\varepsilon D^2/4$ is the volume of a particle, with ε being the width of the particles, one can find the distance beyond which the inter-particle force is less than a given fraction α of the weight W_p of a particle. Since $W_p = \rho g V_p$, one must have

$$\begin{aligned}
F \leqslant \alpha W_p &\iff \frac{3\mu_0\mu^2}{4\pi} \cdot \frac{1}{\rho g V_p} \cdot \frac{1}{r^4} \leqslant \alpha \\
&\iff \frac{3\mu_0}{4\pi} \cdot \frac{\mathrm{Br}^2 V_p^2}{\mu_0^2} \cdot \frac{1}{\rho g V_p} \cdot \frac{1}{\alpha} \leqslant r^4 \\
&\iff \frac{3\mathrm{Br}^2 V_p}{4\pi\mu_0\rho g} \cdot \frac{1}{\alpha} \leqslant r^4 \\
&\iff \frac{1}{\alpha} \cdot \frac{3\mathrm{Br}^2 D^2\varepsilon}{16\mu_0\rho g} \leqslant r^4 \\
&\iff r \geqslant \frac{\sqrt[4]{3}}{2} \cdot \sqrt[4]{\frac{\mathrm{Br}^2 D^2 \varepsilon}{\alpha\rho\mu_0 g}}.
\end{aligned}$$

Setting $D = 6 \cdot 10^{-3}\mathrm{m}$, $\mathrm{Br} = 1.3$, $\varepsilon = 3 \cdot 10^{-3}\mathrm{m}$, $\rho = 7368\mathrm{kg/m^3}$ and $g = 9.8\mathrm{m/s^2}$ (the values for the system presented), one obtains $r \gtrsim 24.78\mathrm{mm}$, that is, $r \gtrsim 4.13D$ for $\alpha = 1$.

Algorithm 5.1 Verlet list algorithm for high efficiency computation of neighbours

```
initialize variables
open output files
position particles with a random initial velocity of the order of $10^{-2}$ ▷ this is done before the compression starts!
initialize the Verlet lists
for $t \leqslant T_{\max}$ do
    if $k < T_r$ then
        descend the piston with an exponential law $\exp(t - 5)$ ▷ that is, the piston lowers smoothly during relaxation
    end if
    if $k = T_r$ then
        $H = H_0$ ▷ that is, when the relaxation ends the piston is positioned at the initial compression height
    end if
    if $T_r \leqslant k \leqslant T_h$ then
        $H = H - \Delta t \cdot V_c T / L$ ▷ that is, during the compression time we lower the piston by a constant factor
    end if
    construct the Verlet lists ▷ or reconstruct, if the threshold of maximum particle displacement is reached
    for each particle $p$ do
        compute the magnetic force of the walls on $p$
        compute the gravitational force on $p$
        for every particle $q$ in the Verlet list of $p$ do
            if $d(q, p) < r_c$ then
                compute the magnetic force between $q$ and $p$
            end if
        end for
        compute the friction force on $p$
    end for
    save computed interactions on output files
    call the Verlet integration subroutine
    advance the time step
    update $k = k + 1$
end for
save last iteration computed interactions on output files
close output files
finalize the Verlet lists
```

5.1.1 Validating the algorithm: choosing the parameters

In order to correctly use the Verlet list algorithm, one must tune the parameters. That is, a triplet (r_v, r_c, r_s) must be chosen in such a way that the optimized version of the simulation with the Verlet method is sufficiently similar to the non-optimized version of the simulation ($O(n^2)$, without the Verlet lists).

The selection of the parameters was done by running simulations with different Verlet radii, varying the cut-off radius accordingly to maintain $r_s = 4.13D$. More precisely, simulations were done for $r_v = 6.26, 7.26, 8.26, 9.26, 10.26, 11.26, 12.26$, with each of these groups having 3 runs with different initial conditions.

Figure 5.2 shows the results obtained. In black the dimensional force on the piston at maximum compression is exhibited: the stars represent the average force, with error bars denoting one standard deviation. The green strip represents a “convergence zone”: one standard deviation above and below the average force for the $O(n^2)$ algorithm. Simulations using Verlet lists that fall inside this zone can be considered equivalent, in a physical sense, to the naïve algorithm. One can see that as the Verlet radius increases, the simulations tend to this zone, with simulations with $r_v = 11.26D$, $r_c = 7.13D$, $r_s = 4.13D$ being the most efficient one for which the convergence is attained. Therefore, these were the parameters chosen.

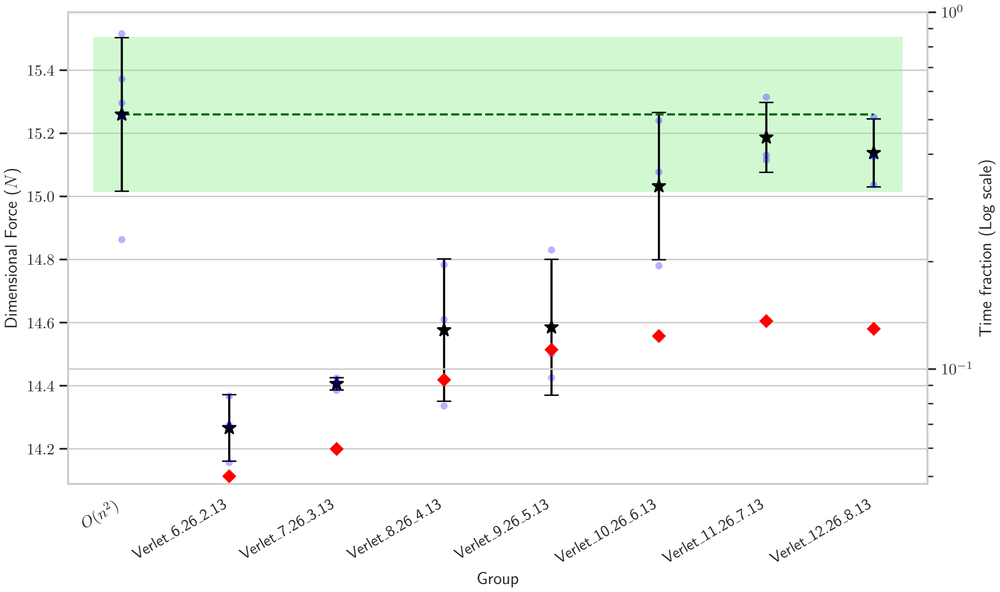

Figure 5.2 In black the mean dimensional force on the piston at maximum compression (stars) is plotted with error bars representing one standard deviation for each group of simulations: the “original” simulations, $O(n^2)$, and the simulations using the Verlet lists algorithm. The Verlet groups are named as “Verlet_[Verlet radius]_[cut-off radius]” and they are arranged in order of increasing r_v. In red the average simulation time of the Verlet simulations consumed, in terms of fractions of the “original” simulation, in logarithmic scale.

Furthermore, Figure 5.2 also shows the average fraction of simulation time that the Verlet simulations consumed in relation to the $O(n^2)$ algorithm using a logarithmic scale. One sees that, as expected, the Verlet simulations take considerably less time to run than the naïve algorithm. The $r_v = 11.26D$

group took, on average, *86% less time* to run (from ~18h with de $O(n^2)$ algorithm to a couple of hours with the Verlet lists).

Figures 5.3 and 5.4 show a few snapshots of the compression of the system for the Verlet (top row in both figures) and standard (bottom row in both figures) algorithms. We exhibit the magnitude of the compression forces the particles are subject to in Fig. 5.3 and the distribution of the Voronoi polygons in Fig. 5.4. We see that the two algorithms give rise to local differences, but the overall behaviour of both the compression force and the Voronoi tessellation is very similar.

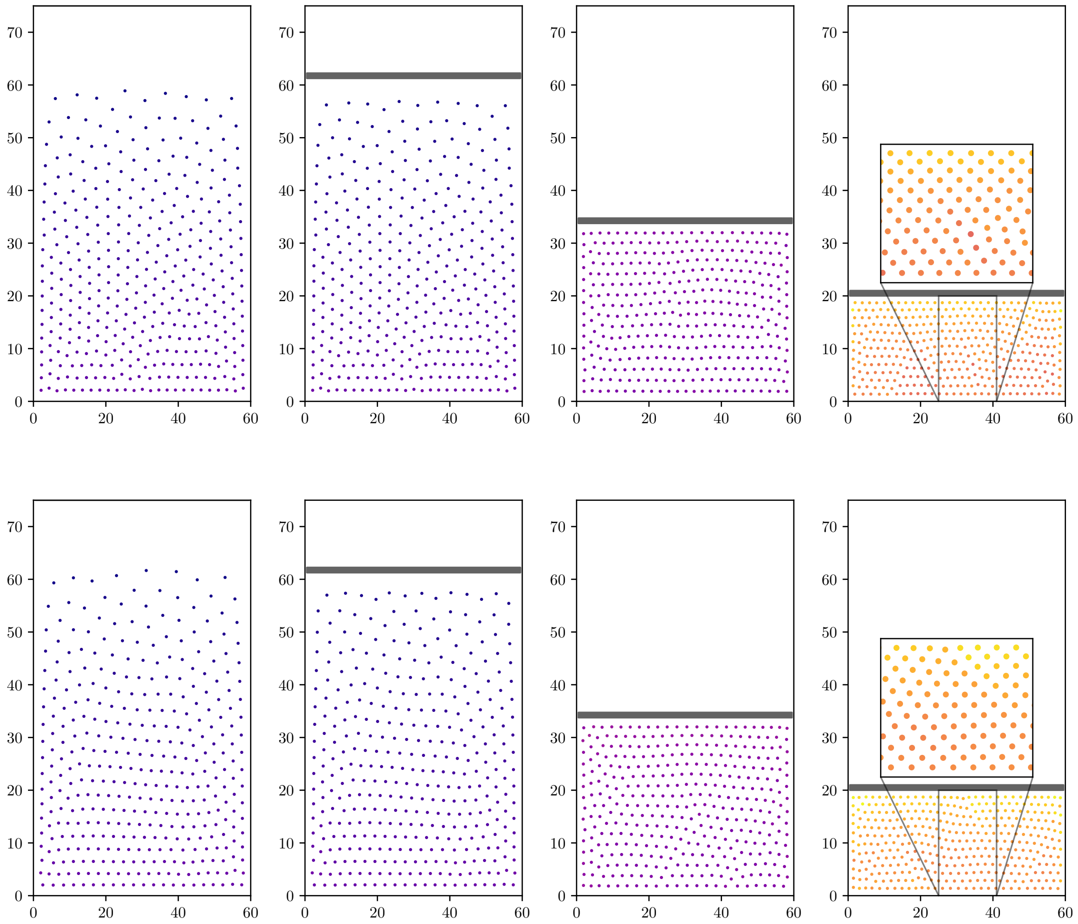

Figure 5.3 Snapshots of the compression of the system using the Verlet (top) and the standard (bottom) algorithms. The colors of the particles denote the magnitude of the compression force acting on them. The insets on the right columns show a zoom of the arrangement of the particles in the final compressed state.

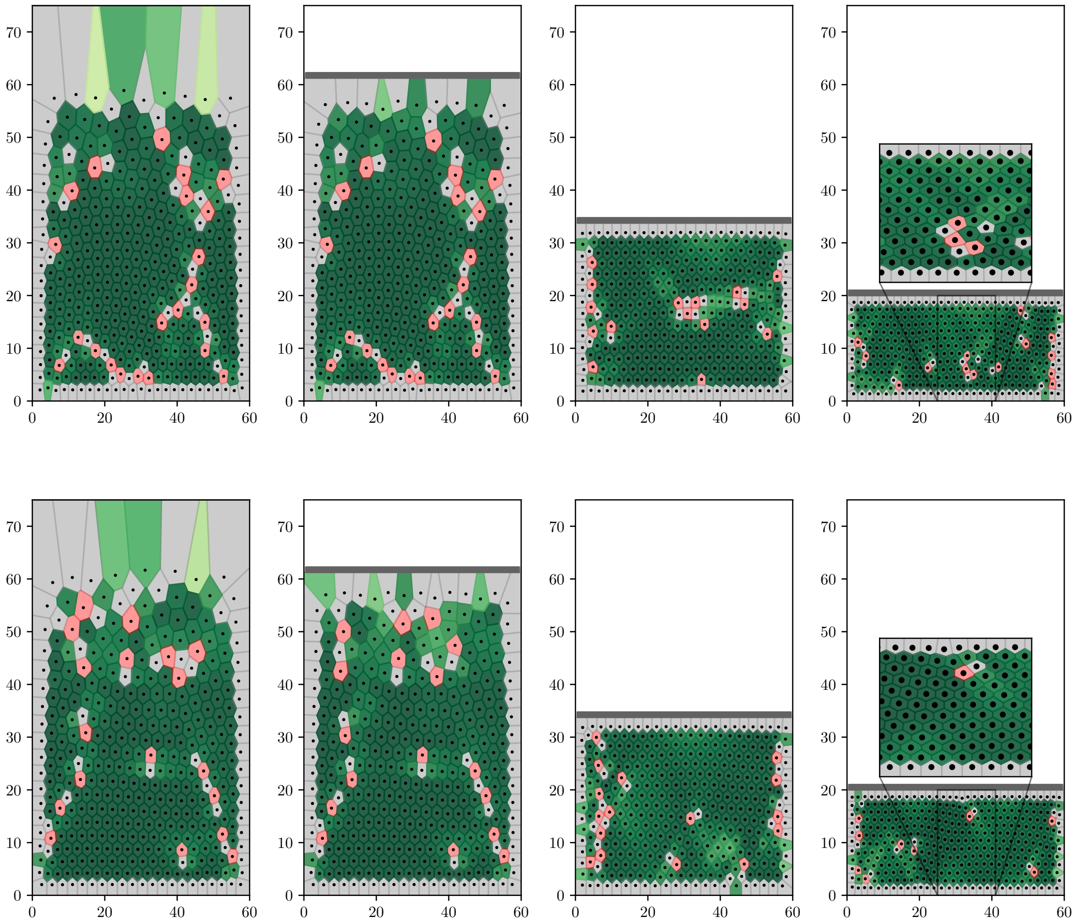

Figure 5.4 Snapshots of the compression of the system using the Verlet (top) and the standard (bottom) algorithms. The colors denote the different shapes of the polygons obtained by the Voronoi tesselation. The insets on the right columns show a zoom of the arrangement of the particles in the final compressed state.

When we scale the system size, either using the Verlet lists with radius 11.26D, or using the standard $O(n^2)$ algorithm, the force on the piston scales linearly, as shown in Figure 5.5. Fitting linear regressions on both Verlet simulations and the standard simulations for system sizes of 368, 460, 552, 644 and 736 particles, we obtain the equations The values used for the fit can be seen in Table 5.2. The means and standard deviations were computed for a set of 3 simulations for each system size.

Table 5.1 Linear fits for standard and Verlet methods.

	Angular Coeff.	Linear Coeff.	R^2
Standard	0.0213	7.59	0.99
Verlet	0.0189	8.32	0.99

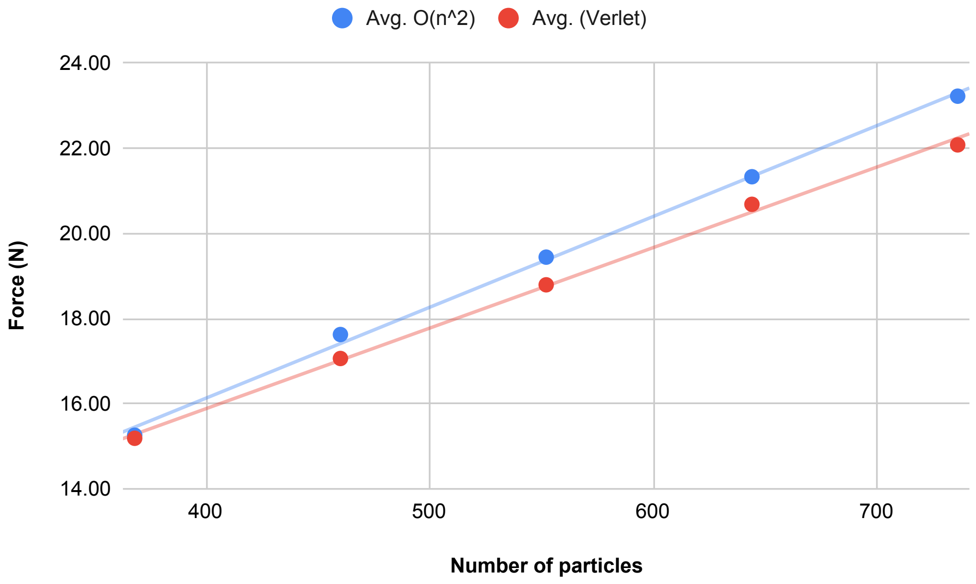

Figure 5.5 Linear fit of the dimensional force on the piston at maximum compression (in Newtons) versus the system size (number of particles).

The relative error is computed relative to the force in the Verlet systems. Note that, using the values in Table 5.1, we can project the relative error for an arbitrary system size. In fact, the relative error is given by

$$\frac{0.0189N + 8.32 - 0.0213N - 7.59}{0.0189N + 8.32} = \frac{-0.0024N + 0.73}{0.0189N + 8.32}, \tag{5.5}$$

where N denotes the system size. This is an equation of a hyperbola, which have horizontal asymptote (when $N \to \infty$) at $y = -12.7\%$! Put another way, we see that the amount of error (relatively) that the Verlet lists introduce does not grow unbounded. Not only that, but the hyperbola equation gives estimates on the relative error for each system size: by these estimates, an error of 10% only occurs for systems with sizes 8.5x or greater the original system size.

Table 5.2 Average and standard deviation of the dimensional force (in Newtons) on the piston at maximum compression for the standard simulations and Verlet simulations. Averages taken on 3 simulations for each system size.

# particles	Avg. force ($O(n^2)$)	Avg. force (Verlet)	Std. ($O(n^2)$)	Std. Verlet	% diff
368	15.26	15.19	0.24	0.11	-0.48
460	17.63	17.06	0.12	0.27	-3.30
552	19.44	18.79	0.19	0.09	-3.46
644	21.33	20.69	0.17	0.13	-3.13
736	23.23	22.08	0.14	0.31	-5.18
1472	36.24	33.88	—	0.42	-6.96
2208	47.86	44.46	—	0.18	-7.65

Lastly on the Verlet algorithm analysis, we studied the gain in simulation time. Figure 5.6 exhibits the average simulation times (in hours) for the Verlet runs (averaged over three executions for each system size) compared to the projected simulation times for the standard algorithm. In dashed lines we exhibit the fits of the form $y = an^b$. Naturally, the standard algorithm has $b = 2$ ($O(n^2)$). The Verlet algorithm has $b = 1.05$, which represents a significant gain. To exemplify this gain: the standard simulation for $N = 736$ took $\approx$ 3 days to run. For a Verlet simulation to run for this long, we would need to have $N \approx 8233$, i.e., a system $\approx$ 22 times greater than the original system ($N = 368$). We note that the grouping of points above and below the fit line for the Verlet algorithm is due to hardware, e.g., competing processes, and does not represent or exhibit an intrinsic behaviour of the system nor the algorithm.

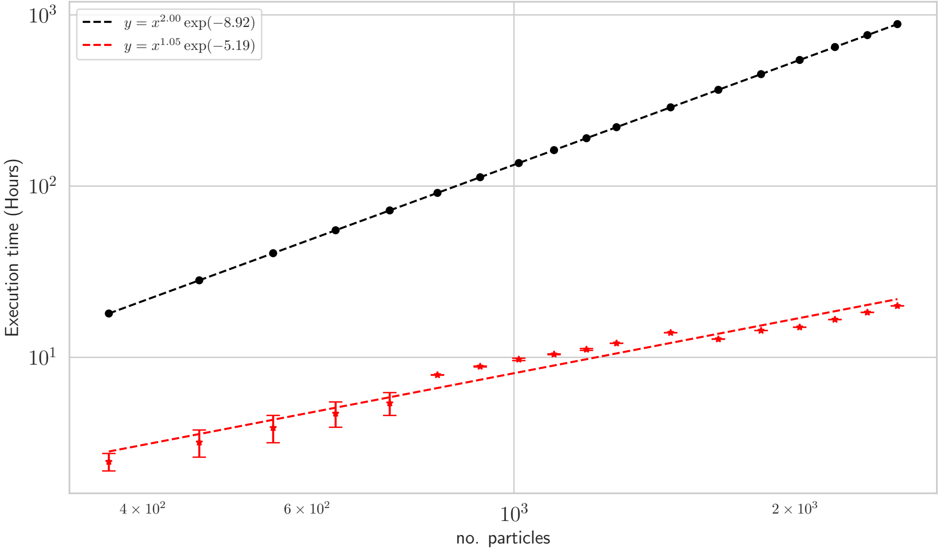

Figure 5.6 Average (red) and projected (black) simulation times for the Verlet and standard algorithms, respectively. In dashed lines we plot fits of the form $y = ax^b$. The red line obtained has $R^2 = 0.98$.

For completeness, in Figure 5.7 we exhibit the average dimensional forces for all system sizes we simulated, with respective standard deviations. The averages were calculated with 3 runs for each system size, with exception of $N = 1472$ for the standard algorithm, which only had one run due to computational limitations. We note that the best fit line to the red dots has $R^2 = 0.996$, reinforcing the linear scaling of the piston force with the system size, as expected.

We also exhibit, in Figure 5.8, the distribution of Voronoi regions at maximum compression by system size for the Verlet and $O(n^2)$ simulations. The numbers are averages of three runs for each system size and algorithm. The golden circles at the top plot represent the share of hexagons, while the red squares and blue triangles on the bottom plot represent the shares of pentagons and heptagons, respectively. We see that there is little variation between the $O(n^2)$ simulations and the Verlet simulations, showing that the underlying structure of the system is barely influenced when we use the Verlet algorithm in the simulations.

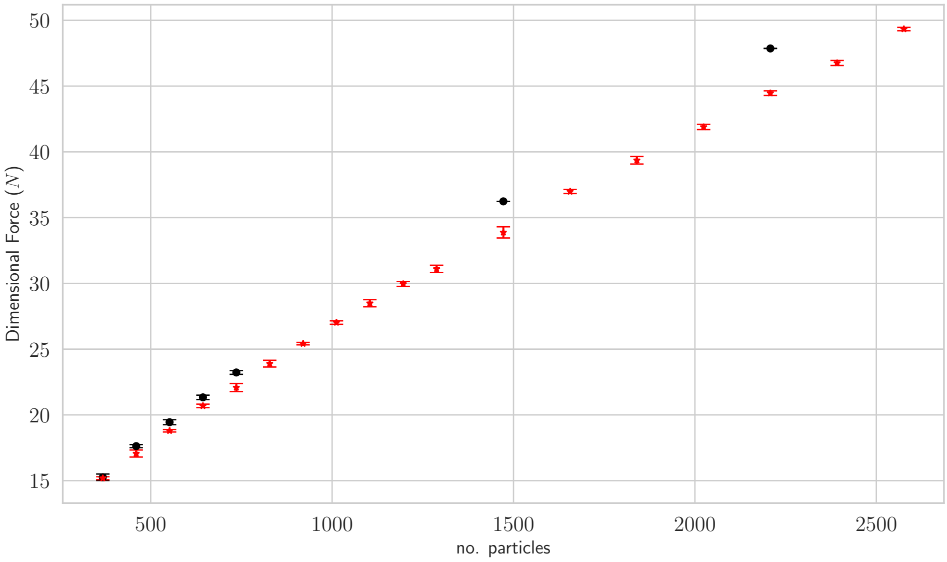

Figure 5.7 Dimensional forces on the piston at maximum compression (in Newtons) versus the system size (number of particles).

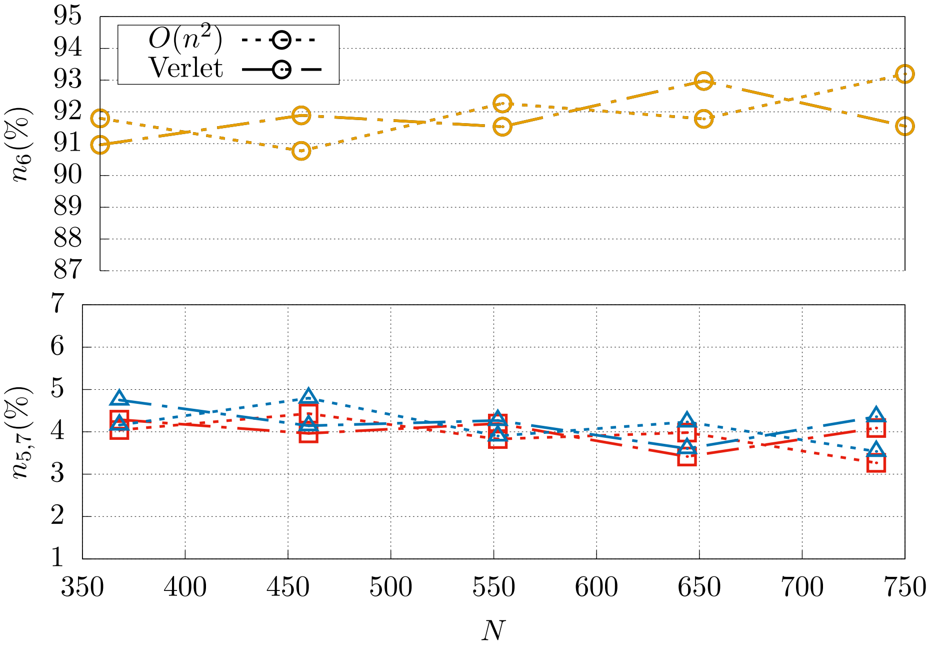

Figure 5.8 Voronoi polygons distribution by system size for the $O(n^2)$ algorithm (short dashed lines) and the Verlet algorithm (long-short dashed lines). The top region of the plot shows the percentage of hexagons, while the bottom part exhibit the percentages of pentagons (red squares) and heptagons (blue triangles). We did not include the standard deviations since they are small. Further details can be found on Appendix A.

As a last commentary, we would like to note that given a system of arbitrary size, one can (in principle) find Verlet triplets such that the discrepancy between the standard simulation and the Verlet simulation for that system is arbitrarily small and, the bigger the system is, the greater the gain in simulation time will be. Albeit simple, this is an important observation of the utility of the Verlet lists in optimizing simulation time.

5.1.2 Possible improvements to the algorithm

Despite the remarkable gains in performance we obtained through a straightforward application of the Verlet lists, we believe that there are a few paths to improving the simulation time further. Two such paths are to combine the Verlet list algorithm with other optimizing algorithm, as in [50, 51], where the authors mix cell lists with Verlet lists, and to parallelize the Verlet list algorithm as was done in [52] to take advantage of GPUs computing power.

None of these paths is straightforward, however. The adaptation of the Verlet algorithm described in the works cited is in and of itself a considerable task that requires a solid background in computational science, not to mention the (possibly less but not insignifcant) work to adapt the simulation code for allowing this "altered" Verlet list algorithm to be plugged in.

5.2 About data-driven machine learning — a quick overview

We live in the age of (big) data & AI. In the past decade or so, a handful of companies focused in advancing machine learning models have grown very rapidly, delivering models ever so slightly more powerful and accurate (suposedly). It is natural, therefore, that many possible applications of several different machine learning algorithms were developed. Two of them that are relevant to the present work are *genetic algorithms* and *symbolic regression*, which combined can be used for uncovering equations/physical laws from data [53].

5.2.1 Genetic algorithms, symbolic regression and the PySR library

Genetic programming was intially developed in the 1980s by J. R. Koze, generalizing parameter optimization to function optimization, initially coded as a tree of operations [54]. This class of algorithms rely on an iterative process, which can be lengthly and virtually impossible for complex problems. According to [55, p. 488], genetic algorithms are hybrids between gradient search strategies and Monte Carlo/Latin hypercube sampling methods.

A second type of machine learning that has been shown to be really useful for science applications is symbolic regression, which sole goal is to uncover human-interpretable symbolic models from real/numeric/synthetic data. Aiming to democratize and popularize symbolic regression for the sciences, Cranmer has developed an open-source Python package, named PySR, that implements symbolic regression in an extremely optimized fashion, taking advantage of its Julia backend. The technical details of the library can be found in the paper [53] and the code can be found on the GitHub repository, which is actively mantained by Cranmer and collaborators. Cheers to them for taking the time to develop a tool that will be unvaluable for many scientists to come!

To exemplify the usage of this package, we apply it to a very simple problem: find the equations that describes the motion of a damped harmonic oscillator, whose ODE is given by

$$mx'' + cx' + kx = 0, \tag{5.6}$$

where m is the mass of the oscillator, c is the damping constant and k is the spring constant. We simulate such an oscillator solving its ODE in Python and pass the resulting numerical solution data to the regressor. The raw LaTeX output of the model is

$$\frac{\cos\left(\left(x_0 - 0.0996\right) 1.00\right)}{e^{\left(x_0 - 0.0996\right) 0.0503}}, \tag{5.7}$$

which can be simplified to

$$\cos(t - 0.0996)\exp[0.0503(0.0996 - t)]. \tag{5.8}$$

In Figure 5.9 we compare the exact solution with the result of the model.

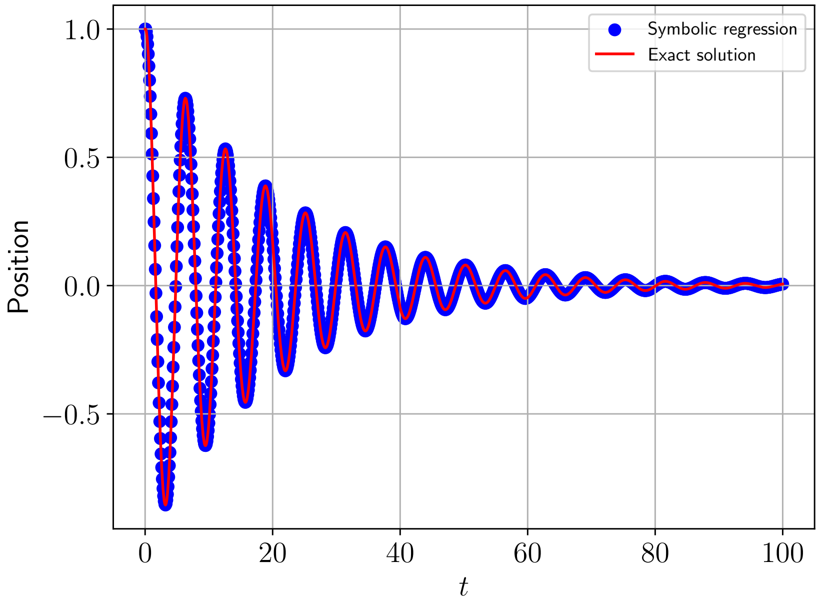

Figure 5.9 Usage example of the PySR Python package.

5.3 Modelling the free fall of the piston

One of the most straightforward applications that we see for the system studied in this work is the modelling/characterization of a magnetic damper: if we simply let the piston fall under the action of the gravity, the magnetic particles contained in the cell will act to counteract its movement, resulting in a damped motion. Similarly to a damped harmonic oscillator, if the piston mass is too great, the system will essentially explode. Therefore, this parameter must be adjusted carefully.

Another very relevant aspect of this damped motion is its intrinsic non-linear nature: what plays the role of the damper in the system is a layer of magnetic particles, that is, a discontinuous material, that interacts with the piston in a very non-linear way.

As we discussed in previous chapters, there are two friction models that can be used in our simulation: a dry friction model and a viscous friction model. The dry one gives rise to a stick-slip motion of the particles, while the viscous one allows for the particles to move more freely, as if they were immersed in a fluid. We chose to use the viscous friction model in the simulations of our damper to allow for a smaller hysteresis in the particles movement, essentially trying to make our damper not loose its damping effect throughout the bounces of the piston.

The way we conducted the simulation is the following: after the particles are initially positioned, we let the piston fall and move freely until it reaches a rest state. After that, we give it a slight nudge upwards (of $0.2D$) and allow it to fall and move freely again. The movement we study is the second one, after the nudge. We chose this approach in order to try to study the system near-linearity.

Our initial idea was to utilize the PySR symbolic regression library (described in the next section) to obtain the equation that describes the piston movement using the simulation data. Nevertheless, "applying PySR" does not immediately imply "obtaining the governing equation of the piston movement": since the core idea of the PySR library (and symbolic regression algorithms in general) is to find the mathematical law that best describes a given dataset, what we are rigorously finding with this algorithm is the *solution* to the governing equation of the piston movement. Knowing the general form of the solution is, therefore, a necessity if one is to use PySR . With that given, we can compare the symbolic regression output to the general form of the solution and determine the values of the coefficients in the general solution (that are the coefficients of the governing equation) for our specific system.

However, we could not do this in a satisfying manner because since the damper is non-linear we would need to include Jacobi elliptic functions in the search space of the symbolic regression algorithm, something that is not implemented yet and would take a considerable effort (not impossible, though), for which we did not have the time to do. In Fig. 5.10 we exhibit the height of the piston during the simulation (in non-dimensionalized units), which shows the oscillatory and damped motion, and in Fig. 5.11 we show the attempt of fit, using PySR, to this movement. The equation obtained was

$$10.53 + 0.02\cos(-1268.36t)\left[\exp(2.71\cos(-291.72t)) + \cos\left(10.96^{t} - 0.03\right)\right]. \tag{5.9}$$

We see that the fit is reasonably good, but does not capture the tail oscillations, for example.

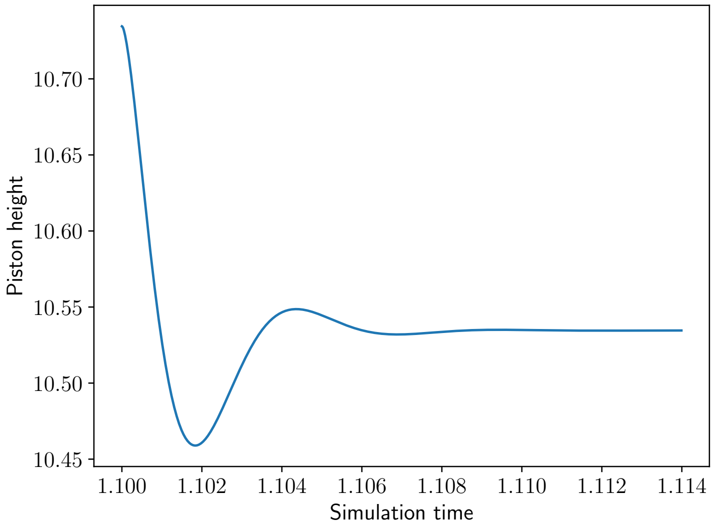

Figure 5.10 Height of the piston subject to free fall over a bed of particles. One can observe the oscillatory and damped motion.

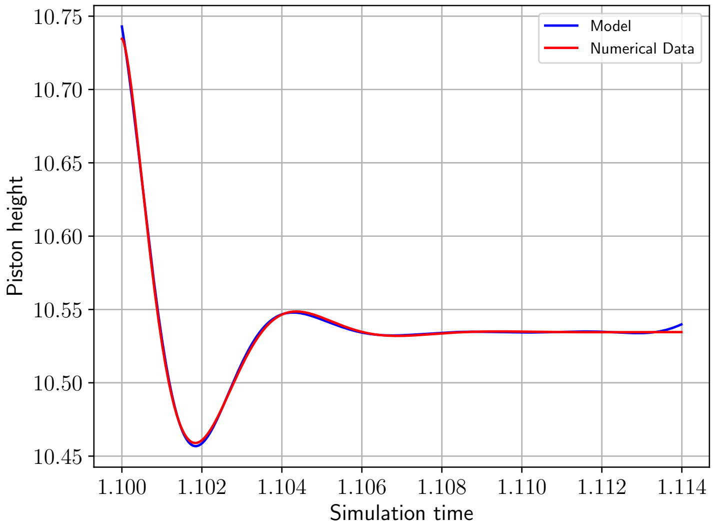

Figure 5.11 Attempt to use PySR to fit the damped motion of the free falling piston. One sees that the fit is reasonably good, but does not capture the tail oscillations, for example. The equation obtained is given in Eq. (5.9).

An alternative to the approach we took using PySR would be to apply SINDy — Sparse Identification of Nonlinear Dynamics [56], which consists of a method for extracting governing equations from data.

As a last comment, we note that in order to perform the regression we did using PySR one could not have used, instead, a standard least squares method. The reason is twofold: first, in the movement equation of the piston there will appear constants inside the arguments of the functions, e.g., the curve we are trying to fit could be, in principle, something as $a \log(bx) + c$, which would require a non-linear least squares fit; second, to use a least squares method, be it linear or non-linear, one needs to know in advance the form of the curve being fitted: is it a polynomial, a trigonometric function, a logarithm, etc? PySR does not require that: we work with a space of functions that include all these and, from there, try to find the best combination of these functions (together with standard operations) that best fit the data passed as input.

5.3.1 Van der Pol equation

Picking up on the fact that our damping is non-linear, with the non-linearity arising naturally from the particles, it is natural to consider a Van der Pol equation as the ideal equation to model the piston movement in such system. This is a second-order differential equation of the form

$$x''(t) - \mu(1 - x^2(t))x'(t) + x(t) = 0, \tag{5.10}$$

where μ is a scalar indicating the non-linearity and strength of damping.

Inspired by the differential equation of motion of a damped *harmonic* oscillator,

$$z'' + 2\lambda z' + \omega^2 z = g, \tag{5.11}$$

where g would be the acceleration of gravity and ω the angular frequency of the oscillator, we compared the movement of the piston to the solution of a Van der Pol-like equation of the form

$$z'' + 2\alpha(z^2 - 2z)z' + \omega^2 z = g_0, \tag{5.12}$$

where g_0 would be a modified acceleration of gravity including the repulsive effect of the granular layer.

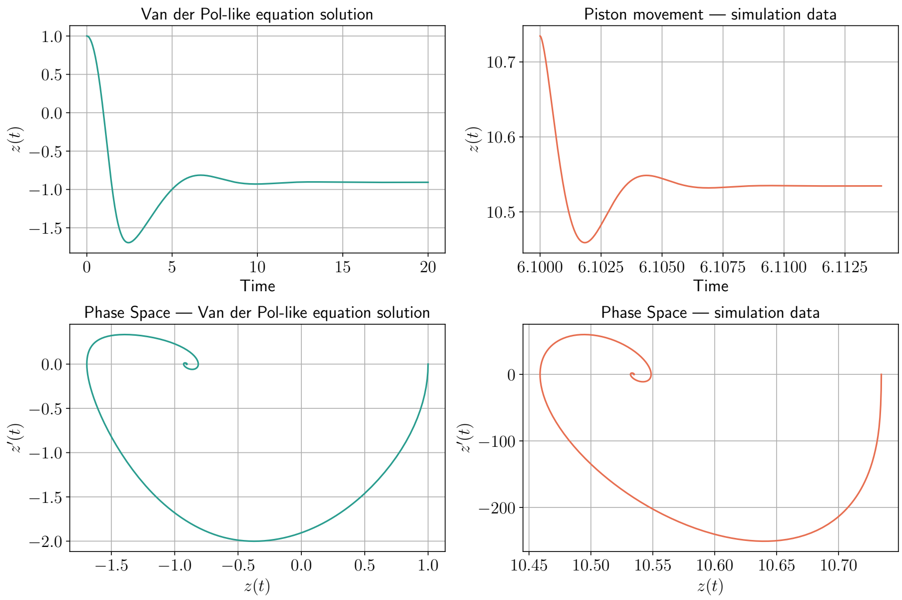

Figure 5.12 Comparison of the piston movement in free fall to the solution of a Van der Pol-like equation. The initial condition used was $z(0) = 1$, $z'(0) = 0$ and the parameters were $\omega = 1.05$, $g_0 = -1$ and $\alpha = 0.17$.

The resulting comparison is shown in Figure 5.12. We see that there is a very close similarity between the pairs of curves, suggesting that Eq. (5.12) at least captures the most relevant features and behaviours of the piston in our system.

CHAPTER 6

CONCLUSION AND FUTURE WORK

> "You know, for a mathematician, he did not have enough imagination.
> But he has become a poet and now he is fine."
> — David Hilbert, talking about an ex-student.

6.1 Conclusion

In this work we investigated the behavior of magnetic granular systems under compression, analysing both mono-disperse and bi-disperse configurations. Through numerical simulations validated against experimental observations, we explored the role and effects of different friction models, initial conditions, and piston velocity in shaping the system's dynamics. The use of structural metrics, such as Voronoi tessellations, provided a deeper understanding of the order/structure formation and force distribution within the granular bed.

A key contribution of this work was the implementation of optimized computational techniques, including the Verlet lists algorithm, which significantly reduced the computational cost of simulating long-range interactions and, consequently, the total overall time of the simulations. This allowed for the efficient modeling of larger systems, paving the way for more complex studies of granular systems influenced by magnetic forces. Furthermore, by adapting the simulation framework to analyze the free fall of the piston, we demonstrated how symbolic regression techniques could aid in deriving governing equations for a magnetic granular damper.

The findings presented here not only enhance our understanding of magnetically interacting granular materials but also suggest promising directions for future research, as detailed below.

6.2 Topics of future work

We believe that there are still a few lines of study worth pursuing. One of the more relevant ones, in our view, is the investigation and characterization of the propagation of defects, which must be related to the force chains, using the KTHNY-theory. This theory comes from the realm of statistical mechanics, and describes the melting of crystals in 2D. It relies heavily on statistical physics tools, such as renormalization, and the Burgers vector, a very useful tool in materials science for the study of lattice distortions in a crystal, which are intimaly related to this theory. To effectively apply this theory to our system, one would have to answer a few questions, such as what is the corresponding parameter to the temperature? The piston height? The dimensions of the cell? A combination of both? Maybe the more accurate analogy on our system is to a gas/liquid that condensates/cristalizes instead of a solid.

Another very relevant line of work is the full/complete study of the damper, identifying the parameters of the Van der Pol-like equation using symbolic regression with Jacobi elliptic functions, which we did not have time to tackle in this work.

Adapting the simulation to allow/account for contact between the particles and to study flow [17, 33] are also relevant lines of work. Lastly, one could also adapt our code to study polidispersity (three or more species of particles) as a proxy for real but yet unexplored systems.

Bibliography

[1] C. Bradford Barber, David P. Dobkin, and Hannu Huhdanpaa. "The Quickhull Algorithm for Convex Hulls". In: *ACM Trans. Math. Softw.* 22.4 (Dec. 1996), pp. 469–483. ISSN: 0098-3500. DOI: 10.1145/235815.235821. URL: https://doi.org/10.1145/235815.235821.

[2] Luciana Maria Dias de Ávila et al. *Os 60 anos do Departamento de Matemática da UnB*. 2022. URL: https://issuu.com/lfeditorial/docs/60_anos_matematica_unb_digital.

[3] IF Sudeste MG. *Biblioteca esclarece sobre o que é o conceito Capes*. URL: https://encurtador.com.br/nATVu (visited on 02/11/2025).

[4] Próximo Nível. *IMPA Tech: instituto vai formar profissionais para tecnologia e inovação*. URL: https://proximonivel.embratel.com.br/impa-tech/?utm_source=twitter&utm_medium=ads&utm_campaign=inovacao (visited on 02/11/2025).

[5] Adeene Denton. *How Grad School Turned me into Darth Vader*. URL: https://medium.com/@adeene.denton/how-grad-school-turned-me-into-darth-vader-9c5bd7bd3ae7 (visited on 02/11/2025).

[6] Tanentzapf Lab. *Max Pertuz quote*. URL: https://twitter.com/TanentzapfLab/status/1667564350284914689?t=qC3CEVMuhAQBzeSqA1GYOQ&s=19 (visited on 02/11/2025).

[7] W. Thomson. "Floating Magnets". In: *Nature* 18 (1878), pp. 13–14. DOI: https://doi.org/10.1038/018013b0.

[8] V G Bar'yakhtar, A N Bogdanov, and D A Yablonskiĭ. "The physics of magnetic domains". In: *Soviet Physics Uspekhi* 31.9 (Sept. 1988), p. 810. DOI: 10.1070/PU1988v031n09ABEH005621. URL: https://dx.doi.org/10.1070/PU1988v031n09ABEH005621.

[9] A. A. Afanas'ev et al. "Adjustable Magnetic Gear". In: *Russian Electrical Engineering* 88.7 (July 2017), pp. 448–52. DOI: https://doi.org/10.3103/S1068371217070057.

[10] X. Wu et al. "Ferromagnetic liquid droplets with adjustable magnetic properties". In: *Proc. Natl. Acad. Sci. U.S.A.* 118.8 (2021). DOI: https://doi.org/10.1073/pnas.2017355118.

[11] Hui Yang et al. "Flux adjustable permanent magnet machines: A technology status review". In: *Chinese Journal of Electrical Engineering* 2.2 (2016), pp. 14–30. DOI: 10.23919/CJEE.2016.7933123.

[12] Dmytro Apalkov, Bernard Dieny, and J. M. Slaughter. "Magnetoresistive Random Access Memory". In: *Proceedings of the IEEE* 104.10 (2016), pp. 1796–1830. DOI: 10.1109/JPROC.2016.2590142.

[13] Sumio Ikegawa et al. "Magnetoresistive Random Access Memory: Present and Future". In: *IEEE Transactions on Electron Devices* 67.4 (2020), pp. 1407–1419. DOI: 10.1109/TED.2020.2965403.

[14] A. B. Guimarães, F. R. Cunha, and R. G. Gontijo. "The influence of hydrodynamic effects on the complex susceptibility response of magnetic fluids undergoing oscillatory fields: New insights for magnetic hyperthermia". In: *Physics of Fluids* 32.1 (Jan. 2020). 012008. ISSN: 1070-6631. DOI: 10.1063/1.5128411. eprint: https://pubs.aip.org/aip/pof/article-pdf/doi/10.1063/1.5128411/12322456/012008_1_online.pdf. URL: https://doi.org/10.1063/1.5128411.

[15] J.A.C. Modesto et al. "Experimental and numerical investigation of the compression and expansion of a granular bed of repelling magnetic disks". In: *Granular Matter* (2022). DOI: https://doi.org/10.1007/s10035-022-01268-w.

[16] K. Tsuchikusa et al. “Disordering two-dimensional magnet-particle configurations using bidispersity”. In: *The Journal of Chemical Physics* 158.21 (June 2023). 214501. ISSN: 0021-9606. DOI: 10.1063/5.0149803. eprint: https://pubs.aip.org/aip/jcp/article-pdf/doi/10.1063/5.0149803/17914802/214501_1_5.0149803.pdf. URL: https://doi.org/10.1063/5.0149803.

[17] Geoffroy Lumay et al. “Flow of magnetic repelling grains in a two-dimensional silo”. In: *Papers in Physics* 7 (Sept. 2015), p. 070013. DOI: 10.4279/pip.070013. URL: https://www.papersinphysics.org/papersinphysics/article/view/266.

[18] A. van Blaaderen et al. “Manipulating the self assembly of colloids in electric fields”. In: *Eur. Phys. J. Spec. Top.* 222 (Nov. 2013), pp. 2895–2909. DOI: https://doi.org/10.1140/epjst/e2013-02065-0.

[19] A. Gerber et al. “Magnetoresistance of granular ferromagnets”. In: *Phys. Rev. B* 55 (10 Mar. 1997), pp. 6446–6452. DOI: 10.1103/PhysRevB.55.6446. URL: https://link.aps.org/doi/10.1103/PhysRevB.55.6446.

[20] Masahiro Hiraoka et al. “Current Status and Perspectives of Hyperthermia in Cancer Therapy”. In: *AIP Conference Proceedings* 716.1 (Aug. 2004), pp. 102–108. ISSN: 0094-243X. DOI: 10.1063/1.1796592. eprint: https://pubs.aip.org/aip/acp/article-pdf/716/1/102/12190651/102_1_online.pdf. URL: https://doi.org/10.1063/1.1796592.

[21] N. A. Usov and B. Ya. Liubimov. “Dynamics of magnetic nanoparticle in a viscous liquid: Application to magnetic nanoparticle hyperthermia”. In: *Journal of Applied Physics* 112.2 (July 2012). 023901. ISSN: 0021-8979. DOI: 10.1063/1.4737126. eprint: https://pubs.aip.org/aip/jap/article-pdf/doi/10.1063/1.4737126/13450923/023901_1_online.pdf. URL: https://doi.org/10.1063/1.4737126.

[22] C. F. Alegretti and Rafael Gabler Gontijo. “New insights on boundary layer control using magnetic fluids: A numerical study”. In: *Journal of Magnetism and Magnetic Materials* 514 (2020). DOI: https://doi.org/10.1016/j.jmmm.2020.167133.

[23] Francisco Ricardo Cunha and Rafael Gabler Gontijo. “Revisiting the governing equations of a magnetic suspension of polar particles: From microhydrodynamics analysis to rheological response”. In: *Physics of Fluids* 36.8 (Aug. 2024). DOI: https://doi.org/10.1063/5.0223500.

[24] Urs Gasser et al. “Melting of Crystals in Two Dimensions”. In: *ChemPhysChem* 11.5 (2010), pp. 963–970. DOI: https://doi.org/10.1002/cphc.200900755.

[25] Nadezhda Gribova et al. “How Close to Two Dimensions Does a Lennard-Jones System Need to Be to Produce a Hexatic Phase?” In: *The Journal of Chemical Physics* 135.5 (2011). DOI: https://doi.org/10.1063/1.3623783.

[26] Xinliang Xu and Stuart A. Rice. “Liquid-to-hexatic phase transition in a quasi-two-dimensional colloid system”. In: *Physical Review E* 78.1 (2008). DOI: https://doi.org/10.1103/PhysRevE.78.011602.

[27] K. Zahn, R. Lenke, and G. Maret. “Two-Stage Melting of Paramagnetic Colloidal Crystals in Two Dimensions”. In: *Physical Review Letters* 82.13 (1999), pp. 2721–2724. DOI: https://doi.org/10.1103/PhysRevLett.82.2721.

[28] K.W. Yung, P.B. Landecker, and D.D. Villani. “An analytic solution for the force between two magnetic dipoles”. In: *Physical Separation in Science and Engineering* 9 (1998), pp. 39–52. DOI: https://doi.org/10.1155/1998/79537.

[29] E. Pennestri et al. “Review and comparison of dry friction force models”. In: *Nonlinear Dyn* 83 (2016), pp. 1785–1801. DOI: https://doi.org/10.1007/s11071-015-2485-3.

[30] J.A.C. Modesto, F.R Cunha, and Y.D. Sobral. “Aggregation patterns in systems composed of few magnetic particles”. In: *Journal of Magnetism and Magnetic Materials* 512 (2020), p. 166664. ISSN: 0304-8853. DOI: https://doi.org/10.1016/j.jmmm.2020.166664. URL: https://www.sciencedirect.com/science/article/pii/S0304885319327854.

[31] K.W. Yung, P.B. Landecker, and D.D. Villani. "An analytic solution for the torque between two magnetic dipoles". In: *Physical Separation in Science and Engineering* 10 (1999), pp. 29–33. DOI: https://doi.org/10.1155/1999/97902.

[32] Ernst Hairer, Lubich Christian, and Wanner Gerhard. "Geometric numerical integration illustrated by the Störmer–Verlet method". In: *Acta Numerica* 12 (July 2003), pp. 399–450. DOI: https://doi.org/10.1017/S0962492902000144.

[33] David Hernández-Enrıquez, Geoffroy Lumay, and Felipe Pacheco-Vázquez. "Discharge of repulsive grains from a silo: experiments and simulations". In: *EPJ Web of Conferences*. Vol. 140. EDP Sciences. 2017, p. 03089.

[34] D Dane Quinn. "A new regularization of Coulomb friction". In: *J. Vib. Acoust.* 126.3 (2004), pp. 391–397.

[35] Atsuyuki Okabe et al. *Spatial Tessellations: Concepts and Applications of Voronoi Diagrams, Second Edition*. 2nd ed. Wiley Series in Probability and Statistics. John Wiley & Sons Ltd, 2000. ISBN: 9780471986355. URL: https://encurtador.com.br/1w7xl.

[36] David M. Mount. *Lecture notes in Computational Geometry,* Oct. 2021. URL: http://www.cs.umd.edu/class/fall2021/cmsc754/Lects/cmsc754-fall-2021-lects.pdf.

[37] Qhull. *Qvoronoi: Convex hull and Voronoi diagram software*. Accessed: 2025-04-22. 2024. URL: http://www.qhull.org/html/qvoronoi.htm.

[38] Jonathan S. Greenfield. *A Proof for a QuickHull Algorithm*. 1990.

[39] *Stack Overflow*. 2022. URL: https://mathoverflow.net/questions/436080/how-to-characterize-the-regularity-of-a-polygon.

[40] Thomas Williams, Colin Kelley, and many others. *Gnuplot 6.0: an interactive plotting program*. http://gnuplot.sourceforge.net/. Mar. 2025.

[41] Jan Kleinert. *Simulating Granular Material using Nonsmooth Time-Stepping and a Matrix-free Interior Point Method*. ResearchGate. 2015. DOI: 10.13140/RG.2.1.2910.9204. URL: https://doi.org/10.13140/RG.2.1.2910.9204.

[42] Stephan Keller and Heinrich M. Jaeger. "Aleatory architectures". In: *Granular Matter* 18.1 (2016), p. 29. DOI: 10.1007/s10035-016-0629-x. URL: https://doi.org/10.1007/s10035-016-0629-x.

[43] Astropy Collaboration et al. "The Astropy Project: Sustaining and Growing a Community-oriented Open-source Project and the Latest Major Release (v5.0) of the Core Package". In: *apj* 935.2, 167 (Aug. 2022), p. 167. DOI: 10.3847/1538-4357/ac7c74. arXiv: 2206.14220 `[astro-ph.IM]`.

[44] Kevin H. Knuth. "Optimal data-based binning for histograms and histogram-based probability density models". In: *Digital Signal Processing* 95 (2019), p. 102581. ISSN: 1051-2004. DOI: https://doi.org/10.1016/j.dsp.2019.102581. URL: https://www.sciencedirect.com/science/article/pii/S1051200419301277.

[45] Emilien Azéma and Farhang Radjaı. "Force chains and contact network topology in sheared packings of elongated particles". In: *Phys. Rev. E* 85 (3 Mar. 2012), p. 031303. DOI: 10.1103/PhysRevE.85.031303. URL: https://link.aps.org/doi/10.1103/PhysRevE.85.031303.

[46] M.P. Allen and D.J. Tildesley. *Computer Simulation of Liquids - code examples*. https://github.com/Allen-Tildesley/examples/blob/master/verlet_list_module.f90. 2017.

[47] M.P. Allen and D.J. Tildesley. *Computer Simulation of Liquids, Second Edition*. 2nd ed. Oxford University Press, 2017.

[48] Ariel A. Chialvo and Pablo G. Debenedetti. "On the Use of the Verlet Neighbor List in Molecular Dynamics". In: *Computer Physics Communications* 60.2 (Sept. 1990), pp. 215–224. DOI: https://doi.org/10.1016/0010-4655(90)90007-N.

[49] Loup Verlet. "Computer "Experiments" on Classical Fluids. I. Thermodynamical Properties of Lennard-Jones Molecules". In: *Physical Review* 159.1 (July 1967), pp. 98–103. DOI: https://doi.org/10.1103/PhysRev.159.98.

[50] Pedro Gonnet. "Pairwise verlet lists: Combining cell lists and verlet lists to improve memory locality and parallelism". In: *Computational Chemistry* 33.1 (Jan. 2012), pp. 76–81.

[51] Zhenhua Yao et al. "Improved neighbor list algorithm in molecular simulations using cell decomposition and data sorting method". In: *Computer Physics Communications* 161 (June 2004), pp. 27–35.

[52] Tyson J. Lipscomb, Anqi Zou, and Samuel S. Cho. "Parallel verlet neighbor list algorithm for GPU-optimized MD simulations". In: *Proceedings of the ACM Conference on Bioinformatics, Computational Biology and Biomedicine*. BCB '12. Orlando, Florida: Association for Computing Machinery, 2012, pp. 321–328. ISBN: 9781450316705. DOI: 10.1145/2382936.2382977. URL: https://doi.org/10.1145/2382936.2382977.

[53] Miles Cranmer. *Interpretable Machine Learning for Science with PySR and SymbolicRegression.jl*. 2023. arXiv: 2305.01582 `[astro-ph.IM]`. URL: https://arxiv.org/abs/2305.01582.

[54] John R. Koza. *Genetic programming: on the programming of computers by means of natural selection*. 1st ed. MIT Press, 1992.

[55] Steven L. Brunton, Bernd R. Noack, and Petros Koumoutsakos. "Machine Learning for Fluid Mechanics". In: *Annual Review of Fluid Mechanics* 52 (2020), pp. 477–508. DOI: https://doi.org/10.1146/annurev-fluid-010719-060214.

[56] Steven L. Brunton, Joshua L. Proctor, and J. Nathan Kutz. "Discovering governing equations from data by sparse identification of nonlinear dynamical systems". In: *Proceedings of the National Academy of Sciences of the United States of America* 113.15 (Apr. 2016). Epub 2016 Mar 28, pp. 3932–3937. DOI: 10.1073/pnas.1517384113.

APPENDIX A

EXTRA DATA FROM THE SIMULATIONS

A.1 Parameters of the bi-disperse simulations

Table A.1 Simulations parameters for the different aspect ratios in the bi-disperse system. The diameters D_1 and D_2 are given in millimeters, the final height H_f is given in terms of D_1 and V_c is equal to 1 millimiter/second.

	$D_2/D_1 = 3/5$		$D_2/D_1 = 2.5/5$		$D_2/D_1 = 6/8$		$D_2/D_1 = 3.75/5$	
R	H_f $(\times D_1)$	T	H_f $(\times D_1)$	T	H_f $(\times D_1)$	T	H_f $(\times D_1)$	T
0.00	14.0000	$0.375/V_c$	14	$0.375/V_c$	22.4	$0.2658/V_c$	14	$0.375/V_c$
0.01	13.9104	$0.375448/V_c$	—	—	—	—	—	—
0.05	13.5520	$0.37724/V_c$	—	—	—	—	—	—
0.10	13.1040	$0.37948/V_c$	12.95	$0.38025/V_c$	21.42	$0.27364/V_c$	13.3875	$0.3780625/V_c$
0.15	12.6560	$0.38172/V_c$	—	—	—	—	—	—
0.20	12.2080	$0.38396/V_c$	11.9	$0.3855/V_c$	20.44	$0.28148/V_c$	12.775	$0.381125/V_c$
0.25	11.7600	$0.3862/V_c$	—	—	—	—	—	—
0.30	11.3120	$0.38844/V_c$	10.85	$0.39075/V_c$	19.46	$0.28932/V_c$	12.1625	$0.3841875/V_c$
0.35	10.8640	$0.39068/V_c$	—	—	—	—	—	—
0.40	10.4160	$0.39292/V_c$	9.8	$0.396/V_c$	18.48	$0.29716/V_c$	11.55	$0.38725/V_c$
0.45	9.9680	$0.39516/V_c$	9.275	$0.398625/V_c$	17.99	$0.30108/V_c$	11.24375	$0.38878125/V_c$
0.50	9.5200	$0.3974/V_c$	8.75	$0.40125/V_c$	17.5	$0.305/V_c$	10.9375	$0.3903125/V_c$
0.55	9.0720	$0.39964/V_c$	8.225	$0.403875/V_c$	17.01	$0.30892/V_c$	10.63125	$0.39184375/V_c$
0.60	8.6240	$0.40188/V_c$	7.7	$0.4065/V_c$	16.52	$0.31284/V_c$	10.325	$0.393375/V_c$
0.65	8.1760	$0.40412/V_c$	—	—	—	—	—	—
0.70	7.7280	$0.40636/V_c$	6.65	$0.41175/V_c$	15.54	$0.32068/V_c$	9.7125	$0.3964375/V_c$
0.75	7.2800	$0.4086/V_c$	—	—	—	—	—	—
0.80	6.8320	$0.41084/V_c$	5.6	$0.417/V_c$	14.56	$0.32852/V_c$	9.1	$0.3995/V_c$
0.85	6.3840	$0.41308/V_c$	—	—	—	—	—	—
0.90	5.9360	$0.41532/V_c$	4.55	$0.42225/V_c$	13.58	$0.33636/V_c$	8.4875	$0.4025625/V_c$
0.95	5.4880	$0.41756/V_c$	—	—	—	—	—	—
0.99	5.1296	$0.419352/V_c$	—	—	—	—	—	—
1.00	5.0400	$0.4198/V_c$	3.5	$0.4275/V_c$	12.6	$0.3442/V_c$	7.875	$0.405625/V_c$

A.2 Voronoi regions distribution for the Verlet and $O(n^2)$ simulations comparison

Table A.2 Mean and standard deviation of the distributions of Voronois regions for the Verlet and $O(n^2)$ simulations. The statistics were obtained with three runs of each system size for each algorithm.

	Verlet simulations						$O(n^2)$ simulations					
	pentagons		hexagons		heptagons		pentagons		hexagons		heptagons	
N	mean	std. dev.	mean	std. dev.	mean	std. dev.	mean	std. dev.	mean	std. dev.	mean	std. dev.
368	0.04	0.004	0.91	0.003	0.05	0.002	0.04	0.008	0.92	0.02	0.04	0.01
460	0.04	0.006	0.92	0.02	0.04	0.009	0.04	0.007	0.91	0.02	0.05	0.01
552	0.04	0.01	0.92	0.02	0.04	0.01	0.04	0.001	0.92	0.004	0.04	0.003
644	0.03	0.005	0.93	0.006	0.04	0.003	0.04	0.007	0.92	0.02	0.04	0.01
736	0.04	0.005	0.92	0.01	0.04	0.007	0.03	0.005	0.93	0.01	0.04	0.004

All data is available upon reasonable request.

Appendix B

Code structure and outputs

The conceptual structure of the code for the "naïve" $O(N^2)$ algorithm is shown below in Figure B.1.

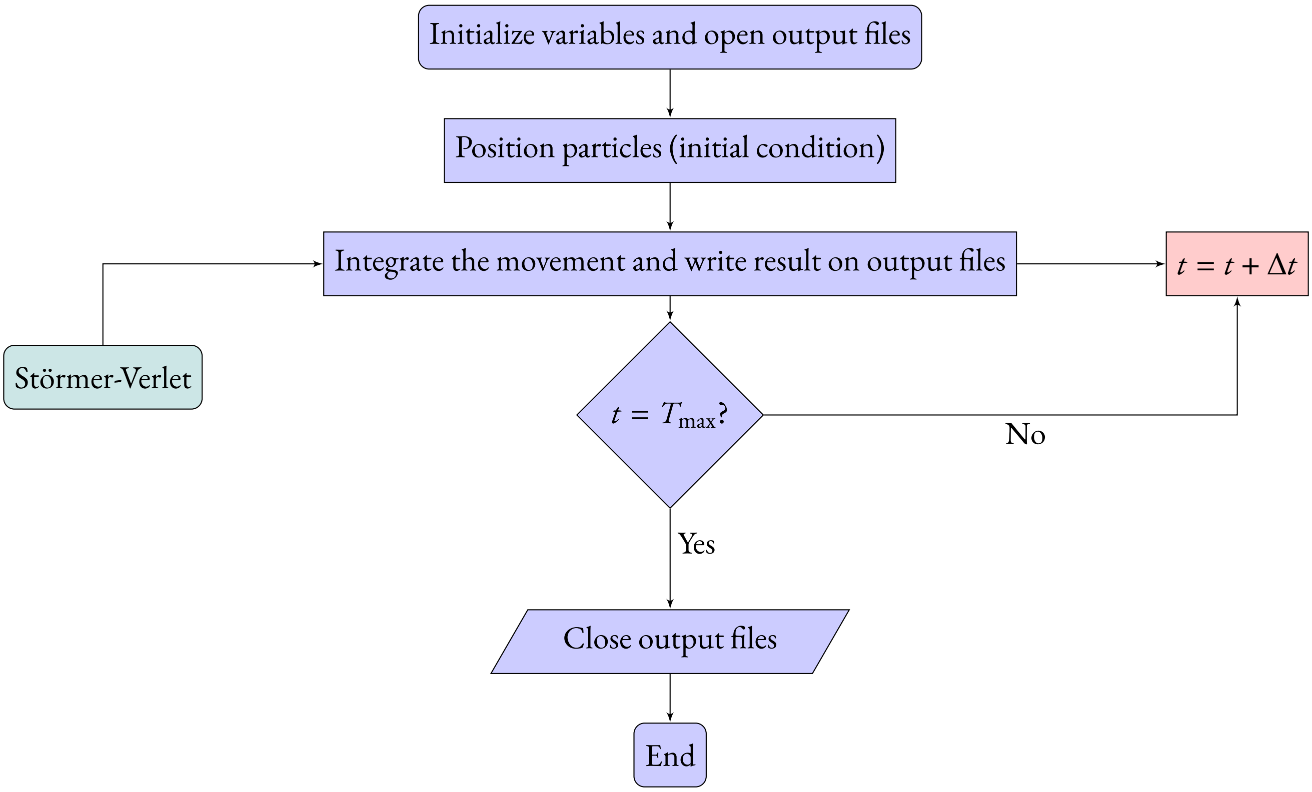

Figure B.1 Code workflow for the $O(N^2)$ algorithm.

To implement such algorithm, we build on previous work of Jorge Augusto, who developed the first working version of the code for the work presented in [15]. To improve readability and to allow for easier parameter adjustment and tuning, we separated the code in Fortran 90 modules. Figure B.2 exhibits the dependece between said modules. The module at the end of an arrow is called/used by the module on the origin of the arrow. We highlighted in gray the main module, in purple the data cleaning routines and in orange the Verlet module.

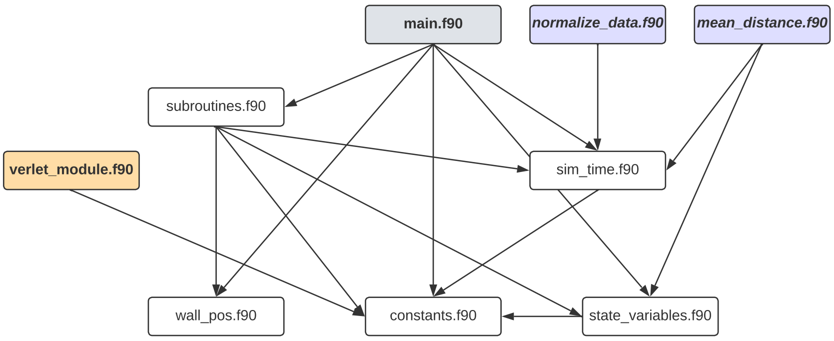

Figure B.2 Dependency diagram for the modules of the code.

The contents of each module are:

- `constants.f90`: declaration of global constants like π, number of particles, etc.
- `sim_time.f90`: declaration of the amount of timesteps the simulation will take
- `state_variables.f90`: declaration of the variables that will contain the particles' data (velocities, positions, etc.) and control variables for saving the data on output files
- `wall_pos.f90`: declaration of the cell dimensions
- `subroutines.f90`: contains all the subroutines used in the simulation
- `main.f90`: contains the algorithm *per se*
- `mean_distance.f90`: used after the simulation finishes to generate a file of particles average distances at each time step
- `normalize_data.f90`: used after the simulation finishes to generate files with processed data from the simulation, which is used to conduct the analysis
- `verlet_module.f90`: used to initialize and (re)build the Verlet lists

When using the Verlet lists module, the verification in Fig. B.3 is performed throughout the simulation.

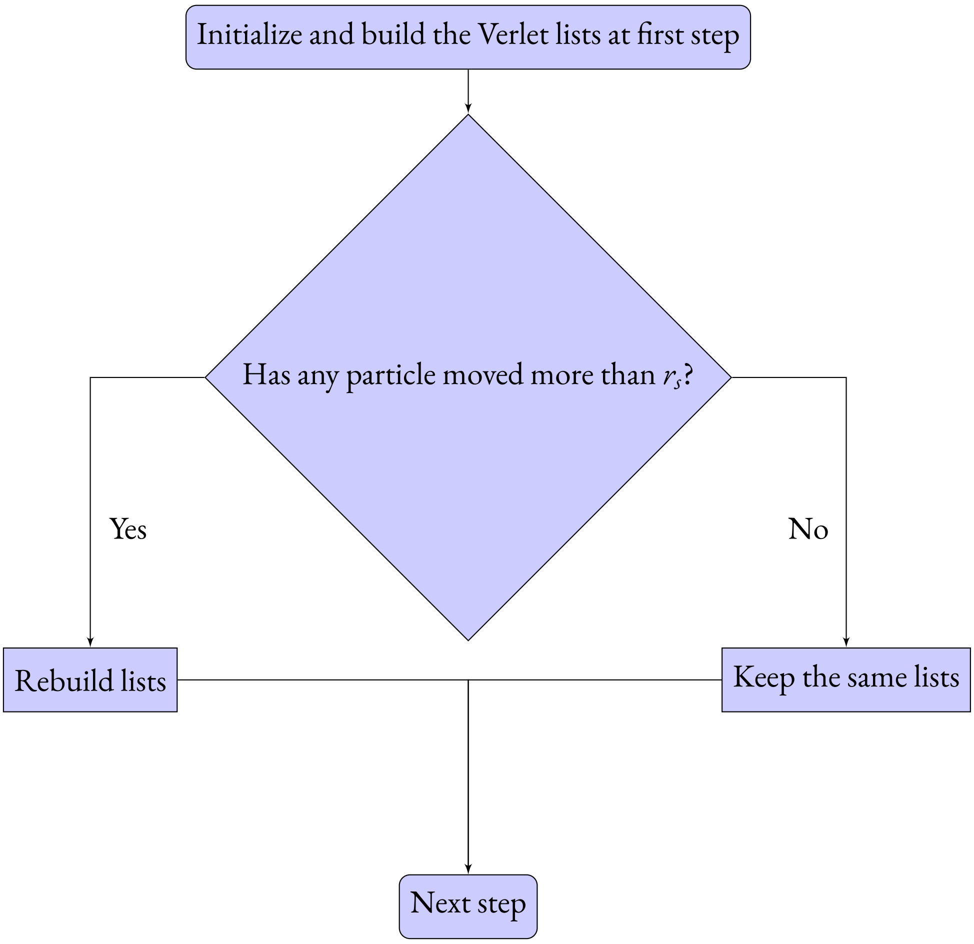

Figure B.3 Verlet list algorithm verification.

To run the simulation, we use the following script shell script.

```
#! /usr/bin/env sh

compile_and_run() {
    local dir=$1
    cd $dir

    # simulation start time
    start_time=$(date +%s)

    gfortran constants.f90 sim_time.f90 walls_pos.f90 state_variables.f90
        subroutines.f90 verlet_module_clean.f90 main.f90
    ./a.out

    # simulation end time
    end_time=$(date +%s)

    # simulation duration (in seconds)
    duration_simulation=$((end_time - start_time))

    # cleaning start time
    start_time=$(date +%s)

    gfortran constants.f90 sim_time.f90 state_variables.f90 mean_distance.f90
    ./a.out

    gfortran constants.f90 sim_time.f90 normalize_data.f90
    ./a.out

    # cleaning end time
    end_time=$(date +%s)

    # cleaning duration (in seconds)
```

```
    duration_clean=$((end_time - start_time))

    # saving
    {
        echo "Tempo simulação (segundos): $duration_simulation seconds"
        echo "Tempo limpeza (segundos): $duration_clean seconds"
    } > exec_time.dat

    cd $current_dir
}

current_dir=$(pwd)

for dir in "$@"
do
    compile_and_run "$dir"
done
```

We define the function `compile_and_run()` that

i. compile and runs the simulation, measuring the execution time in seconds

ii. compile and run the mean distances post-processing routine and the normalizing post-processing routine, measuring the execution time in seconds

iii. saves the measured times in a file

After the shell script is executed, we have several output files:

- `posPart.dat`: contains particles positions at every 250 time steps
- `velPart.dat`: contains particles velocities at every 250 time steps
- `forPart.dat`: contains particles forces at every 250 time steps
- `comPart.dat`: contains the compression forces experienced by each particle at every 250 time steps
- `piston.dat`: contains piston positions at every 250 time steps
- `posPart_0.dat`: contains particles positions at every 10 time steps
- `velPart_0.dat`: contains particles velocities at every 10 time steps
- `forPart_0.dat`: contains particles forces at every 10 time steps
- `comPart_0.dat`: contains the compression forces experienced by each particle at every 10 time steps
- `piston_0.dat`: contains piston positions at every 10 time steps
- `charUnits.dat`: contains the characteristic units of the system
- `avgDis.dat`: contains the average distance of the particles at every 1000 time steps

- `comPart_norm.dat`: contains the compression forces experienced by each particle at every 1000 time steps, normalized by the maximum compression
- `posPart_norm.dat`: contains the particles position at every 1000 time steps
- `scales.dat`: the scale of the radius of each particle, useful for bi-disperse simulations: 1 for "big" particles and the aspect ratio (0.6, for example) for "small" particles

The normalized files are, then, used to conduct the analysis of the results.